



**TIMING AND SPECTROSCOPY REQUIREMENTS FOR A
PLASTIC SCINTILLATING FIBER BUNDLE TIME-OF-FLIGHT
NEUTRON SPECTROMETER**

THESIS

Paul A. Clement, First Lieutenant, USAF
AFIT-ENP-13-D-01

**DEPARTMENT OF THE AIR FORCE
AIR UNIVERSITY**

AIR FORCE INSTITUTE OF TECHNOLOGY

Wright-Patterson Air Force Base, Ohio

**DISTRIBUTION STATEMENT A.
APPROVED FOR PUBLIC RELEASE; DISTRIBUTION UNLIMITED.**

The views expressed in this thesis are those of the author and do not reflect the official policy or position of the United States Air Force, Department of Defense, or the United States Government. This material is declared a work of the U.S. Government and is not subject to copyright protection in the United States.

AFIT-ENP-13-D-01

TIMING AND SPECTROSCOPY REQUIREMENTS FOR A
PLASTIC SCINTILLATING FIBER BUNDLE TIME-OF-FLIGHT
NEUTRON SPECTROMETER

THESIS

Presented to the Faculty
Department of Engineering Physics
Graduate School of Engineering and Management
Air Force Institute of Technology
Air University
Air Education and Training Command
in Partial Fulfillment of the Requirements for the
Degree of Master of Science in Nuclear Engineering

Paul A. Clement, B.S.N.E.

First Lieutenant, USAF

December 2013


DISTRIBUTION STATEMENT A.
APPROVED FOR PUBLIC RELEASE; DISTRIBUTION UNLIMITED.

AFIT-ENP-13-D-01

TIMING AND SPECTROSCOPY REQUIREMENTS FOR A
PLASTIC SCINTILLATING FIBER BUNDLE TIME-OF-FLIGHT
NEUTRON SPECTROMETER

Paul A. Clement, B.S.N.E.
First Lieutenant, USAF


Approved:


Maj Benjamin R. Kowash (Chairman)

12 DEC 13
Date


Dr. John W. McClory, PhD (Member)

12 DEC 13
Date


Dr. Justin A. Clinton, PhD (Member)

12 DEC 13
Date

Abstract

The design parameters of a Time-of-Flight (TOF) neutron spectrometer composed of BCF-12 plastic scintillating fibers were investigated. A GEANT4 transport model was developed for analyzing the interaction of 2.5 MeV neutrons with a 14×14 BCF-12 fiber bundle. The bundle simulation demonstrated that 0.359% of all neutrons incident on the bundle will double scatter. The timing and data collection efficiencies of a Tektronix DPO7104 series digital oscilloscope were examined to determine the signal processing requirements for future fiber bundle measurements. The minimum detectable neutron energy was computed by taking into account the bundle scintillation efficiency, light collection efficiency, photodiode quantum efficiency, and quenching. For a BCF-12 fiber coupled to dual-readout Hamamatsu S10362-11-025C series Silicon Photomultipliers (SiPMT), the minimum detectable neutron energy was calculated to be 300–700 keV, depending on the fiber cladding and geometry. The spatial and timing uncertainties were set to 1 mm and 0.1 ns, respectively, to determine the overall energy uncertainty associated with a TOF neutron spectrometer. The uncertainties of 1 mm and 0.1 ns were chosen as the optimal capabilities of the the SiPMT and digital oscilloscope. Finally, analysis of a SiPMT in a light-tight box was performed to validate dark counts, determine light leakage and other detection system background noise. An experiment involving a 14×14 BCF-12 fiber bundle connected to dual-readout SiPMTs is recommended for future research to compare to the GEANT4 double scatter event probability.

*To my beautiful wife and child, my father, my late mother, and the rest of the
Clement Clan!*

*Without their continuous prayer, love and support I would have been unable to
complete my research.*

Acknowledgements

I would (again), first like to present a most sincere, loving and grateful thanks to my scintillating and amatory wife for being exceptionally supportive and understanding through the long distance engagement and countless hours dedicated to research; I love you! Also, to our first child who will enter this world in a few months and initiate our long journey in life toward having a large family. Special thanks (yet again) to my family as well as my wife's family, for all their prayers.

The education and experience gained at the Air Force Institute of Technology has been a great privilege granted to me by this great country and its citizens. I recognize that I have been given a unique and wonderful opportunity to attend such a prestigious graduate school. Hopefully with this education I can further our nation's defensive capabilities against those forces who threaten and challenge our safety.

I would like to acknowledge all the professors, faculty, staff, and mentors who have provided me their experiences, knowledge, time, tools, and opportunities in an effort to challenge me to reach my full potential. A few of these individuals include my thesis committee Maj. Ben Kowash, Dr. Justin Clinton, and Dr. John McClory, as well as the rest of the nuclear program faculty. The exhaustive amount of times asking questions during advisor meetings was always able to get me headed in the right direction when the research became unclear.

Finally, I would like to thank all of my fellow nuclear engineering classmates here at AFIT. The last 18 months have been better than anticipated due to the fun, helpful, and generous support demonstrated by all within the group. All of us will be headed in different career paths, but the memories will live on; thank you!

Paul A. Clement

Table of Contents

	Page
Abstract	iv
Acknowledgements	vi
List of Figures	ix
List of Tables	xx
List of Abbreviations	xxiii
I. Introduction	1
1.1 Motivation	1
1.2 Background	2
1.3 Objectives	3
1.4 Literature Review	4
1.5 Thesis Outline	7
II. Theory	8
2.1 Organic Scintillators	8
2.1.1 Light Output of Organic Scintillators	9
2.1.2 Time Response of Organic Scintillators	11
2.1.3 Photon Transport in Scintillators	13
2.2 Neutron Kinematics	18
2.3 Scintillating Fibers	22
2.3.1 Light Capture and Propagation	22
2.3.2 Estimating Scintillation Yield	27
2.3.3 Estimating Position and Energy Resolution	28
2.4 BCF-12 Plastic Scintillating Fibers	29
2.5 Photon Detection Techniques	33
2.5.1 Photomultiplier Tubes	34
2.5.2 Silicon Photomultipliers	36
2.6 Digital Data Acquisition	38
2.7 Spatial and Timing Resolution	41
III. Experiment & Simulation Methodology	43
3.1 Modeling a Single BCF-12 Fiber	43
3.1.1 Simulation of an Internal Optical Photon Source	44
3.1.2 Simulation of an External Neutron Source	45
3.2 Modeling of the BCF-12 Fiber Bundle Array	47
3.3 Construction of a 14×14 BCF-12 Fiber Bundle Array	48

	Page
3.4 Investigation of the DPO7104 Digital Data Acquisition	53
3.5 Scintillation Yield Parametric Study	60
3.6 Spatial and Timing Resolution Parametric Study	62
3.7 Single BCF-12 Fiber Readout Using SiPMTs	63
3.7.1 SiPMT Circuit Construction	64
3.7.2 SiPMT Dark Count Verification	70
IV. Results & Analysis	72
4.1 Geant4 Modeling	72
4.1.1 Single BCF-12 Fiber	72
4.1.2 14×14 BCF-12 Fiber Array	76
4.2 Digital Oscilloscope Findings	85
4.3 Scintillation Yield Findings	91
4.4 Spatial and Timing Resolution	93
4.5 SiPMT Findings	96
V. Conclusion & Recommendations	100
Appendix A. 14×14 BCF-12 Plastic Scintillating Fiber Geant4 Post-Processing Script	103
Appendix B. Dual Ended Readout Oscilloscope Script	112
Appendix C. Hamamatsu H3378-50 PMT Specifications	116
Appendix D. Scintillation Yield Script	118
Appendix E. Spatial and Timing Resolution Uncertainty Script	119
Appendix F. Peak Counting (Dark Count) Script	124
Appendix G. Fast Digital Data Acquisition Parameters	126
Bibliography	129

List of Figures

Figure		Page
1	The energy distribution of a recoil proton, E_P , produced by monoenergetic neutrons. For scattering from hydrogen, E_P is equivalent to E_R . Reproduced with permission from Knoll.	10
2	The two conditions at the interface/boundary of two dissimilar materials, where the scintillator material (denoted by ‘0’) has a greater refractive index than the surrounding material (denoted by ‘1’). The first ray and incident angle is given at the critical angle, θ_C , and is used for visual reference for the two following situations. Ray ‘A’ has an angle, θ_A , which is less than the critical angle; resulting in a <i>Fresnel</i> refraction of the optical photon into the surrounding material. Ray ‘B’ has an angle, θ_B , which is greater than the critical angle; resulting in total internal reflection. The interface conditions and results are reproduced with permission from Knoll.	15
3	The two coordinate systems: (<i>Left</i>) Center-of-Mass and (<i>Right</i>) Laboratory used to describe and depict neutron kinematics. The coordinate systems are reproduced with permission from Knoll.	19

4	<p>A cross-sectional view of a BCF-12 plastic scintillating fiber core, optical cladding, and extra mural absorber illustrating the effects of photon loss, trapping, and escape. (<i>Left</i>) The “trapped-photon” cones (denoted in red) open from the point of scintillation birth toward the fiber ends and show the angular domain, with respect to the fiber axis, where scintillation photons will internally reflect within the fiber. All the scintillation photons depicted in this fiber core on the left (denoted in green) have trajectories equal to or less than the critical cone angle ($\phi_C = 21.4$ deg), with respect to the fiber axis; thus they will internally reflect within the fiber. These internally reflecting scintillation photons in the fiber core on the left will continue to reflect until re-absorption by the fiber core. (<i>Right</i>) The “leaked-photon” tapered ring (denoted in blue) requires the 2π rotation to form the tapered ring which photons can escape. All of the scintillation photons depicted in the fiber core on the right (denoted in orange) have trajectories greater than the critical cone angle, with respect to the fiber axis; thus they will leak out of the fiber. The critical angle, θ_C, is normal to the core and cladding interface and equals 68.6 deg. The “escaped-photon” cone angle, ϕ_E, shows how the escaped photons, according to Snell’s Law, will broaden the angle calculated by the numerical aperture. Note the angles are not drawn to scale for illustrative reasons.</p>	25
5	<p>A depiction of how meridional and skew rays propagate through a fiber scintillator. (<i>Top</i>) Shows the lengthwise cross sectional view of the fiber scintillator as radiation enters and induces a scintillation event in the fiber. A single ray (denoted in red) is traced from the radiation induced event to illustrate the propagation down the length. (<i>Bottom</i>) Shows the fiber end (i.e. axial) cross sectional view of the fiber scintillator for both the meridional and skew rays.</p>	26
6	<p>An illustration of the the dual ended fiber readout variables. The position-of-interaction (POI) occurs at a distance x from end ‘1’ (i.e. left end). The scintillation yields at each end are N_1 and N_2. The figure is recreated and adapted from Capt Jones thesis.</p>	29

Figure		Page
7	A diagram of a typical Saint-Gobain Crystals, Inc. plastic scintillating fiber. Some properties of interest are the refractive indices of the core and cladding, as well as the critical cone angle ($\phi_C = 21.4$ deg). Scintillation photons generated between zero degrees and the critical angle will experience total internal reflection through both axial directions of the fiber. Scintillation photons that reach the ends of the fiber with an angle between zero degrees and the critical cone angle ($\phi_C = 21.4$ deg) will exit (i.e. escape) the fiber at the ends. The broadening of the angle to 35.7 deg is a result of Snell's Law and is calculated using the equation for the numerical aperture (Equation 17). This photo is reproduced with permission from Saint-Gobain's brochure for their scintillating fiber products.	31
8	The spectral response of a photodiode and PMT. The response of the photodiode is better suited for emission across the entire light spectra, whereas the PMT and bialkali PMT are only suited for the violet and blue. For reference the BCF-12 plastic scintillating fiber peaks at 435 nm, as shown in Figure 12. The plot is reproduced with permission from Knoll.	33
9	Top Three: Plots of voltage over time for a PMT anode pulse response at the two extremes of (<i>Middle</i>) Case 1: Large and (<i>Right</i>) Case 2: Small anode time constants. The plots are recreated and adapted from Knoll [6]. Bottom Three: Plots of the response exhibited by a photocathode. (<i>Left</i>) Response of photocathode, where individual electrons are leaving the photocathode. (<i>Middle</i>) Current at the anode after the multiplication of electrons. (<i>Right</i>) Leading edge of voltage pulse across anode circuit with large time constant. The plots are reproduced with permission from Knoll.	35
10	A general depiction of a readout circuit for a Geiger-mode APD. V_A is the bias voltage, R_B is the ballast resistor, $h\nu$ is the photon incident on the APD which generates a voltage V_D across the APD, R_L is the load resistor across which V_{OUT} is measured. The circuit is reproduced with permission from Cova et. al. <i>Evolution and prospects for single-photon avalanche diodes and quenching circuits.</i>	37

11	A diagram of the dual-ended SiPMT readout using digital data acquisition. The light output from the scintillator is converted into voltage pulses by the SiPMTs, which are then passed through and multiplied by the fast pre-amplifiers and then measured by the digital oscilloscope. The digital oscilloscope captures a set number of waveforms digitally in its internal buffer and then transfers the internal buffer to the computer via a gigabit Ethernet connection. The digital oscilloscope is controlled by the computer through TekVISA via a list of commands created in a MATLAB *.m file.	39
12	The emission spectra of the BCF-12 plastic scintillating fiber. Eight points were taken from the distribution to describe the function in Geant4. The wavelengths were converted to energy for the correct input type into the Geant4 model. The emission band of approximately 385–575 nm correspond to energies of 3.22–2.16 eV, respectively. The amplitude is normalized. The distribution was reproduced with permission from Saint-Gobain’s scintillating fibers brochure.	46
13	Illustration of the master key. The master key was made out of wood and was used for consistent 30 cm long fiber cuts. The notch along the top was made by drawing a line with a pencil and using a knife to cut down into the wood. The fiber was pulled off of the spool and set flush with the left side (depicted with diagonal lines). The fiber was gently pressed into the groove and cut at 30 cm lengths (designated by the dotted line).	49
14	Illustration of the construction of the 5×5 fiber array. The entire bundle is ~ 30 cm long with four pieces of double sided tape, placed ~ 10 cm apart, holding each layer (i.e. row) of fibers. The bottom right is a larger view of the fiber array end. The tape is $\sim 2.5 \times 2.5$ cm in dimension (denoted in gray). The arrows on the left of enhanced image denote the locations of the tape. Note: the fiber bundle is not completely assembled in this image nor drawn to scale for illustrative purposes.	51

Figure		Page
15	The “xy-plane” cross-sectional view of the 14×14 BCF-12 fiber bundle array. Each fiber is 500 micron (0.5 mm) in diameter, thus having an approximate height and width of 3.5 mm. Notice, upon shining a light through the fiber you can see light coming through; of course a few fibers appear to have some issues. These issues include angled (non-perpendicular) cleaved ends, crushed (oval-shaped) ends, and dark blemishes from over heated (burnt) plastic ends. Since all the ends were cleaved before construction an additional cleave needs to be made to create a flush surface.	52
16	The “z-axis” view of the 14×14 BCF-12 fiber bundle array. The bundle measures 30 cm in length, however, the ends are to be cleaved flush, thus will be shorter after the final cleaves are performed.	52
17	The “z-axis” view of the 14×14 BCF-12 fiber bundle array. The bundle is wrapped in black vinyl electrical tape to help mitigate light leakage out of the bundle. The tape was applied at a approximately a 45 deg angle and three layers were applied.	53
18	Illustration of a waveform measured and displayed by the Tektronix DPO7104 digital oscilloscope. The waveform depicts a typical response received by the digital oscilloscope from a SiPMT.	56
19	A diagram breaking down a single acquisition run (denoted in black). A single run is composed of set(s) (denoted in red), which is composed of waveform(s) (denoted in green). The run begins and ends with the start and stop of the MATLAB script for the SiPMT data collection.	57

20	An illustration of a run (denoted in black) from a programming and coding perspective. A run begins when the MATLAB (denoted in red) script is user started. The script progresses through configure, acquire, ask, read, save, write, and continue. The oscilloscope (denoted in green) receives command prompts from MATLAB through TekVISA commands which include configure, acquire, ask, and read. The computer (denoted in blue) receives data from MATLAB to save the run, which is composed of many set(s) containing multiple waveform(s). Solid lines represent a command being executed. Dotted lines represent a move to the next command after the current prompt is completed, where no new command is given and no data is transferred. The half solid, half dotted line represents data being transferred, where no new command is given.	59
21	The light-tight aluminum box used for SiPMT experimentation. The box measures 19×11×6 cm and is labeled A and B for the dual ended SiPMT experimentation. Black vinyl electrical tape was used to cover the edges of the lid-box interface to reduce the amount of light leakage into the aluminum box.	65
22	The Hamamatsu S10362-11-025C SiPMT. Note the effective active area is 1×1 mm and is depicted by the darker small square within the larger silver square. The SiPMT picture was obtained from the silicon photomultiplier technical brochure and reproduced with permission from Hamamatsu.	66

23	Basic connection diagram suggested by Hamamatsu for their SiPMTs. RG-223/U and RG-58C/U were used to wire the diagram to correctly match the impedance of the circuit. The RG-223/U coaxial cable was used for both the output signal and power and were connected to the box via a BNC connection. The connections inside the box were provided by a female-female BNC union. Four of these unions (two for power and two for signal output) were placed at the ends of the aluminum box. The Hamamatsu suggested SiPMT circuit diagram was obtained from their silicon photomultiplier technical brochure and reproduced with permission from Hamamatsu.	67
24	Basic connection diagram used for SiPMT-based TOF-PET detector. The circuit is reproduced with permission from Ronzhin et. al.	67
25	The light-tight aluminum box internal view. Each SiPMT is held securely in each aluminum jig with nylon washers and screws. The threaded rod extends length-wise across the entire inside of the aluminum box with both jigs secured with washers. Each SiPMT circuit connects to two female-female BNC ports via RG-223/U 50 ohm; one for bias voltage supply (-70.15 ± 0.03 V), and one for signal output to the preamplifier. The signal was to the tektronix DPO7104 digital oscilloscope with a T-connector and terminated with a 50 ohm terminator.	68
26	The front-side view of the SiPMT circuit attached to the aluminum jig inside the aluminum light-tight box. The small black box hole in the aluminum jig located between the threaded rod and nylon screw is the hole where the single BCF-12 scintillating fiber would be placed to contact the SiPMT. The hole is slightly larger than $500 \mu\text{m}$ (0.5 mm).	69
27	The back-side view of the SiPMT circuit attached to the aluminum jig inside the aluminum light-tight box.	69

Figure		Page
28	A view of the single BCF-12 fiber created in Geant4. The optical photon source is located at the intersection of the x and y-axis. The green vectors are traces of the optical photon trajectories within the fiber. While difficult to see, the light blue lines depict the outer cladding boundary, and the dark blue lines depict the outer core boundary. Note only the traces of the completely trapped optical photons are shown, and that for illustrative purposes this depicts an optical photon source of 100 generated photons.	73
29	A depiction of the solid angle, Ω , of the point source scintillating photons subtended by the plastic scintillating fiber. The gray shaded region indicates where the plastic scintillating fiber surface and source surface area overlap, which is constrained by the critical cone angle, ϕ_C , radius of the isotropic point source ‘sphere,’ r_S , and the radius of the plastic scintillating fiber, r_F . Note the lengths, radii, and angles are not drawn to scale for illustrative purposes.	76
30	Distribution of counts for distance traveled between 1st to 2nd, 2nd to 3rd, and 3rd to 4th neutron scatter events in the 14×14 BCF-12 fiber bundle. The 1st to 2nd neutron scatter is denoted in blue. The 2nd to 3rd neutron scatter is denoted in green. The 3rd to 4th scatter is denoted in red. The fiber bundle was subjected to 1×10^8 neutrons.	79
31	All 1st to 2nd, 2nd to 3rd, and 3rd to 4th neutron scatter event energies and respective distance traveled. The 1st to 2nd neutron scatters are denoted in blue. The 2nd to 3rd neutron scatters are denoted in green. The 3rd to 4th neutron scatters are denoted in red.	80
32	The overall scattering energy and distance traveled distribution for all scattering events combined. Each energy bin represents a dE of 100 keV and each distance bin represents a dx of 1 mm.	82

33	Comparison of the Geant4 and MATLAB calculated neutron energies for 1st to 2nd, 2nd to 3rd, and 3rd to 4th neutron scatter events. The majority of 1st to 2nd neutron scatter points follow the $\text{Geant4} = \text{Energy} (1/2mv^2)$ line, denoted in black. Note: the data marker size for 2nd to 3rd and 3rd to 4th neutron scatter events is larger than the 1st to 2nd neutron scatter events to increase visibility on the plot.	83
34	Comparison of two different frequency signals. Signal A has a lower frequency than signal B. If the same amount of time, t , is used to collect signals A and B, then it is expected that a greater number of pulses (or counts) will register for signal B than for signal A. Same logic follows that for a desired number of pulses (counts), signal B will take less time (t) to reach the desired number than signal A.....	88
35	Comparison of the various time components of a single fast digital data acquisition. The four plots show how each of the functions in a single acquisition affect the total time to perform the data collection. (<i>Top Left</i>) The “acquire time” directly relates to a change in frequency and/or waveform per set. (<i>Top Right</i>) The “ask time” demonstrates a negligible adjustment to a change in frequency and/or waveform per set. (<i>Bottom Left</i>) The “read time” reacts the same as the acquire time, where there is a direct relationship between the read time and a variation in frequency and/or waveform per set. (<i>Bottom Right</i>) The “save time” demonstrates no relation with frequency, but directly relates to a change in waveform per set. Both the acquire time and read time dominate the entire collection time by two orders of magnitude for frequencies less than 10 kHz, when compared to the ask time and save time. The acquire and read times are only one order of magnitude larger in time for frequencies greater than 10 kHz. Note: the legend in the acquisition time vs frequency plot applies to all four plots.	89
36	The fraction of the total pulses collected by the digital oscilloscope as the frequency (f), number of waveforms per set ($N_{W/S}$), and number of pulses per waveform changes ($N_{P/W}$).	91

37	Comparison of approximate number of scintillation photons detected by a SiPMT as a function of trapping efficiency. This assumes using a Hamamatsu S10362-11-025C Series SiPMT and a BCF-12 plastic scintillating fiber 30 cm in length with the position-of-interaction occurring at the middle of the fiber. The trapping efficiency of the the Saint-Gobain fibers changes with the fiber geometry and layers of cladding. In order of top to bottom in the legend the trapping efficiencies increase as 3.44%, 4.50%, 5.60%, and 7.30%.....	93
38	The energy and its uncertainty for calculated energies of 0-3 MeV and below based on a position uncertainty of 1 mm and timing uncertainty of 0.1 ns. Note for illustrative purposes the white region in the top left corners of both plots can be ignored since to get the appropriate scale the values were fixed.	95
39	Percent uncertainty shown as the relative percent uncertainty of σ_E with respect to energy, E . The contours show a sharp increase below ~ 1.75 ns and below 2 cm. This is where the ten percent uncertainty threshold is obtained for a position uncertainty of 1 mm and a timing uncertainty of 0.1 ns. The green circle denotes an energy of 1.45 ± 0.141 MeV at a position of 5 cm and time of 3 ns. The blue contour line denotes a relative error of 10%.	96
40	A snapshot of the oscilloscope showing a sample of the pulses produced by Hamamatsu S10362-11-025C SiPMT. The Tektronix DPO7104 digital oscilloscope was used with fast acquisition setting turned on. The the y-axis is at 40 mV/div and the x-axis is at 5 ns/div. The trigger level was set to 30 mV.	98

Figure		Page
41	(<i>Top</i>) The pulse height distribution of the dark counts from SiPMT A (Channel 1). The peaks are centered at approximately 0.125, 0.25, 0.375, and 0.5 V. (<i>Bottom</i>) The pulse height distribution of the dark counts from SiPMT B (Channel 2). The peaks are centered at approximately 0.12, 0.23, 0.34, and 0.45 V. The voltage was set to -70 ± 0.03 V. There was no source or scintillating fiber present in the aluminum light-tight box. Each pulse peak represents an additional pixel firing from the SiPMT.	99
42	A typical Hamamatsu cylindrical PMT module which closely resembles the H3378-50 PMT. The figure is reproduced with permission from Hamamatsu.	116

List of Tables

Table		Page
1	Variables and their definition used in the kinematics of neutron elastic scattering for both laboratory and center-of-mass coordinate systems. The table is reproduced with permission from Knoll.	19
2	Maximum fractional energy transfer in neutron elastic scattering, which is reproduced with permission from Knoll.	20
3	Saint-Gobain’s BCF-12 plastic scintillating single-clad fiber properties.	30
4	Characteristics of the Hamamatsu S10362-11-025C SiPMT.	37
5	Vertical axis acquisition specifications for the Tektronix DPO7104 digital oscilloscope used during these experiments and investigations.	40
6	Horizontal axis acquisition specifications for the Tektronix DPO7104 digital oscilloscope used during these experiments and investigations.	40
7	Optical emission properties used in the Geant4 model to define the BCF-12 plastic scintillating fiber. The BCF-12 optical properties were defined in Geant4 by breaking the emission distribution (Figure 12) into 8 points. The six parameters (only two shown here) defining the optical properties require a value at each of the 8 points. The units column represents the unit multiplier required by Geant4 to define the units of all the values contained within the respective parameter (i.e. row).	47
8	Characteristics of two arbitrary waveforms generated for the digital oscilloscope dead time experiments. The two types of pulses were generated by the Agilent 33220A 20 MHz Function/Arbitrary Waveform Generator. Both waveforms could range in frequency from 1 Hz to 5 MHz (period of 1 sec to 200 ns).	54

Table		Page
9	The scintillation yield parametric study yield parameters and their values. The scintillation efficiency, ϵ_{scint} , will only change as you change the type of scintillating fiber (e.g. BCF-10, 12, 20, 60, 91A, 92, 98). The trapping efficiency, ϵ_{trap} , changes as a function of fiber geometry (e.g. round versus square fibers). The non-quenching factor, $P_{non-quench}$, is assumed as 90%. The position-of-interaction, x , is fixed at 15 cm (but can be changed to user's desire) to represent the mid-point between the fiber ends (total length of fiber is 30 cm). The quantum efficiency, ϵ_{quant} , is a fixed characteristic of the SiPMT chosen. The model no. indicates whether the property describes the BCF-12 plastic scintillating fiber or the specific Hamamatsu S10362-11 series SiPMT. This table references parameters from Equation 18.	61
10	Distribution of scattering events for the 14×14 BCF-12 fiber array Geant4 simulation exposed to 1×10^8 neutrons.	77
11	Collection times for a 5000 kHz pulse, where each set is comprised of 1000 waveforms ($N_{W/S}$).	86
12	Collection times for a 1 kHz pulse, where each set is comprised of 1000 waveforms ($N_{W/S}$).	87
13	Hamamatsu photomultiplier tube H3378-50 assembly characteristics. The photocathode material for this PMT is bialkali (Sb-Rb-Cs or Sb-K-Cs) and the window material is quartz (synthetic silica). This information was reproduced with permission from Hamamatsu.	116
14	Hamamatsu photomultiplier tube H3378-50 cathode characteristics. This information was reproduced with permission from Hamamatsu.	116
15	Hamamatsu photomultiplier tube H3378-50 anode characteristics. This information was reproduced with permission from Hamamatsu.	117
16	Fast digital data acquisition parameters. (<i>Top</i>) 1 waveform per set. (<i>Bottom</i>) 10 waveforms per set.	127

Table		Page
17	Fast digital data acquisition parameters. (<i>Top</i>) 100 waveforms per set. (<i>Bottom</i>) 1000 waveforms per set.	128

List of Abbreviations

Abbreviation	Page
SNM	special nuclear material 1
DTRA	Defense Threat Reduction Agency 2
PMT	photomultiplier tube 2
TOF	time-of-flight 3
Geant4	Geometry and Tracking 3
BCF	bulk continuous fiber 3
PSF	plastic scintillating fiber 3
SiPMT	silicon photomultiplier 4
CFD	constant fraction discriminator 5
TAC	time to amplitude converter 5
PHA	pulse height analyzer 5
AFIT	Air Force Institute of Technology 6
MCNP5	Monte Carlo N-Particle Transport Code 6
POI	position-of-interaction 6
YAG:Ce	Yttrium Aluminum Garnet doped with Cerium 6
MeVee	mega-electron volt electron equivalent 9
FWHM	full width at half maximum 12
PMMA	polymethylmethacrylate 29
EMA	extra mural absorber 30
APD	avalanche photodiode 36
G-APD	Geiger-mode avalanche photodiode 36
VISA	Virtual Instrument Software Architecture 39

Abbreviation	Page
TekVISA	Tektronix Virtual Instrument Software Architecture 41
TOF-PET	time-of-flight positron emission tomography 66

TIMING AND SPECTROSCOPY REQUIREMENTS FOR A
PLASTIC SCINTILLATING FIBER BUNDLE TIME-OF-FLIGHT
NEUTRON SPECTROMETER

I. Introduction

Preventing the proliferation of special nuclear material (SNM) is a global initiative requiring ingenuity in the field of radiation detection. Neutron detection plays an important role in this effort. There are many advantages to using neutron detection technologies over other radiation detection systems. Neutrons provide unique fission signatures and are capable of penetrating materials which otherwise easily absorb gamma rays. Border crossings and portal monitors use helium-3 based neutron detectors, but since the supply of helium-3 is diminishing there is demand for other neutron detection technologies. Some of the challenges of neutron detection include low neutron energy detection, which affect scintillation detectors; the neutrality of neutrons, which renders electric fields useless in directing neutrons towards a detector; and background noise, which is created by alpha and beta particles as well as high-energy photons.

1.1 Motivation

There is considerable interest in radiation detection by the United States. The ever present danger of terrorists obtaining SNM is of the highest concern. Technologies which could help to detect, find, and rapidly identify SNM with high confidence are in constant demand. Current technologies such as gas-filled proportional detectors can accomplish some of this, however, more efficient and elementary methods

are sought to improve the SNM prevention and detection process. Government agencies such as the Defense Threat Reduction Agency (DTRA) research and develop radiation detection technologies such as stand-off detectors, helium-3 replacement materials, and new organic scintillator detectors as a means to find radioactive materials in the United States or abroad. There are various types of neutron detectors which include gas proportional detectors, scintillation neutron detectors, semiconductor neutron detectors, neutron activation detectors, and fast neutron detectors, all of which afford advantages and disadvantages. Gas-filled proportional detectors are optimal for neutron count rate, but are limited as energy spectrometers. Liquid organic scintillators are used for fast neutron applications and have pulse discrimination capabilities, but they lack in low thermal neutron efficiency and are susceptible to radiation damage effects. Semiconductor neutron detectors are only used for high neutron flux monitoring due to the crystal size limitations and low overall detection efficiencies. Developing a neutron-sensitive scintillating fiber optic bundle detector would provide great potential in modular placement of portable neutron detectors at ports and international border crossings to monitor imported goods and materials [1].

1.2 Background

The development of scintillators as a means of radiation detection trace back to the spinthariscopes, which was first built in 1903 by Sir William Crookes. The spinthariscopes featured a ZnS screen, which produced scintillations visible to the naked eye when viewed by a microscope in a dark room. While, this was a cornerstone in scintillator technology, this method was extremely tedious. It would take another four decades (1944) before Curran Baker brought scintillator technology out of naked eye measurement to more modern methods with the development of the photomultiplier tube (PMT) [1]. Development of scintillators progressed for a multi-

tude of reasons which included linearity, speed, density, transparency, and favorable costs to manufacture [1]. Over time scintillators have transformed from the ZnS of the early years to organic scintillators composed of aromatic hydrocarbon compounds and inorganic crystals composed of alkali metal halides. Eventually, with the advances in scintillator technology these organic and inorganic scintillators reduced the typically large cylinder and block geometries down to small scale (i.e. fractions of a millimeter) diameter fibers. Fiber optics have the advantages of transferring light and information over long distances with extreme flexibility. This advance in small diameter fiber scintillator technology led to this research on large scintillating fiber bundles. The possible advantages of a large fiber bundle as opposed to a single large block scintillator (of approximately the same size) includes better flexibility, efficiency, timing, and position resolution in developing novel Compton camera detectors capable of detecting special nuclear material.

1.3 Objectives

This research is focused on investigating the timing and spectroscopy requirements of a time-of-flight (TOF) neutron spectrometer. There are five research objectives, which are comprised of experiments, simulations, and parametric studies. The first objective is to understand the light production and collection processes in a single fiber optic cable. This process can be analyzed using the Geometry and Tracking (Geant4) particle interaction model by modeling a single bulk continuous fiber (BCF), specifically Saint-Gobain's BCF-12 plastic scintillating fiber (PSF), and incorporating all pertinent optical, absorption, emission, and other material properties into the model. The model can then simulate the fiber subjected to optical photon and neutron sources to record neutron scattering, energy deposition, and ray tracing which can help determine how the BCF-12 could respond to an experiment setup similar

to the simulation. The second objective will expand the single fiber simulation to a 14×14 BCF-12 plastic scintillating fiber bundle array to understand the interaction of radiation in a bundle, how the radiation produces light, and how the light appears as a quantitative signal that can be used to estimate the properties of the neutron that induced the signal. The third objective is to understand the timing and resolution requirements necessary for a functional spectrometer to provide optimal results. The results are considered optimal if they have less than ten percent relative error. By setting bounds on spatial and timing resolution an approximate region or domain of operation for optimal use of the proposed TOF neutron spectrometer can be determined. The fourth objective is to understand the signal processing requirements required for a functional spectrometer. These requirements include the dead time of the digital oscilloscope used for fast digital data acquisition of the detection system. Since, a digital oscilloscope will be utilized in reading, saving and writing the pulses produced from the silicon photomultiplier (SiPMT), the oscilloscope needs to be fast enough to resolve coincident pulse events on the picoseconds to nanosecond time scale. The final objective is to experimentally determine the minimum spatial resolution that can be achieved with a scintillating fiber optic cable. Related previous work by other investigators is briefly described in the next section.

1.4 Literature Review

Research into plastic scintillating fibers has been performed throughout the past twenty years [2] [3] [4] [5]. These experiments include efforts to understand “quenching” effects, increase neutron scattering cross-sections, and determine spatial resolution. Since this research focuses on the spatial and timing characteristics desired in a proposed novel TOF neutron spectrometer, the results of efforts to determine spatial resolution, experimental set-ups, and the results of similar experiments were sought.

Only a few of the more relevant efforts are described in this section.

Understanding the spatial resolution of BCF-12 fibers, or any plastic scintillating fiber, is crucial in implementing the fiber in a TOF neutron spectrometer. Takada et. al., performed a series of experiments to determine two linear relations [5]. The first was the relationship between the incident position of the neutrons and the change in time with which each photomultiplier tube responded to the incident light created by the neutron scatter. When the neutron beam was focused on different positions along the scintillating fiber a change in the PMT response time was observed. The second was the relationship between the neutron flux level and the counting rate. In their research they used BCF-20, which is similar to the BCF-12, differing only in wavelength emission and attenuation length. Saint-Gobain produces plastic scintillating fibers, designated as BCF, that emit in the blue or green with peak emissions between 430-530 nm and attenuation lengths ranging from 2.2–3.5 meters. Takada et. al. used a 1–2 MeV peak energy reactor neutron source and collimated the fast neutron beam down to a 5 cm diameter that was directed onto a single 1 mm diameter BCF-20 fiber. The fiber was connected directly to two photomultiplier tubes (PMT), with preamplifiers, a constant fraction discriminator (CFD), and a single time to amplitude converter (TAC), which fed into a pulse height analyzer (PHA). The results of this experiment determined the best achievable spatial resolution for a 1 mm diameter, 100 meter long, green emission fiber was approximately 16 cm. In this research, the hope is to obtain better spatial resolution on the order of one centimeter or less by making changes to the detection system setup featured in the research by Takada et. al. The first change is to use shorter length fibers, which will cause less attenuation of light. The second change is to utilize SiPMTs instead of PMTs for higher quantum efficiency.

Much of the research performed in this thesis stems from prior work carried out by

Gearhart in his Air Force Institute of Technology (AFIT) M.S. thesis titled, “Investigation of BCF-12 Plastic Scintillating Coherent Fiber Bundle Timing Properties” [2]. Gearhart worked with BCF-12 plastic scintillating fibers and developed a model of the BCF-12 fiber bundles exposed to a neutron source in the Monte Carlo N-Particle Transport Code (MCNP5). His model provides a comparison for my simulation of a 14×14 BCF-12 bundle created in Geant4. The MCNP5 model was simulated for various sized arrays of fibers from a single fiber up to a 100×100 BCF-12 bundle. The MATLAB script used to control the Tektronix DPO7104 digital oscilloscope for fast digital data acquisition written by Gearhart was used in this research with only a few minor adjustments. Other information provided by Gearhart’s research was background theory on scintillators, the techniques used in creating a BCF-12 fiber bundle, and the light-tight containers used for performing the initial light sensitive experiments.

Jones’ thesis titled, “Investigation of YAG:Ce Scintillating Fiber Properties Using Silicon Photomultipliers” provided valuable documentation and information to the development of this research [3]. The research used the attenuation lengths to conduct position-of-interaction (POI) measurements to determine the achievable position resolution of Yttrium Aluminum Garnet doped with Cerium (YAG:Ce) fibers using dual-readout SiPMTs. The results obtained were compared to theoretical calculations and Monte Carlo simulations. His research provided information on related theory, SiPMT design and calibration, the construction of two jigs for holding two SiPMT circuit boards for dual-readout of a single plastic scintillating fiber, and experimentation using dual-readout data collection. Jones’ research was focused on inorganic scintillating fibers as opposed to this research which focuses on the BCF-12 plastic fiber, which is an organic scintillating fiber.

1.5 Thesis Outline

This thesis presents the background, theory, methodology, experimentation, results, and analysis pertaining to the timing and spectroscopic parameters of a time-of-flight plastic scintillating fiber neutron spectrometer. It is divided into the following chapters: Chapter II - theory associated with the scope of organic scintillators, neutron kinematics, scintillating fibers, BCF-12 plastic scintillating fibers, photon detection, digital data acquisition, and spatial/timing resolution; Chapter III - methodology and experimentation performed during this investigation of BCF-12 plastic scintillating fiber time-of-flight neutron spectroscopy design parameters; Chapter IV - results and analysis of the simulations, experiments, and parametric studies; and Chapter V - conclusions and recommendations.

II. Theory

This chapter will present the theory pertaining to a dual-readout silicon photomultiplier scintillating fiber detection system. This system is comprised of a plastic scintillating fiber(s), silicon photomultipliers, charge sensitive preamplifiers, and a digital oscilloscope for fast data acquisition. As a suitable background information resource, interested readers may find it beneficial to review the scintillation mechanisms for organic or inorganic scintillators, which is described in detail in Knoll's *Radiation Detection and Measurement* [6]. The theory presented first addresses organic scintillator properties pertaining to light output, time response, and photon transport. Afterward, information on neutron kinematics is presented. Scintillating fibers are discussed with a focus on light capture and propagation, scintillation yield estimation, and position/energy resolution estimation, with an emphasis on BCF-12 plastic scintillating fiber properties and characteristics. Photon detection techniques using photomultiplier tubes and silicon photomultipliers are explained with the bulk of the attention given to silicon photomultipliers. Then, digital data acquisition as the preferred method for data collection is presented. Finally, the theory chapter will conclude with spatial and timing resolution as it pertains to how the uncertainty affects the energy calculation of a proposed TOF neutron spectrometer.

2.1 Organic Scintillators

The scientific field of scintillators is comprised of two main categories of scintillators, organic and inorganic. Organic-based scintillators are comprised of liquids or plastics with low density and low atomic number (i.e. Z number). The light output generated by organic scintillators is low and non-linear, while the hydrogen content is typically high, thus well suited for fast neutron detection. Other character-

istics of organic-based scintillators include fast decay times and the ability to perform pulse-shape discrimination between different types of particles. Inorganic-based scintillators are comprised of alkali halides, glasses and cerium-activated fast inorganic compounds. These types of scintillators differ from the organic-based scintillators in that they have high density and high atomic number. Compared to the organics they have higher and more linear light output, but slower decay times. This research focuses on organic-based plastic scintillating fibers and this section focuses on the light output and time response of organic scintillators, as well as photon transport.

2.1.1 Light Output of Organic Scintillators.

When incident radiation interacts with a scintillation material the majority of kinetic energy will be converted into heat. The small fraction of the total particle energy that isn't converted into heat and is instead converted into light is commonly known as the scintillation efficiency. The scintillation efficiency of the material is dependent on the type of particle and its energy. Electrons interacting with organic scintillators result in a linear response for energies up to 125 keV [6]. Heavy charged particles (e.g. alpha particles and protons) generate a smaller response when compared to electrons of the same energy. Another difference in heavy charged particle and electron interactions is the former demonstrates non-linearity up to larger energy thresholds. Although the responses of the two types of particles become similar as particle energy increases, the proton response will always be less than an equivalent energy electron response.

Organic scintillators commonly use the mega-electron volt electron equivalent (MeVee) term to describe the absolute light yield obtained by the scintillator to allow for direct comparison of scintillation yield across different impinging radiation particles. The energy required to generate 1 MeVee of light by definition is 1 MeV

for fast electrons and several MeV for heavy charged particles due to their reduced light yield per absorbed quantity of energy [6]. Since organic scintillators typically are hydrogen rich, incident heavy charged particles and neutrons interacting with the organic scintillator will generate a recoil proton. The energy distribution of a recoil proton from incident monoenergetic neutrons is well known and shown in Figure 1.

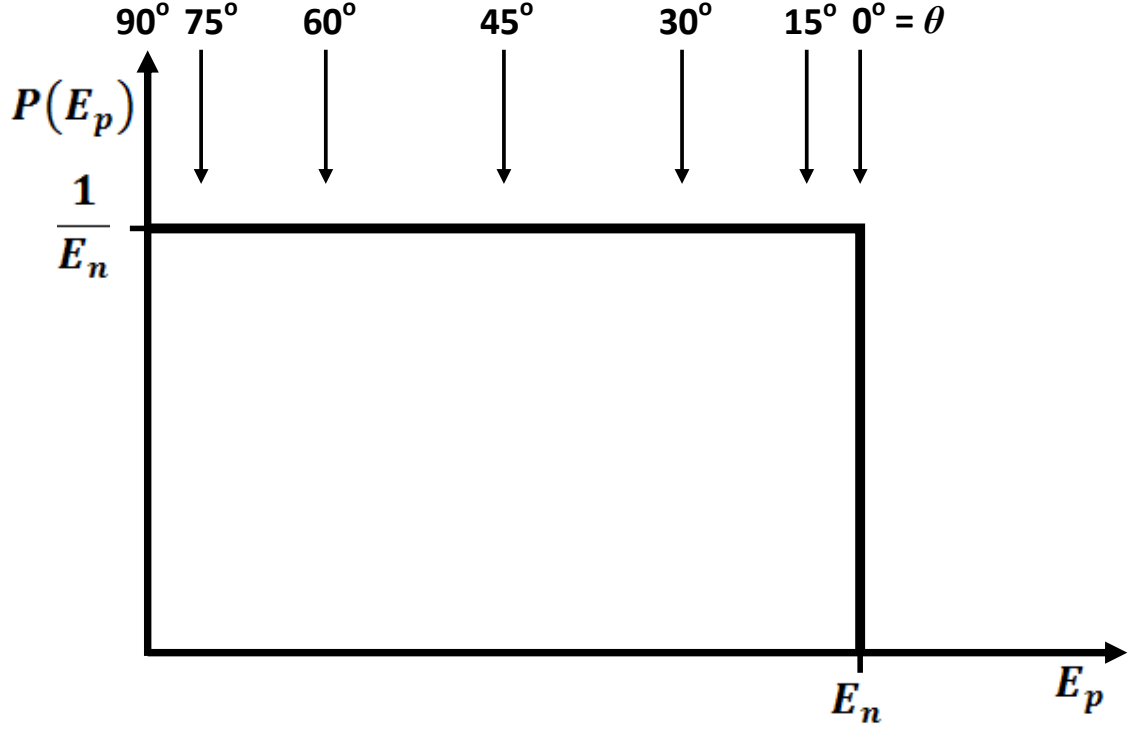


Figure 1. The energy distribution of a recoil proton, E_P , produced by monoenergetic neutrons. For scattering from hydrogen, E_P is equivalent to E_R . Reproduced with permission from Knoll [6].

The relationship between the fluorescent energy emitted per unit path length, dL/dx , and the specific energy loss for the incident charged particle, dE/dx , provides the initial foundation for describing the response of organic scintillators to charged particles. A relationship founded on the assumption that a high ionization density in the path of the particle produces quenching effects, due to the molecular structure incurring damage, and the resulting lowering of the scintillation efficiency is proposed by Birk [7]. This relationship postulates that the density of the molecular damage

from the particle along its trajectory within the scintillator and the ionization density are directly proportional. This direct relationship is represented by

$$\frac{dL}{dx} = \frac{S \frac{dE}{dx}}{1 + kB \frac{dE}{dx}}, \quad (1)$$

where, dL/dx is the emitted fluorescent energy per unit path length, S is the typical scintillation efficiency, dE/dx is the incident charged particle's specific energy loss, B is a proportionality constant, and k is the fraction of the ionization density which will cause quenching [7].

Additional mechanisms for sizable reductions in light yield in a scintillator include prolonged exposure to ionizing radiation, light, and oxygen. Degradation of the optical properties of organic scintillators is a result of the scintillator's exposure to ionizing radiation, while the over exposure of organic scintillators to light and oxygen typically induce slow polymer deterioration. Physical scratches and abrasions on the surface of organic scintillators, as well as other deformations to the surface from exposure to adverse and harsh environments, also cause degradation in the light yield due to the decrease in efficiency for internal light reflection.

The sum of all these factors of quenching, over exposure, and physical deformity are used to explain the reduction of light yield from organic scintillators. Each of these factors causes the initial scintillation yield within the scintillator to decrease as optical photons traverse the scintillator. Some of these factors are easy to quantify, while others will be unmeasurable and result in error.

2.1.2 Time Response of Organic Scintillators.

Organic scintillators will fluoresce and phosphoresce when de-exciting. Determining the response time profile requires making two assumptions. The first assumption is that the organic molecule instantaneously reaches the fluorescent states, and the

second assumption is that in this same organic molecule the only light response observed is prompt fluorescence. Applying these initial assumptions a time profile of the associated light pulse will be a very fast leading edge, for the rise time, followed by a simple exponential decay, for the fall time. This response pulse is described by

$$I = I_0 e^{-t/\tau} , \quad (2)$$

where, I represents the prompt fluorescent intensity of light at time t following excitation, I_0 is the initial fluorescent intensity, and τ represents the fluorescence decay time. However, more detailed representations of the time dependence of the scintillation yield take into account additional effects. These additional effects include the amount of time required to fill the luminescent states and the delayed fluorescence and phosphorescence. If the assumption is made that the filling of the optical levels is exponential the relationship in Equation 2 is modified to

$$I = I_0 (e^{-t/\tau} - e^{t/\tau_1}) , \quad (3)$$

where, in addition to the variables in Equation 2, τ_1 is the time constant for the filling of the optical levels. Other models assume the relationship is better represented by a Gaussian function, $f(t)$, and further characterized by a standard deviation, σ_{ET} , the overall shape of the light pulse is given by

$$\frac{I}{I_0} = f(t) e^{-t/\tau} . \quad (4)$$

Typically the rise and fall of the light output can be determined from experiments where the full width at half maximum (FWHM) of the resulting light versus time profile is carefully measured using very fast timing equipment and procedures. While equipment capable of nanosecond time scales to discriminate pulses is practi-

cal, time scales of picoseconds is more favorable. Common practice has dictated the performance (i.e. resolution) of ultrafast organic scintillators by their FWHM time, instead of the decay time. Faster decay times for scintillators is advantageous in most scintillator applications, except when the goal is to use pulse shape discrimination to distinguish between different radiation particles (e.g. alphas, neutrons, and gammas).

2.1.3 Photon Transport in Scintillators.

After the creation of the photons in the scintillator material, it is necessary to address the transport of these optical photons from creation through the scintillator. Absorption of the optical photons within a scintillator is primarily caused by impurities and point defects in the crystalline lattice. Other defects, which cause optical photon transport inefficiencies include air gaps, cracks, and rough surfaces. These optical impurities are a result of the crystal growth techniques implemented in the creation of the scintillator.

Scintillation photon transport is most easily described by reflections and refractions. The creation of the scintillation photons is considered isotropically distributed and randomly polarized. Snell's Law describes the reflection and refraction of light at the boundaries and interfaces of two different media. The relationship between the two materials at the boundary surface is given by

$$n_1 \sin(\theta_1) = n_0 \sin(\theta_0) , \quad (5)$$

where, subscripts '0' and '1' denote the two materials, n_i is the refractive index of the material, and θ_i is the angle measured from the normal of the media interface. The subscript '0' denotes the current material the photon is traversing through, while subscript '1' denotes the next material with which the photon could reflect or traverse through if refraction occurs. The index of refraction is defined as the ratio of the speed

of light in a vacuum to the speed of light in the material. Most organic scintillators have an index of refraction ranging from 1.4–1.6, which makes for a good interface coupling with photomultiplier tubes or silicon photomultipliers. The majority of photodetectors have some form of optical coating (e.g. glass, $n \approx 1.5$) for protection. With both materials having similar indices of refraction, the light is less likely to internally reflect.

The phenomena of internal reflection occurs when the photon travels from a material with a higher refractive index to a material with a lower refractive index. This presents an issue in the transfer of optical photons from the scintillating material to the photodetector, and is more prevalent in activated inorganic scintillators than organic scintillators. There is an angle at which point all optical photons are totally reflected back into the material, which is known as the critical angle (θ_C), defined by

$$\theta_C = \sin^{-1} \left(\frac{n_1}{n_0} \right), \quad (6)$$

where, the equation defines an optical photon traveling from material ‘0’ to material ‘1’. The initial material containing the optical photon requires a refractive index (n_0) that is greater than the second material refractive index (n_1) for total internal reflection to occur. An illustration of the two situations of optical photon transport at a dissimilar material interface is provided in Figure 2. The leakage and total internal reflection of optical photons occurs at two critical and differing boundaries. The first is at the interface between the scintillator core and the optical cladding where the majority of optical photons will leak out. The second, is the at the interface between the scintillator core fiber ends and the photosensor lens (i.e. window). In the latter of the two, it is desired to lose optical photons from the fiber core into the photosensor window. This is called optical photon “escape” in this research, where the escaping optical photons are measured by the detection system.

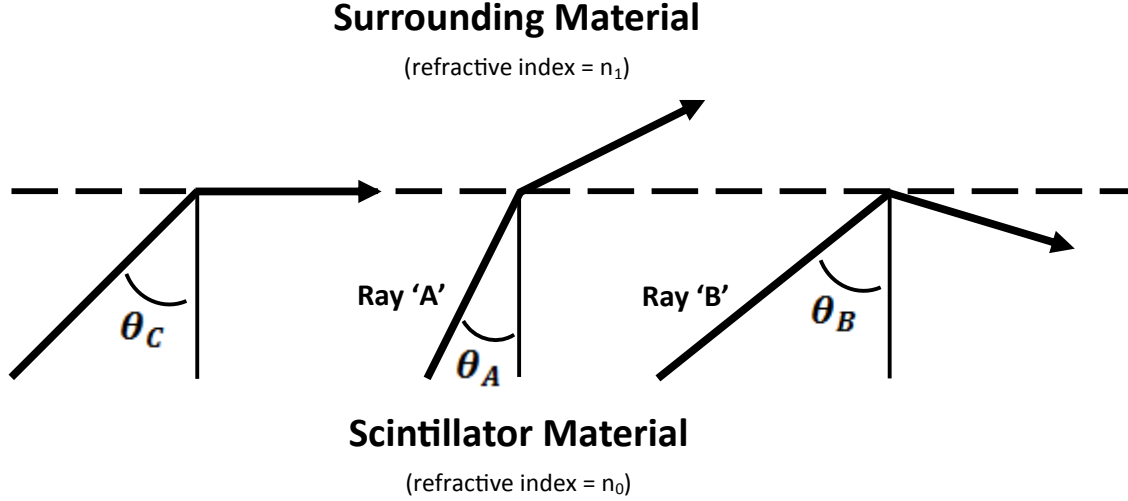


Figure 2. The two conditions at the interface/boundary of two dissimilar materials, where the scintillator material (denoted by ‘0’) has a greater refractive index than the surrounding material (denoted by ‘1’). The first ray and incident angle is given at the critical angle, θ_C , and is used for visual reference for the two following situations. Ray ‘A’ has an angle, θ_A , which is less than the critical angle; resulting in a *Fresnel* refraction of the optical photon into the surrounding material. Ray ‘B’ has an angle, θ_B , which is greater than the critical angle; resulting in total internal reflection. The interface conditions and results are reproduced with permission from Knoll [6].

The two conditions for the optical photon traversing from one material to the other are both desired for different reasons in the scintillation system. The condition where the optical photon is completely internally reflected is best suited for the scintillator core and cladding material boundary to “pipe” light down the axial length of the fiber to the ends for collection by a photosensor. The collection of the scintillation photons by the photosensor requires the condition where the scintillation photon trajectory is less than the critical angle (θ_C), with respect to the normal of the boundary interface, hence the photon is able to leave the scintillator material and enter the surrounding material. The ability of photons to escape the scintillator and enter the photosensor increases the detection efficiency of the scintillator and photosensor system. If scintillation photons reflect off the photosensor window and internally reflect, then scintillation photons can travel between the fiber ends bouncing from one end to other until they leak, escape, or undergo re-absorption. These reflections may

appear to be new scintillation creation events, when measured by the photosensor.

The discrimination of true scintillation events from these potential reflections involves two different methods. The first is pulse height discrimination and the second is time discrimination. For pulse height discrimination, the majority of scintillation photons that are totally internally reflected down the scintillator toward the ends will exit and escape the scintillator into the photosensor, thus providing a large pulse response on the readout. A delayed and smaller pulse response, “reflected pulse,” is produced from the photosensor’s collection of a few scintillation photons which are reflected from the scintillator-photosensor interface. This smaller and delayed pulse is composed of only a few photons, which is on the same order of pulses produced by the detection system, environment, and background noise. All acquired data requires pulse height discrimination in the post-processing of the data.

The time discrimination method involves calculating the expected time it takes for a scintillation event to reach each end of the fiber, which will differ depending on the location of the scintillation photon creation, and comparing this to the time it takes the reflected scintillation photon to travel. The time it takes the photons to travel from origination to a photosensor is used for comparison to the time it takes the “reflected photons” to travel from one end of the plastic scintillating fiber to the other end and enter the same photosensor. The time it takes for the scintillation photons to travel to the ends of the scintillator and escape or reflect can be calculated from a few relations involving the velocity of light, refractive index, and length of the scintillator material. The relationship is given by combining the equations which define velocity and the refractive index, Equations 7 and 8, respectively,

$$v = \frac{dx}{dt}, \quad (7)$$

where, v is the velocity of the scintillation photon, dx is the length of the scintilla-

tor, and dt is the time it takes the scintillation photon to travel the length of the scintillator; and

$$n = \frac{c}{v}, \quad (8)$$

where, n is the refractive index of the scintillator material and c is the speed of light in a vacuum. Combining these equations and replacing dx and dt with x and t , respectively for simplicity, provides the final relationship to determine the time it takes an optical photon to reflect from one end of the scintillator and travel to the opposite end,

$$\begin{aligned} v &= \frac{x}{t} = \frac{c}{n}, \\ t &= \frac{x n}{c}. \end{aligned} \quad (7)$$

Since the time scales required in time-of-flight neutron spectroscopy using plastic scintillating fibers is on the order of $10^2 - 10^3$ of picoseconds, the reflections may not be of concern if the length of the fiber is long enough. For short length fibers the reflections will require less time to travel the full length of the fiber, thus potentially broadening further the pulse response by the photosensor (i.e. increase in energy uncertainty). This will especially occur in scintillation induced events created at the fiber ends closest to the photosensors due to the smaller time separation between the original photons and “reflected photons” reaching the opposite end photosensor. However, if the fibers are long enough, then the reflections will require a longer period of time, thus mitigating the concern of receiving a broadened pulse response. For instance, using Equation 7 for a plastic scintillating fiber with a refractive index of $n = 1.60$ and a fiber length of $x = 30$ cm; the time (t) it takes for a scintillation photon to reflect off of a photosensor window and travel from one end to the other would be approximately 1.6 ns. For every additional 10 cm of plastic scintillating fiber length,

with the same properties, it takes an additional ~ 0.5 ns for the reflected scintillation photons to travel. These issues should be taken into consideration when determining scintillating fiber length for time-of-flight spectroscopy detection applications.

This method of time discrimination is also applied to neutron scatters. Time-of-flight neutron spectrometers must be capable of discriminating between successive neutron scatters. If the velocity of the neutron is known (derived from the neutron energy), then Equation 7 can be used to determine the time between scatters of varying distance. The same is then applied for determining the distance between successive neutron scatters based on varying the time. These calculations are the basis of analyses to determine potential spatial and timing resolution requirements for a TOF neutron spectrometer, which is discussed in greater detail in Section 2.7.

2.2 Neutron Kinematics

Fast neutron detection most commonly uses the method of scattering of neutrons by light nuclei (e.g. hydrogen, deuterium, or helium) [8]. A recoil nucleus is generated when a portion of an incident neutron's kinetic energy is transferred to the target nucleus. Hydrogen is the preferred target nuclei due to its superior energy transfer characteristics. Hydrogen is able to receive all of an incident neutron's kinetic energy. When the target nuclei are light, the recoil nucleus behaves much like a proton or alpha particle in the way that it loses energy in the detector medium [9].

Using conservation of momentum and conservation of energy equations to describe the kinematics of an incident neutron upon a target nucleus produces some simple equations and relationships. Equation 9 utilizes the variables contained within Table 1. Figure 3 provides a schematic to visually describe the relationship between an incident neutron, target nucleus, and recoil neutron.

For incoming non-relativistic neutrons (i.e. $E_n \ll 939$ MeV) the relation for the

Table 1. Variables and their definition used in the kinematics of neutron elastic scattering for both laboratory and center-of-mass coordinate systems. The table is reproduced with permission from Knoll [6].

Variable	Definition
A	Mass of the target nucleus/neutron mass
E_n	Incident neutron kinetic energy (laboratory coordinate system)
E_R	Recoil nucleus kinetic energy (laboratory coordinate system)
Θ	Scattering angle of neutron (center-of-mass coordinate system)
θ	Scattering angle of recoil nucleus (laboratory coordinate system)

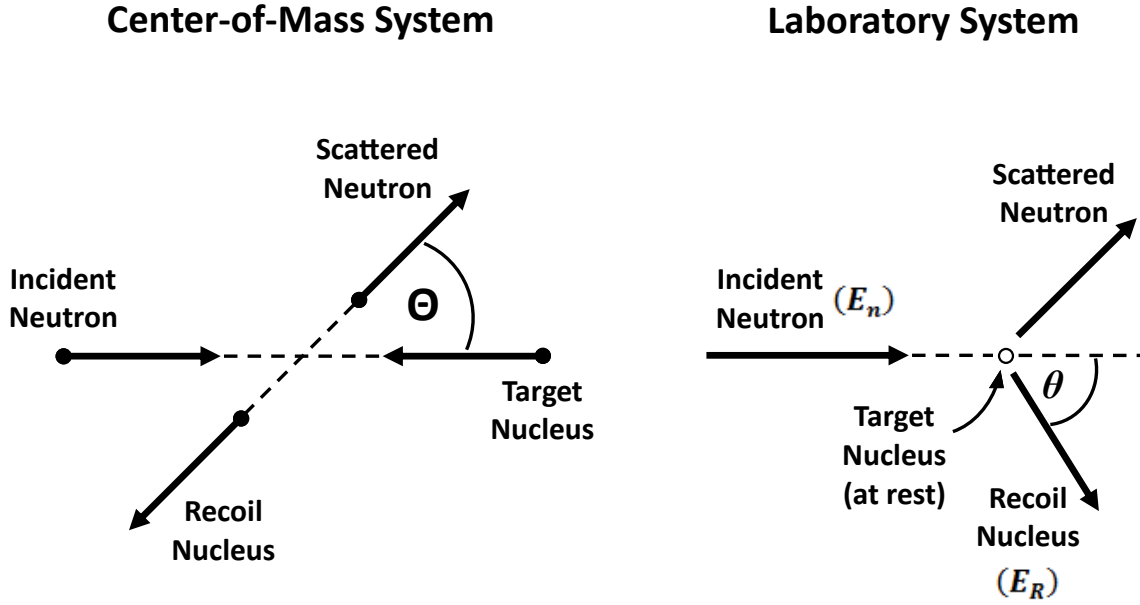


Figure 3. The two coordinate systems: (*Left*) Center-of-Mass and (*Right*) Laboratory used to describe and depict neutron kinematics. The coordinate systems are reproduced with permission from Knoll [6].

energy of the recoil nucleus in the center-of-mass coordinate system is given by

$$E_R = \frac{2A}{(1+A)^2} [1 - \cos(\Theta)] E_n. \quad (9)$$

To convert to the laboratory coordinate system in which the original target nucleus is at rest, to the center-of-mass coordinate system, we use

$$\cos(\theta) = \sqrt{\frac{1 - \cos(\Theta)}{2}}. \quad (10)$$

Combining Equations 9 and 10 gives the relation for the recoil nucleus energy in terms of its own angle of recoil

$$E_R = \frac{4A}{(1+A)^2} [\cos^2(\theta)] E_n. \quad (11)$$

From Equation 11 the energy of the recoil nucleus is uniquely determined by the scattering angle. For a scattering angle in which the target nucleus is slightly grazed by the incident neutron (i.e. $\theta \cong 90$ deg), the recoil energy approaches zero. On the other hand, a head-on collision between the incident neutron and the target nucleus (i.e. $\theta \cong 0$ deg) results in the maximum possible recoil energy

$$E_R \Big|_{max} = \frac{4A}{(1+A)^2} E_n. \quad (12)$$

Using Equation 12, the maximum fraction of incident neutron energy that can be transferred to a recoil nucleus can be calculated for various target nuclei as in Table 2. The general trend, as expected, of the maximum fractional energy transfer decreases as the target nucleus mass increases. This demonstrates why hydrogen is desired in the creation of a neutron detection system based on elastic scattering.

Table 2. Maximum fractional energy transfer in neutron elastic scattering, which is reproduced with permission from Knoll [6].

Target Nucleus	A	$\frac{E_R}{E_n} \Big _{msx} = \frac{4A}{(1+A)^2}$
${}^1_1\text{H}$	1	1
${}^2_1\text{H}$	2	$8/9 = 0.889$
${}^3_2\text{He}$	3	$3/4 = 0.750$
${}^4_2\text{He}$	4	$16/25 = 0.640$
${}^{12}_6\text{C}$	12	$48/169 = 0.284$
${}^{16}_8\text{O}$	16	$64/289 = 0.221$

The energy distribution of recoil nuclei are distributed between a minimum of zero and a maximum value (i.e. the entire energy of the incident neutron), which is shown in Table 2. If we assume that all scattering angles are possible, a continuum of recoil energies between these two extremes is expected. If $\sigma(\Theta)$ is defined as the differential cross section in the center-of-mass system, the probability that the neutrons will be scattered into $d\Theta$ about Θ is given by

$$P(\Theta) d\Theta = 2\pi \sin(\Theta) d\Theta \frac{\sigma(\Theta)}{\sigma_s}, \quad (13)$$

where, σ_s is the total scattering cross section integrated over all angles. While the distribution in recoil nucleus scattering angle can be helpful, the distribution in recoil nucleus energy is of greater importance. The distribution of recoil nucleus energy can be obtained if we let $P(E_R) dE_R$ represent the probability of creating a recoil with energy dE_R about E_R . This results in the following relationship

$$P(E_R) dE_R = P(\Theta) d\Theta. \quad (14)$$

By simply substituting Equation 13 into Equation 14 the resulting relationship provides the expected recoil energy based on the recoil nucleus scattering angle

$$P(E_R) = 2\pi \sin(\Theta) \frac{\sigma(\Theta)}{\sigma_s} \cdot \frac{d\Theta}{dE_R}. \quad (15)$$

Close observation of Equation 15 shows the recoil energy continuum does in fact have the same shape as the differential cross section, $\sigma(\Theta)$ as a function of the scattering angle. Most target nuclei will preferentially forward or backward scatter, which is confirmed by the distribution of $\sigma(\Theta)$. When the target nuclei is hydrogen, the scattering process becomes isotropic, for the center-of-mass system. The expected proton recoil energy distribution, as was shown earlier in Figure 1, is a rectangular

area extending from zero to the incident neutron total energy. Since the BCF-12 fiber is a hydrogen rich material, it is expected that bombarding this material with neutrons will yield a response function similar to Figure 1.

2.3 Scintillating Fibers

This section will discuss the characteristics and properties of scintillating fibers as there are some inherent differences in behavior from other scintillators, mostly attributed to geometric characteristics. The science of fiber optics deals with the transmission or guidance of light (rays of waveguide modes in the optical region of the spectrum) along transparent fibers of glass, plastic, or a similar medium [10]. Fiber scintillators are highly sought for high-energy particle tracking experimentation due to their inherently achievable two dimensional position when also coupled with pixelated detectors. Scintillating fibers range in size from 0.25–1 mm in diameter, shaped in geometries (typically circular or square cross-sections) conducive to ray propagation, and are made of plastic or glass because of their favorable optical properties.

2.3.1 Light Capture and Propagation.

Incident radiation that generates a scintillation event within a plastic scintillating fiber produce scintillation photons. These photons traverse the fiber with only a small fraction of them successfully reaching the ends of the fiber. The portion of the initial scintillation photons which reach the end is inversely proportional to the ratio of scintillator core and cladding refractive indices. Using the solid angle subtended within the fiber and bounded by the cone angle, which determines complete total internal reflection, provides the initial relationship to determine the fraction of scintillation photons trapped within a scintillating fiber,

$$\begin{aligned}
F_T &= 2 \cdot \frac{\Omega}{4\pi} = \frac{1}{2\pi} \int_0^{2\pi} d\phi \int_0^{\pi-\theta_c} \sin(\theta) d\theta \\
&= 1 - \cos(\pi - \theta_c) = 1 - \sin(\theta_c) \\
&= 1 - \frac{n_{clad}}{n_{core}},
\end{aligned} \tag{16}$$

where, F_T is the fraction of light trapped within the scintillating fiber, ϕ_C is the cone angle which is measured with respect to the fiber axis, Ω is the solid angle subtended by the cone angle (ϕ_C), and θ_C is the critical angle which is measured with respect to the normal of the scintillator fiber core and cladding interface. Figure 4 is provided later in this section as an aid in identifying the difference between the cone angle, ϕ_C , and the critical angle, θ_C .

A close inspection of the refractive indices ratio in Equation 16 shows the trapping efficiency can be increased by increasing the scintillator core refractive index and/or decreasing the scintillator cladding refractive index. Increased detection of incident radiation (e.g. alphas, gammas, and neutrons) by a scintillating fiber requires the highest total internal reflection to occur within the fiber until the scintillation photons reach the fiber ends. When the scintillation photons reach the end of the fiber they must escape the fiber, instead of internally reflecting, to enter the photosensor for measurement. The BCF-12 fiber, like most scintillating fibers, has a high cladding-to-core refractive index ratio. According to the scintillation products brochure, Saint-Gobain claims a cladding and core refractive index of 1.49 and 1.60, respectively, which equates to a ratio of 0.931 [11]. A large cladding-to-core refractive index ratio produces large critical angles (i.e. small critical cone angle), which reduces the amount of trapped light within the fiber from a radiation induced scintillation event. The large critical angle and consequently low trapping efficiency, which is on the order of 3–4%, provides the desired condition to allow scintillation photons to escape the ends of the fiber and produce a measured result from the photosensor.

A photosensor can only measure light that enters the detection window. For a photon to escape the scintillating fiber core and enter the photosensor requires the scintillation photon to have a trajectory that increases the probability of escape. If the scintillation photon reaches the fiber end with an angle less than or equal to the trapped photon cone angle (i.e. critical cone angle, ϕ_C) then the scintillation photon has a high probability of being measured after entering the photosensor. Saint-Gobain claims a total internal reflection angle of 68.6 deg, with respect to the fiber core-cladding boundary and a critical cone angle of 21.4 deg, with respect to the fiber axis. Any scintillation photons which have trajectories greater than the critical cone angle will remain trapped within the fiber until lost by means of optical absorption. An illustration of the scintillating fiber core trapped, leaked, and escaped photon properties is provided in Figure 4.

As the scintillation photons escape the fiber into the photosensor window, the photons will refract. The amount the photon will refract is determined by the numerical aperture, NA . The launch angle, θ_{launch} , core refractive index, and cladding refractive index provide a relationship to the numerical aperture, which is given by

$$NA = n \cdot \sin(\theta_{launch}) = \sqrt{n_{core}^2 - n_{clad}^2}. \quad (17)$$

where, NA is the numerical aperture, n is the refractive index of the external material (e.g. air or photosensor window), and the θ_{launch} is the launch angle (i.e. escaped-photon cone in Figure 4).

There are two means of light propagation within a scintillating fiber depending on the location of the radiation induced scintillation event, which are meridional and skew rays. The difference in the two modes of propagation is in the paths taken after reflecting off the core-cladding boundary within the fiber core, shown in Figure 5. The meridional rays traverse the fiber core by reflecting off of the core-cladding interface

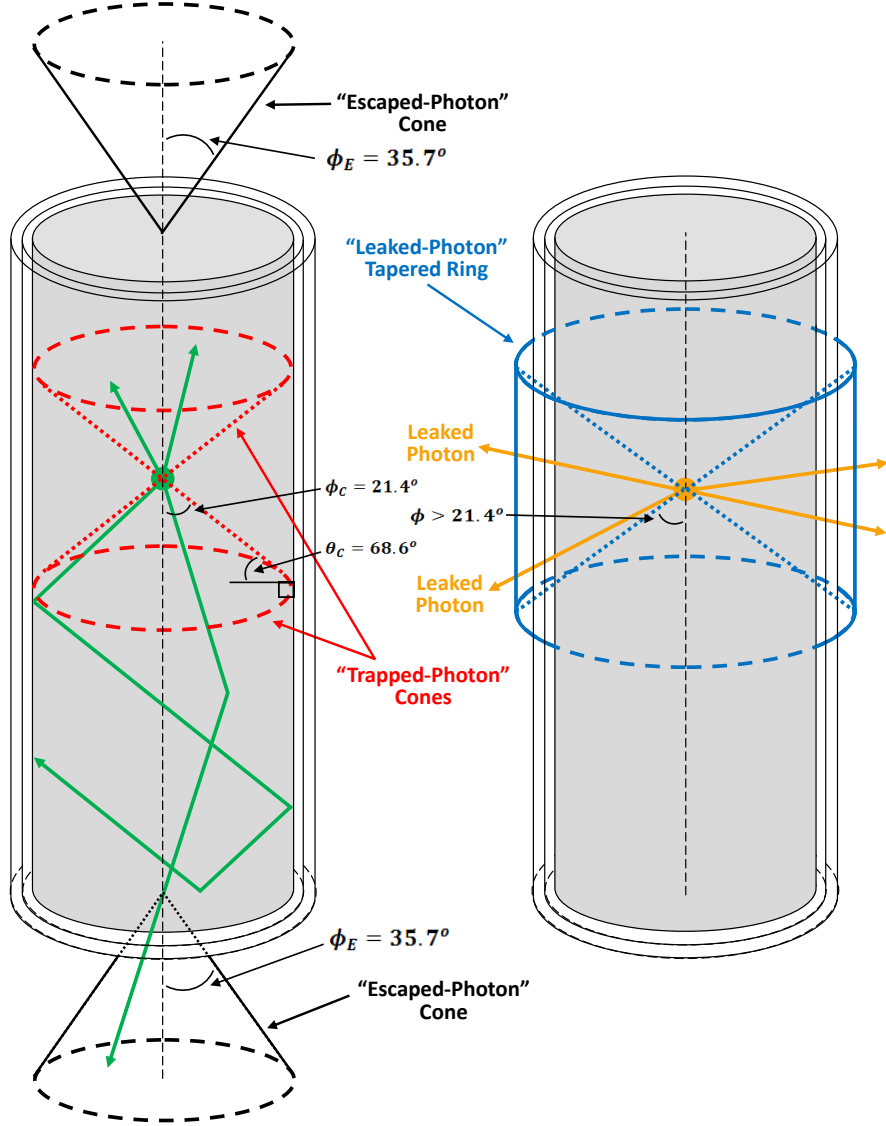


Figure 4. A cross-sectional view of a BCF-12 plastic scintillating fiber core, optical cladding, and extra mural absorber illustrating the effects of photon loss, trapping, and escape. (*Left*) The “trapped-photon” cones (denoted in red) open from the point of scintillation birth toward the fiber ends and show the angular domain, with respect to the fiber axis, where scintillation photons will internally reflect within the fiber. All the scintillation photons depicted in this fiber core on the left (denoted in green) have trajectories equal to or less than the critical cone angle ($\phi_C = 21.4$ deg), with respect to the fiber axis; thus they will internally reflect within the fiber. These internally reflecting scintillation photons in the fiber core on the left will continue to reflect until re-absorption by the fiber core. (*Right*) The “leaked-photon” tapered ring (denoted in blue) requires the 2π rotation to form the tapered ring which photons can escape. All of the scintillation photons depicted in the fiber core on the right (denoted in orange) have trajectories greater than the critical cone angle, with respect to the fiber axis; thus they will leak out of the fiber. The critical angle, θ_C , is normal to the core and cladding interface and equals 68.6 deg. The “escaped-photon” cone angle, ϕ_E , shows how the escaped photons, according to Snell’s Law, will broaden the angle calculated by the numerical aperture. Note the angles are not drawn to scale for illustrative reasons.

and passing through the fiber axis. The skew rays traverse the fiber core by reflecting off of the core-cladding interface and never passing through the fiber axis. Due to the different trajectories taken, the meridional rays will have shorter path lengths than the skew rays and thus reach the fiber ends in a shorter amount of time.

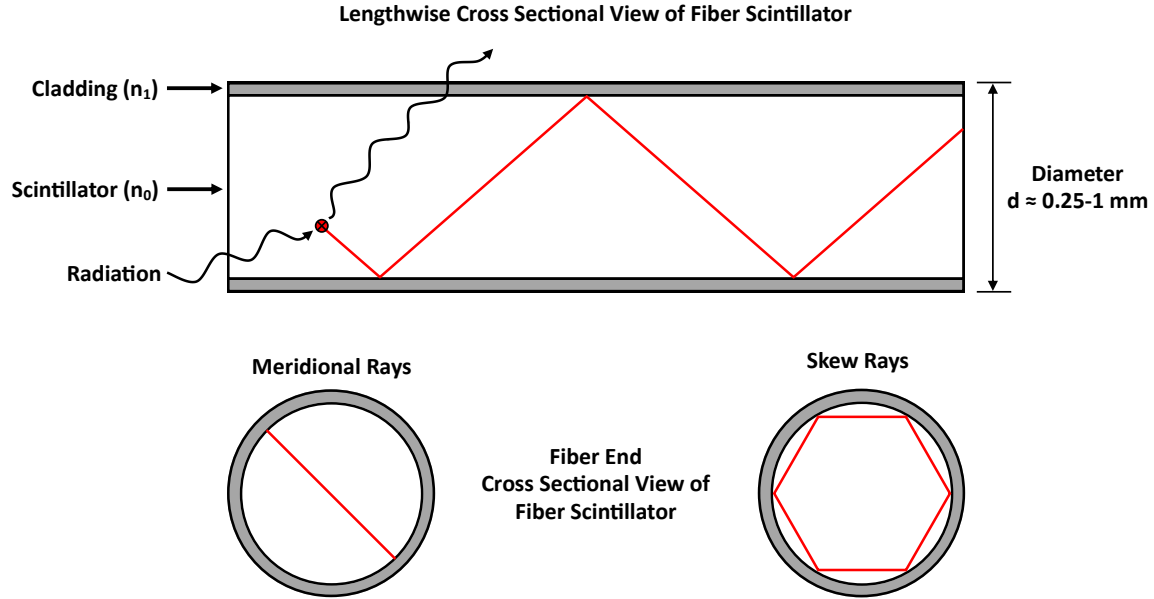


Figure 5. A depiction of how meridional and skew rays propagate through a fiber scintillator. (*Top*) Shows the lengthwise cross sectional view of the fiber scintillator as radiation enters and induces a scintillation event in the fiber. A single ray (denoted in red) is traced from the radiation induced event to illustrate the propagation down the length. (*Bottom*) Shows the fiber end (i.e. axial) cross sectional view of the fiber scintillator for both the meridional and skew rays.

Determining the position of the radiation induced scintillation event within the fiber relies heavily on the precision of the timing measurements. The timing information is contained in the time difference between the measured light reaching each photosensor from the same scintillation event. Uncertainty in this time difference measurement is in the response time of photosensors and oscilloscope's timing resolution. If the detection system produces resolvable time difference measurements then the position-of-interaction of the radiation induced event can be determined, which is known as the “time-of-flight” method. The TOF method has many applications including particle tracking, electron mobility, and mass spectroscopy experiments [5] [12] [13].

2.3.2 Estimating Scintillation Yield.

The scintillation yield in a plastic scintillator can be characterized with a few parameters, the scintillator efficiencies and energy deposited by a neutron,

$$N_{photons} = \frac{1}{2} E_n \epsilon_{scint} \epsilon_{trap} P_{non-quench} \cdot \exp\left(-\frac{x}{\lambda_{eff}}\right) \epsilon_{quant} , \quad (18)$$

where, $N_{photons}$ is the number of photons detected at one end of a single scintillating fiber, E_n is the amount of energy deposited in the scintillator by a neutron, ϵ_{scint} is the scintillation efficiency (i.e. photons per keV) of the scintillator material, ϵ_{trap} is the trapping efficiency of the scintillator material, $P_{non-quench}$ is the non-quenching factor, x is the distance from the position-of-interaction to the end of the fiber, λ_{eff} is the effective attenuation length of the scintillator material, and ϵ_{quant} is the quantum efficiency of the photosensor. Depending on the desired set up of Equation 18 the non-quenching factor ($P_{non-quench}$) could be substituted with the quenching factor (P_{quench}), which is given by the relationship

$$P_{quench} = 1 - P_{non-quench} . \quad (19)$$

Rearranging Equation 19 and substituting back into Equation 18 provides for a slightly different variation of the number of photons detected at one end of a single scintillating fiber ($N_{photons}$) based on the quenching factor

$$N_{photons} = \frac{1}{2} E_n \epsilon_{scint} \epsilon_{trap} (1 - P_{quench}) \cdot \exp\left(-\frac{x}{\lambda_{eff}}\right) \epsilon_{quant} . \quad (20)$$

2.3.3 Estimating Position and Energy Resolution.

Long scintillating fibers make position-of-interaction calculations using the time-of-flight method more feasible since photons require more time to travel longer distances. Long scintillating fibers, typically on the order of meters to tens of meters, can potentially be useless in the POI calculations if the attenuation length (i.e. $1/e$ length) is much shorter than the length of the fiber. The attenuation length of the scintillating fiber describes the light intensity at a specific distance from the induced scintillation event. A scintillation event has its greatest intensity of light (i.e. number of photons) at the event's position-of-interaction and the number of photons will decrease with distance. An exponential decay using the ratio of the distance from the interaction site to the attenuation length describes the number of surviving photons,

$$N = \frac{1}{2} N_0 \cdot \exp\left(-\frac{x}{\lambda}\right), \quad (21)$$

where, N_0 is the estimated total amount of scintillation photons produced, x is the distance between the position-of-interaction and the photosensor, and λ is the attenuation length of the scintillating fiber.

If the initial amount of scintillation photons and the attenuation length of the scintillating fiber are known or measured, then the radiation induced scintillation event location can be calculated. The position is solved for by using Equation 21 for each photosensor and combining the two expressions. Further manipulation, incorporation of the fiber length, and solving for the position, x , gives the following

$$x = \frac{1}{2} \left(\lambda \ln \left(\frac{N_2}{N_1} \right) + l \right), \quad (22)$$

where, x is the position-of-interaction, l is the fiber length, N_2/N_1 is the relative signal amplitude ratio measured by the photosensors at each end of the fiber. Figure 6, provides a schematic to define these variables.

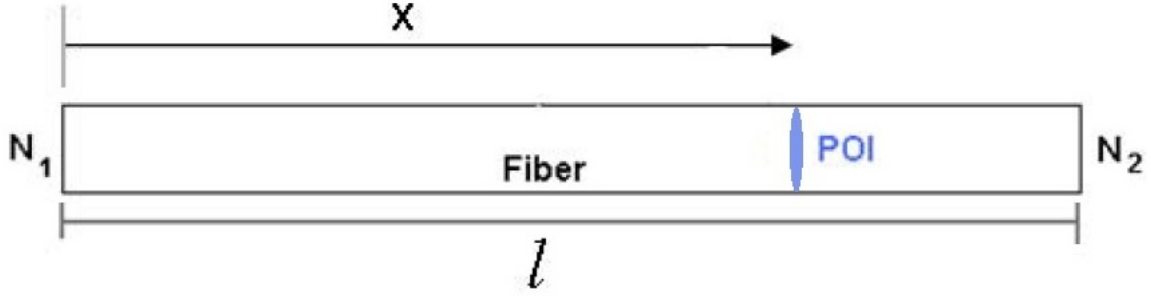


Figure 6. An illustration of the the dual ended fiber readout variables. The position-of-interaction (POI) occurs at a distance x from end ‘1’ (i.e. left end). The scintillation yields at each end are N_1 and N_2 . The figure is recreated and adapted from Capt Jones thesis [3].

The energy deposited by the incident radiation is estimated by the use of photon counting by a photosensor (e.g. PMT or SiPMT). The estimation is simplified by the fact that photosensors have a linear response to light entering the photosensor detection window. This means that the measured readout from the photosensor is proportional to the scintillation photons entering the photosensor escaping the scintillating fiber. The calculations from Equation 22 only provide estimates of the number of photons created from the induced scintillation event and there are uncertainties associated with these calculations. Basic error propagation derivations of energy with respect to time and position can be used in parametric studies to determine the amount of time and position sensitivity for an ideal TOF neutron spectrometer. These derivations and approximations are explained in greater detail in Section 2.7.

2.4 BCF-12 Plastic Scintillating Fibers

The creation of plastic scintillators involves the dissolution of an organic scintillator in a solvent, which is then polymerized. The fibers used in these experiments and investigations are produced by Saint-Gobain. They are the BCF-12 plastic scintillating fibers, which are mainly comprised of a polystyrene based core and an acrylic polymethylmethacrylate (PMMA) cladding. Optical “cross-talk” can be reduced by

applying an external extra mural absorber (EMA), however, the BCF-12 plastic scintillating fibers used in this research do not have an EMA layer. The fluorescent dopants chosen as part of the fiber core produce the desired scintillation and radiation-resistance characteristics. However, when one scintillation property is increased the other is often sacrificed to achieve the desired result. The fluor concentration is increased in the small fibers (i.e. diameter is less than 0.5 mm). The consequence of an increased amount of fluor is a decrease in the light attenuation length [11]. Saint-Gobain provides a schematic for how their typical round plastic scintillating fibers are constructed. This schematic is recreated and adapted in Figure 7. The more important properties and specifications of the BCF-12 fibers used in this research are displayed in Table 3.

Table 3. Saint-Gobain’s BCF-12 plastic scintillating single-clad fiber properties [11].

Property	Value
Core Material	Polystyrene
Core Refractive Index	1.60
Density	1.05 g/cm ³
Cladding Material	Acrylic
Cladding Refractive Index	1.49
Cladding Thickness	3% of Fiber Diameter
Numerical Aperture	0.58
Trapping Efficiency	3.44% Minimum
No. of H atoms/cm ³ (Core)	4.82×10^{22}
No. of C atoms/cm ³ (Core)	4.85×10^{22}
No. of electrons/cm ³ (Core)	3.4×10^{23}
Radiation Length	42 cm
Emission Color	Blue
Emission Peak	432 nm
Decay Time	2.7 ns
1/e Length	2.2 m
No. of Photons/MeV	8000
Operating Temperature	−20°C to +50°C
Vacuum Compatible	Yes

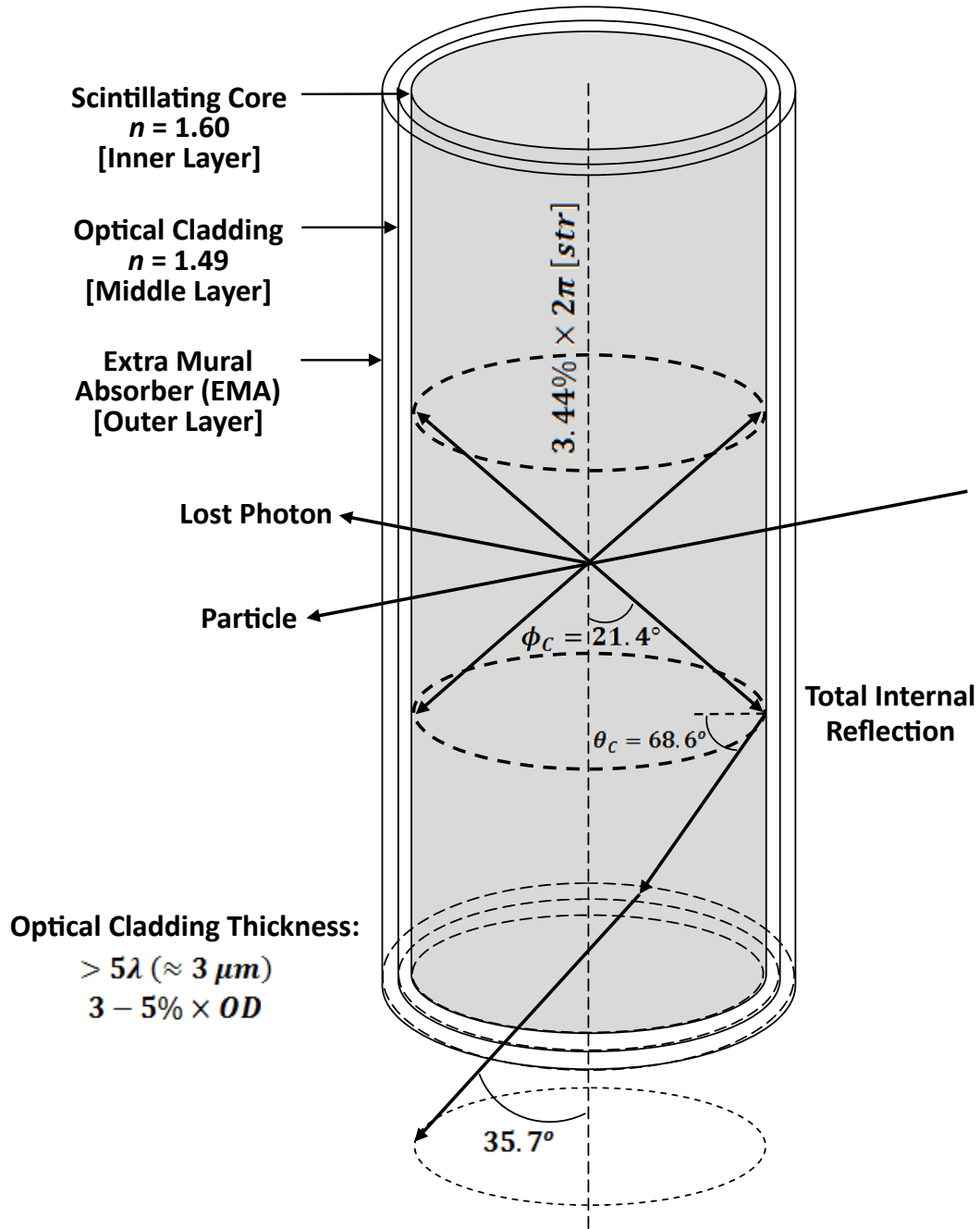


Figure 7. A diagram of a typical Saint-Gobain Crystals, Inc. plastic scintillating fiber. Some properties of interest are the refractive indices of the core and cladding, as well as the critical cone angle ($\phi_C = 21.4$ deg). Scintillation photons generated between zero degrees and the critical angle will experience total internal reflection through both axial directions of the fiber. Scintillation photons that reach the ends of the fiber with an angle between zero degrees and the critical cone angle ($\phi_C = 21.4$ deg) will exit (i.e. escape) the fiber at the ends. The broadening of the angle to 35.7 deg is a result of Snell's Law and is calculated using the equation for the numerical aperture (Equation 17). This photo is reproduced with permission from Saint-Gobain's brochure for their scintillating fiber products [11].

The cladding material used by Saint-Gobain’s plastic scintillating fibers is PMMA, which has the molecular formula $C_5H_8O_2$. These fibers possess a density, ρ , of 1.2 g/cm^3 and a refractive index, n , of 1.49. The geometrical shape and size of the fiber determines the thicknesses of the optical cladding. In this research, round fibers with diameters greater than 0.20 mm are used, which have a PMMA cladding thickness of 3–5% of the fiber’s outer diameter (i.e. fiber core, cladding, and EMA, if the EMA is applied). The trapping efficiency of the scintillating fibers are determined by the refractive indices of the core and cladding, as well as the cross section of the fiber. There is also another factor to consider in determining the trapping efficiency. Since not all scintillation events occur along the fiber axis, the distance between the fiber axis and the scintillation event will cause an increase in trapped scintillation photons. Saint-Gobain quotes the trapping efficiency for their round scintillating fibers as 3.4% to $\sim 7.0\%$ [11]. The range depends on the location of the scintillation event, the trapping efficiency is 3.4% at the fiber axis and increases as you travel radially out from the fiber axis to $\sim 7.0\%$ at the core-cladding boundary.

The “cross-talk” between the scintillating fibers can cause error in the signals. Cross-talk occurs between adjacent optical fibers when scintillation photons leave one fiber and enter another fiber. This can cause errors in measurement since it is a form of photon leakage, and if position measurements are desired based on a specific optical fiber interactions. A way to reduce this fiber cross-talk is to apply an exterior coating to the optical fiber. The EMA is usually applied in thickness between 10 to 15 microns. The extra mural absorber coating has the negative consequence of decreasing the overall intensity of the signal obtained from a fiber. The greatest reduction in signal intensity is observed with black EMA and/or with short fibers. Another adverse affect of EMA coatings include reduced light-piping in the cladding. The black and white EMA coatings have differing uses based on the desired application. Black EMA,

when applied near the fiber ends, is used to flatten out position dependent response, while white EMA is used when building short fiber imaging bundles [11].

2.5 Photon Detection Techniques

The light produced in a scintillator from radiation is commonly collected and read by photomultipliers (PMTs). While PMTs have the advantage of a large window area and high gain, they have limited quantum efficiencies, high operating voltages, and are susceptible to magnetic fields. These fundamental limitations provide the need for other high-gain photon counting detectors. The optical photon readouts of thin organic plastic scintillating fibers, such as BCF-12 which emits in the blue, or inorganic scintillating fibers, such as YAG:Ce which emits in the green, are more suited to recently developed photosensors. Silicon photomultipliers have demonstrated better response and higher quantum efficiencies compared to PMTs, as shown in Figure 8.

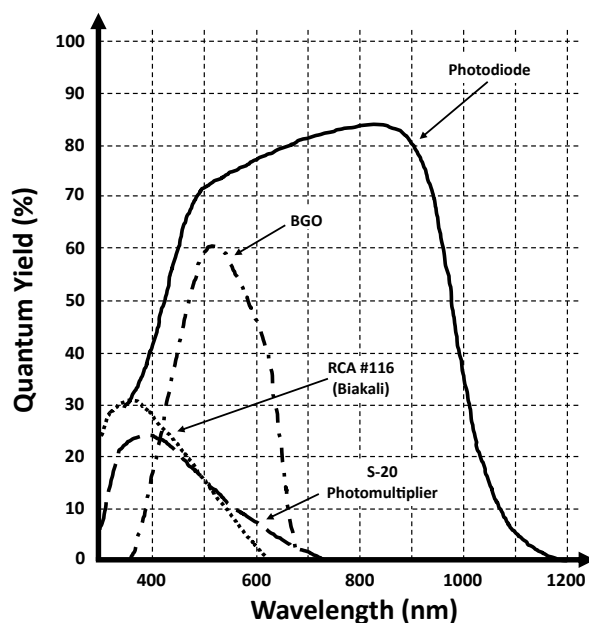


Figure 8. The spectral response of a photodiode and PMT. The response of the photodiode is better suited for emission across the entire light spectra, whereas the PMT and Biakali PMT are only suited for the violet and blue. For reference the BCF-12 plastic scintillating fiber peaks at 435 nm, as shown in Figure 12. The plot is reproduced with permission from Knoll [6].

2.5.1 Photomultiplier Tubes.

Photomultiplier tubes provide the conversion and multiplication of photons into photoelectrons. The photocathode performs the conversion. The spectral response of a PMT is a function of PMT window material and photocathode materials. The photocathode in a PMT converts the incident light energy into photoelectrons with the efficiency of the conversion dependent on the incident wavelength of light. Photomultiplier tubes are typically less sensitive to longer wavelength (i.e. green through red) due to the reduction of light absorption by the photocathode and the relatively low energy imparted by the photoelectrons, they are more sensitive to shorter wavelength (i.e. violet and blue) light.

The time characteristics exhibited by a PMT are determined by the electron trajectories since the time required for photoemissions is very short lived. The transit time of an electron in a PMT is derived from the average time difference between the photon arriving at the photocathode and the burst of electrons at the anode. An important characterization quantity, with respect to timing properties for PMTs, is the spread or distribution in electron transit time. This timing characteristic of the PMT is vital in determining the time width of the pulse of electrons arriving at the anode.

The voltage pulse shape produced at the anode of the photomultiplier after a scintillation event depends on the time constant of the anode circuit. As a result, two extremes can occur; the first occurs when the anode time constant, $\tau \equiv 1/\theta$, is very large compared to the decay time, λ , of the scintillator (i.e. $\theta \ll \lambda$), and the second occurs when the anode time constant is much smaller than the decay time of the scintillator (i.e. $\theta \gg \lambda$). These two extremes are shown in the top three plots of Figure 9.

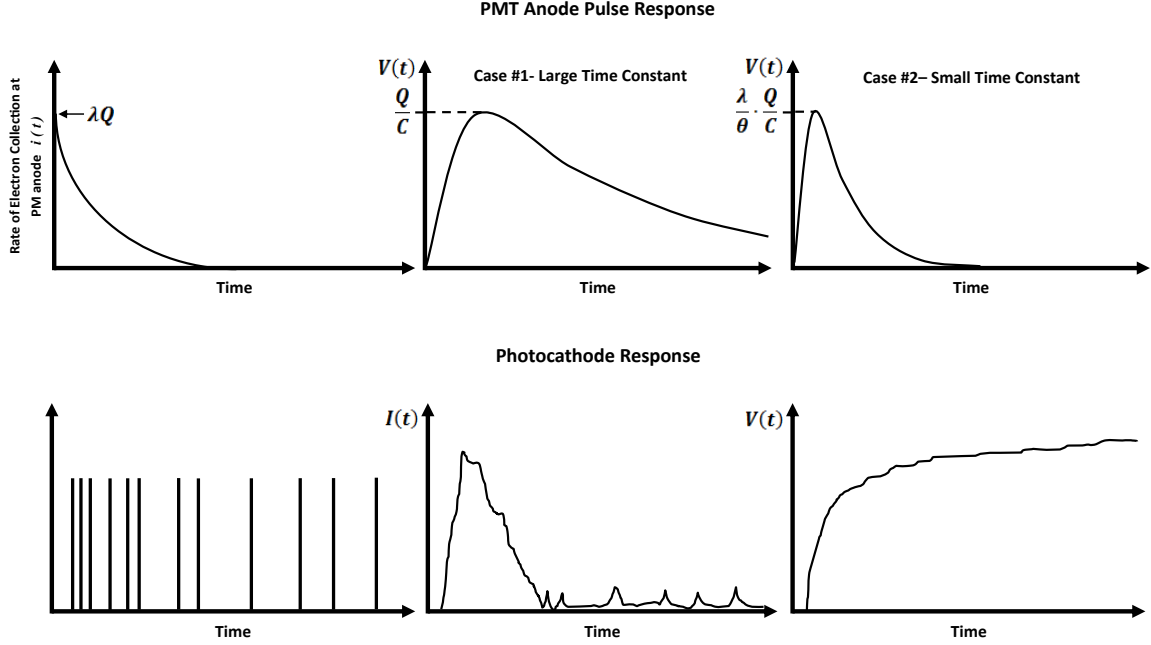


Figure 9. Top Three: Plots of voltage over time for a PMT anode pulse response at the two extremes of (*Middle*) Case 1: Large and (*Right*) Case 2: Small anode time constants. The plots are recreated and adapted from Knoll [6]. Bottom Three: Plots of the response exhibited by a photocathode. (*Left*) Response of photocathode, where individual electrons are leaving the photocathode. (*Middle*) Current at the anode after the multiplication of electrons. (*Right*) Leading edge of voltage pulse across anode circuit with large time constant. The plots are reproduced with permission from Knoll [6].

In Figure 9, when the anode time constant is very large (i.e. $\theta \ll \lambda$), the response from the PMT resembles the top middle plot (Case #1); however, when the anode time constant is very small (i.e. $\theta \gg \lambda$), the response from the PMT resembles the top right plot (Case #2). The PMT integrates all the light from the scintillator, thus the resultant output produced is discrete pulses which are shown in the bottom middle plot of Figure 9. In cases where the PMT system response is well-known by the user, post-processing of the output information can utilize deconvolution techniques to extract individual scintillation event pulses.

2.5.2 Silicon Photomultipliers.

Photodiodes are used to detect and measure light, making them ideal instruments to measure the response of scintillators to radiation induced events. Impact ionization is the physical mechanism used for avalanche gain in photodiodes, which occurs when the electric field in the depletion region is strong enough to have an electron transfer enough energy to a bound valence electron to ionize it. An electron-hole pair is created, thus producing current gain large enough to be measured. Additional carriers can potentially gain enough energy from the electric field to produce more impact ionization. This creates an avalanche of electron-hole pairs. The amount of electron-hole pairs in the photodiode depletion region is directly proportional to the number of incident scintillation photons upon the photosensor's active region.

An avalanche photodiode (APD) is a p-n junction diode subjected to a large reverse bias voltage. The Geiger operating region is reached when the bias voltage is set to a level greater than the “breakdown voltage.” A large ballast resistor is placed in series with the APD to quench the photodiode. A charge integrating preamplifier is used to readout the signal generated by the APD, however, the APD can also be directly readout from a load resistor [14]. A Geiger-mode avalanche photodiode (G-APD) is capable of measuring single-photon events. Larger multiplication factors are used to achieve signals large enough to be measured directly. In this research, however, charge sensitive preamplifiers are used to increase the signal. A schematic showing the readout circuit for a Geiger-mode APD is provided in Figure 10.

The silicon photomultipliers used in this research are the Hamamatsu S10362-11-025C. This SiPMT is a new type of photon-counting device made up of multiple APD pixels operated in Geiger mode. The SiPMT is an opto-semiconductor device with excellent photon-counting capability, low voltage operation, and insensitivity to magnetic fields. The characteristics of this SiPMT are found in Table 4.

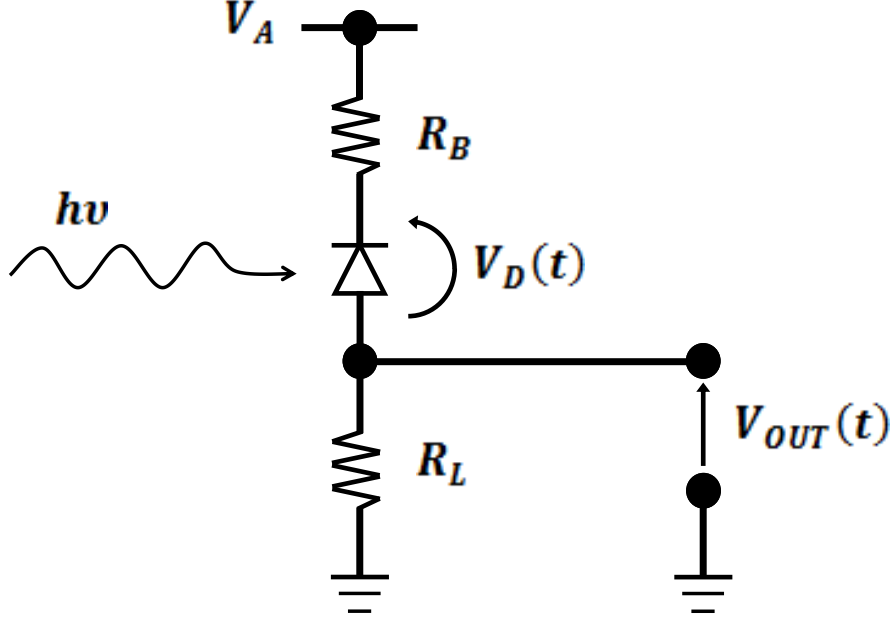


Figure 10. A general depiction of a readout circuit for a Geiger-mode APD. V_A is the bias voltage, R_B is the ballast resistor, $h\nu$ is the photon incident on the APD which generates a voltage V_D across the APD, R_L is the load resistor across which V_{OUT} is measured. The circuit is reproduced with permission from Cova et. al. *Evolution and prospects for single-photon avalanche diodes and quenching circuits* [14].

Table 4. Characteristics of the Hamamatsu S10362-11-025C SiPMT [15].

Parameter	Value
Effective Active Area	1 x 1 mm
Number of Pixels	1600
Pixel Size	25 x 25 μm
Fill Factor	30.8 %
Spectral Response Range	320-900 nm
Peak Sensitive Wavelength	440 nm
Photon Detection Efficiency	25 %
Operating Voltage Range	70 \pm 10 V
Dark Count	300 kcps
Dark Count Max.	600 kcps
Time Resolution (FWHM)	200 – 300 ps
Gain	2.75×10^5

2.6 Digital Data Acquisition

This section discusses the methods, techniques and equipment utilized to collect data in the experiments. The raw pulses can be measured directly from the detector, but in this case the pulses were measured after passing through charge sensitive preamplifiers to a digital oscilloscope (Tektronix DPO7104). The characteristics and specifications of the Tektronix DPO7104 obtained from the manufacturer's manual [16] is shown in Tables 5 and 6. The data can be saved digitally to the oscilloscope's internal memory and then post-processed later by the user. Once the data is saved the response of the analog pulse-shaping electronics can be implemented by data processing algorithms.

Digital data acquisition can help in reducing detection system noise due to the fact that it has the potential to bypass the preamplifiers, linear amplifiers, and shaping amplifiers. All of these will add another component of noise to the signal as it propagates through the system. Valuable timing information is lost when measuring very fast events from the detector when the signal passes through more amplification components. The data acquired in these experiments passed through charge sensitive preamplifiers before being collected by the digital oscilloscope. The detection system setup used in these experiments and investigations is shown in Figure 11.

There are multiple advantages to utilizing this equipment for fast digital data acquisition. The Tektronix DPO7104 has an extremely high sampling rate, a max of 20.0 GHz, and is thus able to obtain a time resolution as low as 200 picoseconds per data point (i.e. 0.2 nanoseconds per data point). Another advantage of this equipment is the FastFrameTM acquisition capability. If this setting is activated, thousands of individual waveforms per second can be measured and stored in the oscilloscope's internal buffer. The capabilities of the FastFrameTM acquisition are only bounded by the size of the oscilloscope's internal memory and its sampling rate. The third

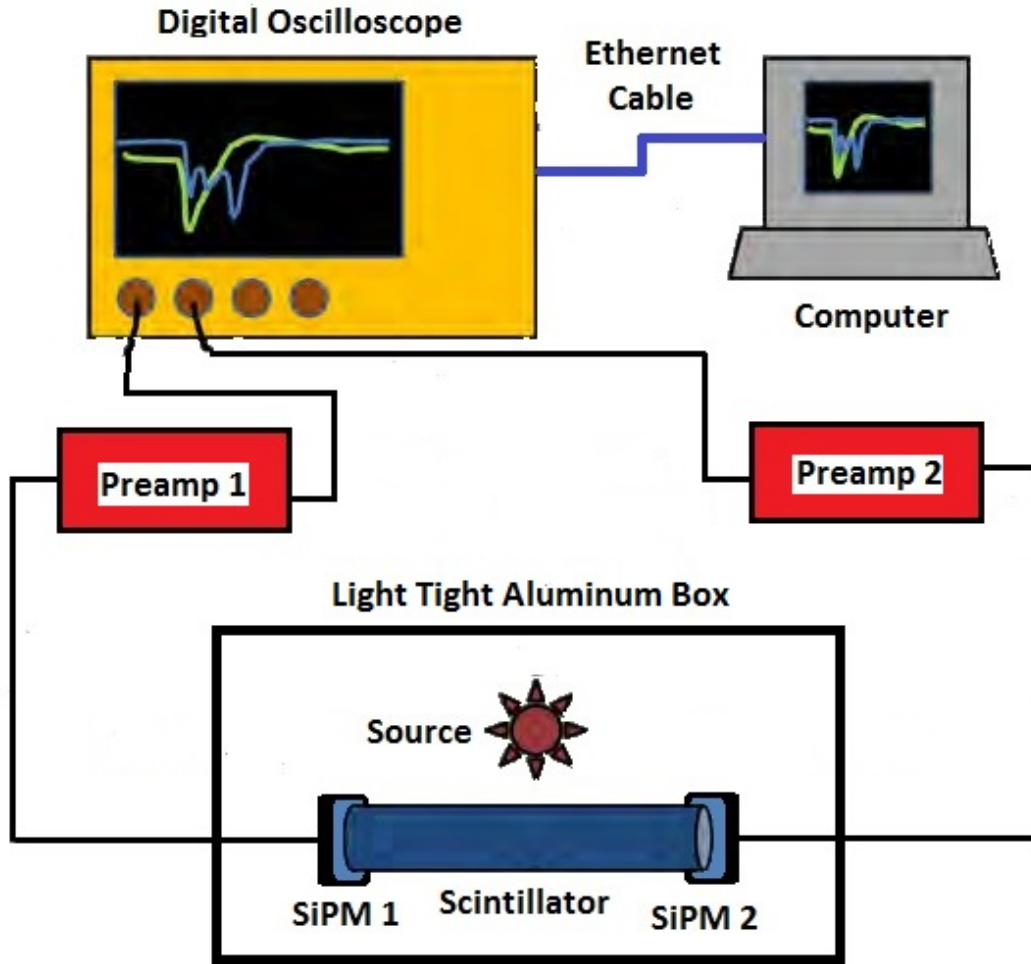


Figure 11. A diagram of the dual-ended SiPMT readout using digital data acquisition. The light output from the scintillator is converted into voltage pulses by the SiPMTs, which are then passed through and multiplied by the fast pre-amplifiers and then measured by the digital oscilloscope. The digital oscilloscope captures a set number of waveforms digitally in its internal buffer and then transfers the internal buffer to the computer via a gigabit Ethernet connection. The digital oscilloscope is controlled by the computer through TekVISA via a list of commands created in a MATLAB *.m file.

and final advantage of the Tektronix DPO7104 oscilloscope is the ability to configure and declare every setting on the oscilloscope through Virtual Instrument Software Architecture (VISA) commands. Software programs for numerical computation (e.g. MATLAB or LabVIEW) have built in VISA interfaces compatible with the Tektronix DPO7104. MATLAB contains instrument drivers that can be utilized to directly control instruments like the Tektronix oscilloscope. The VISA or Tektronix Virtual

Table 5. Vertical axis acquisition specifications for the Tektronix DPO7104 digital oscilloscope used during these experiments and investigations [16].

Component	Setting
Input Channels	4
Bandwidth	1 GHz
Rise Time 10% to 90% (Typical)	300 ps
Rise Time 20% to 80% (Typical)	200 ps
DC Gain Accuracy	$\pm 1\%$ with offset/position set to 0
Bandwidth Limit	2 GHz
Input Coupling	AC, DC, GND
Input Impedance	$1\text{ M}\Omega \pm 1\%$ with $13\text{ pF} \pm 2\text{ pF}$, $50\ \Omega \pm 1\%$
Input Sensitivity	$1\text{ M}\Omega$: 1 mV/div to 10 V/div $50\ \Omega$: 1 mV/div to 1 V/div
Vertical Resolution	8 bit (> 11 bit with High Resolution)
Max Input Voltage, $1\text{ M}\Omega$	150 V CAT I, de-rate at 20 dB/decade to $9 V_{RMS}$ above 200 kHz
Max Input Voltage, $50\ \Omega$	$5 V_{RMS}$, with peaks $\leq \pm 24\text{ V}$
Position Range	± 5 divisions
Delay between any Two Channels	$\leq 100\text{ ps}$ ($50\ \Omega$)

Table 6. Horizontal axis acquisition specifications for the Tektronix DPO7104 digital oscilloscope used during these experiments and investigations [16].

Component	Setting
Max Sample Rate (1 Channel)	20 GS/s
Max Sample Rate (2 Channels)	10 GS/s
Max Sample Rate (3-4 Channels)	5 GS/s
Max Equiv. Time Sampling Rate	4 TS/s
Max Record Length with Std Config.	50 M (1 Channel), 25 M (2 Channels), 12.5 M (3-4 Channels)
Time Base Range	50 ps/div to 1000 s/div
Time Resolution (in ET/IT mode)	500 fs
Time Base Delay Time Range	5 ns to 250 s
Trigger Jitter (RMS)	1.5 ps_{RMS} with enhanced trigger OFF $< 100\text{ fs}_{RMS}$ w/ enhanced triggering ON
Max FastAcq Wvfrm Capture Rate	$> 250,000\text{ wfms/s}$ with 4 Channels
FastFrame Acquisition	Acq memory divided into segments; maximum trigger rate $> 310,000\text{ wfms/s}$. Time of arrival recorded with each event. Frame Finder helps visually ID trans.

Instrument Software Architecture (TekVISA) interface is independent of instrument drivers and will work as long as the controller (e.g. MATLAB, C++, or Fortran) and the instrument (e.g. Tektronix DPO7104, Hewlett-Packard, National Instruments) are VISA compliant. The MATLAB/TekVISA interface allows complete control of every feature of the DPO7104 as if the user were manually measuring signals on the oscilloscope. Typical adjustments on the oscilloscope itself include voltage scale (y-axis), time scale (x-axis), resolution, trigger settings, voltage offset, time offset, and waveform positioning to get the oscilloscope to display all the desired features of a waveform. These commands can be programmed into a MATLAB script to call up and configure these settings when the MATLAB script file is run. Using a MATLAB script allows for an easy change in settings when different parameters (e.g. scintillator material, radioactive source, or photosensor) of an experiment are used.

2.7 Spatial and Timing Resolution

This section pertains to the uncertainty approximations in the spatial and time domain and how the uncertainty affects the energy calculation and its uncertainty. A neutron spectrometer which can back-trace the trajectories and energy of the incident neutron radiation relies on precise spatial and timing measurements. If the theoretical parameters of precision for space and time can be bounded and characterized a range of limitations for the proposed time-of-flight neutron spectrometer can be proposed and compared to experimental results. The spatial and time uncertainties are derived and combined to determine the net effect each has on the energy and its uncertainty. The kinetic energy of a neutron is

$$E_{KE} = \frac{1}{2} m v^2 = \frac{1}{2} m \left(\frac{dz}{dt} \right)^2 = \frac{1}{2} m \left(\frac{dz^2}{dt^2} \right). \quad (23)$$

Let us first consider the spatial uncertainty (dz) component and hold the timing

uncertainty constant, while taking the derivative of kinetic energy with respect to position. In this case, dz is used as the convention for position instead of dx or dy because the cross-section of a long fiber bundle array is considered the xy-plane

$$\begin{aligned}\frac{d}{dz}(E) &= \frac{d}{dz} \left(\frac{1}{2} m \frac{dz^2}{dt^2} \right) \\ \frac{dE}{dz} &= m \frac{dz}{dt^2}.\end{aligned}\tag{24}$$

One assumption made in the derivation of Equation 24 is that the uncertainty in the xy-plane, dx and dy , is neglected due to the small diameter of the fibers. The fibers have a diameter of 0.25 mm, which gives the 14×14 fiber bundle array an overall width and height of 3.5 mm. Now, lets consider the timing uncertainty (dt) component and hold the spatial uncertainty constant, while taking the derivative of the kinetic energy with respect to time

$$\begin{aligned}\frac{d}{dt}(E) &= \frac{d}{dt} \left(\frac{1}{2} m \frac{dz^2}{dt^2} \right) \\ \frac{dE}{dt} &= -m \frac{dz^2}{dt^3}.\end{aligned}\tag{25}$$

Using error propagation to solve for the uncertainty in calculating the kinetic energy the uncertainty in space and time are accounted for as

$$\sigma_E^2 = \left(\frac{dE}{dz} \right)^2 \sigma_z^2 + \left(\frac{dE}{dt} \right)^2 \sigma_t^2.\tag{26}$$

Inserting Equations 24 and 25 into Equation 26 and taking the square root of both sides of the equation solves for the uncertainty in energy, σ_E , resulting in

$$\sigma_E = \sqrt{\left(m \frac{dz}{dt^2} \right)^2 \sigma_z^2 + \left(-m \frac{dz^2}{dt^3} \right)^2 \sigma_t^2}.\tag{27}$$

III. Experiment & Simulation Methodology

The details concerning the modeling and simulation of a single BCF-12 scintillating fiber and a 14×14 fiber bundle along with its design and construction are presented in this chapter. The experimental procedures and setup for the digital oscilloscope dead time and acquisition characteristics is developed and discussed. In addition, the methodology of the parametric studies concerning the spatial and timing resolution are formulated and presented. This chapter concludes with the single BCF-12 fiber dual-readout SiPMT experimentation, including the SiPMT circuit design, construction, and dark count verification.

3.1 Modeling a Single BCF-12 Fiber

Geant4 is a Monte Carlo tool initially developed at CERN to describe the interactions of particles in high energy physics experiments. The code has many applications pertaining to interactions found in space, radiation effects on microelectronics, and nuclear physics. In this research Geant4 is used to understand the neutron scattering efficiency of the scintillating fibers, the amount of energy deposited by the interactions, the amount of scintillation light created, and finally the amount of optical photons that reach the ends of the fiber. With this information the simulated response of the scintillating fiber to neutron interactions can be understood.

The BCF-12 fiber was modeled to understand the creation of scintillation events as a result of neutron scattering in a single fiber. More importantly, the number of double scatter neutrons and the amount of energy deposited with each scattering event was modeled. With such a model, we can determine the double scatter efficiency, as well as change the position of the external neutron source to find more trajectories that favor increased double scattering events; which is discussed in Section 3.2.

3.1.1 Simulation of an Internal Optical Photon Source.

A single plastic scintillating fiber (BCF-12) was modeled in Geant4 to understand how optical photons generated by scintillation events travel axially to the fiber's ends. The single fiber was given the same dimensions and material properties provided in Table 3, of Section 2.4. The fiber was modeled as polystyrene with an acrylic cladding located in a vacuum. The cladding of the BCF-12 fiber, also known as PMMA, has a chemical composition of $C_5H_8O_2$ and a density of 1.2 g/cm^3 . Providing these material properties allowed Geant4 to properly construct and model the PMMA cladding of the BCF-12 fiber. The fiber scintillator is adequately defined in Geant4 using six parameters, which are the optical photon emission energy, core refractive index, cladding refractive index, environment refractive index (e.g. air or vacuum), absorption length (i.e. $1/e$ length), and the emission fraction. These parameters are defined as 'energyrange,' which is the range of optical photon energies emitted by the scintillator; 'rindexcore,' which is the refractive index of the scintillator core material; 'rindexclad,' which is the refractive index of the scintillator cladding material; 'rindexair,' which is the refractive index of the surrounding environment (e.g. air, in this case); 'absorption,' which is the scintillator attenuation length (i.e. $1/e$ length); and 'emission,' which is the normalized fraction of total optical photons emitted at a specific energy (i.e. wavelength).

The isotropic optical photon source was set to generate 1×10^5 photons with a mono-energetic energy of 2.74 eV to gather quick initial results. The photon source was then changed to generate 1×10^6 photons for better counting statistics. The photons were set to a mono-energetic value of 2.74 eV (i.e. $\sim 452 \text{ nm}$), which is the average value of the optical photon emission energy distribution provided by Saint-Gobain [11]. The absorption length was defined as 270 cm for each energy point. The refractive indices of the core, cladding, and air for each energy point were held

constant at 1.60, 1.49, and 1.00, respectively. The values for the refractive index of core and cladding were obtained from Table 3. Finally the emission fraction was set to 1.00, due to the fact that all the optical photons are mono-energetic.

The simulation traced the path of the optical photons from their generation point at the center of the fiber to the ends where the light is detected. Geant4 is used to test the trapping efficiency by constructing two “detector” surfaces placed at each end of the fiber. As a photon is transported from the fiber core volume, through the core-detector interface, into the “detector” volume a tally is recorded. The summation of these tallies provide the fraction of generated optical photons which traversed through the fiber from generation to the fiber ends. While the results from this model provide insight into how optical photons transit down the fiber, they do not provide information about where and how light is produced from neutron scattering events. To study these effects, a second Geant4 model using an external neutron source was developed.

3.1.2 Simulation of an External Neutron Source.

Building upon the previous Geant4 model, the internal optical photon source was removed and replaced with an external fan beam neutron source located 1 cm from the center of a single scintillating fiber. The fan beam was used so that Geant4 didn’t have to generate and track neutrons that did not have a chance of intersecting the 500 μm diameter, 30 cm long plastic scintillating fiber. Unlike the previous simulation, this model now introduces the true emission spectrum produced from scintillation events in the fiber. The emission spectrum for BCF-12 is shown in Figure 12, which indicates a peak emission around 435 nm (blue emission). The neutrons are modeled as monoenergetic neutrons at 2.5 MeV, which corresponds with the energy of the neutrons produced in the D-D neutron generator located on AFIT’s campus.

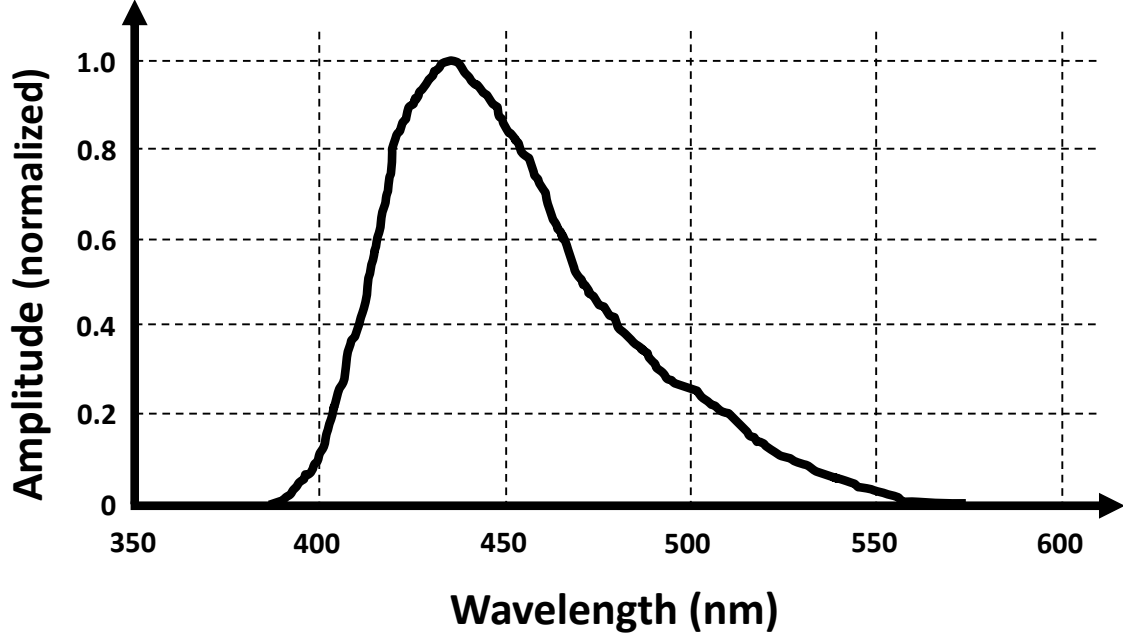


Figure 12. The emission spectra of the BCF-12 plastic scintillating fiber. Eight points were taken from the distribution to describe the function in Geant4. The wavelengths were converted to energy for the correct input type into the Geant4 model. The emission band of approximately 385–575 nm correspond to energies of 3.22–2.16 eV, respectively. The amplitude is normalized. The distribution was reproduced with permission from Saint-Gobain’s scintillating fibers brochure [11].

To correctly capture the distribution in Figure 12, eight “energy points” (i.e. wavelengths) were chosen and given a refractive index value for the core, cladding, and air, as well as the absorption length, and fraction of total optical photon emission at each energy value. The eight points which define the BCF-12 emission spectra are found in Table 7. The energy range, absorption and emission values were taken from Saint-Gobain’s published brochure on scintillating fibers [11]. These parameters are used by Geant4 to describe all the optical properties of the polystyrene scintillating fiber, which is necessary for optical photon generation and transport.

Detector surfaces, used for tallying, are placed at both ends of the fiber to count the number of photons that a real photosensor may detect from neutron induced scintillation events. While this information is useful for understanding light production and transport in the fiber, there are some other parameters of interest that must be

Table 7. Optical emission properties used in the Geant4 model to define the BCF-12 plastic scintillating fiber. The BCF-12 optical properties were defined in Geant4 by breaking the emission distribution (Figure 12) into 8 points. The six parameters (only two shown here) defining the optical properties require a value at each of the 8 points. The units column represents the unit multiplier required by Geant4 to define the units of all the values contained within the respective parameter (i.e. row).

Parameter	Value								Units
energyrange	3.02	2.98	2.83	2.74	2.51	2.39	2.28	2.18	(.*eV)
emission	0.030	0.078	0.769	1.000	0.430	0.233	0.100	0.048	—

characterized in order to assess a fiber bundle for use as a time-of-flight spectrometer and imager. In particular, it is important to know when and where neutrons interact and the amount of energy deposited at each collision. After preliminary tests with the single fiber model, it was expanded by incorporating multiple fibers to create a model of a 14×14 BCF-12 fiber array.

3.2 Modeling of the BCF-12 Fiber Bundle Array

A 14×14 BCF-12 scintillating fiber array model was built to understand the expected number of double (or greater) neutron scattering events possible in a packed fiber bundle. This model provided information about the position, speed, and energy imparted by the neutrons interacting with the fiber array. The model provides insight into the efficiency of double scatter events in the bundle. It should be noted that only elastic neutron scattering events were recorded for this model. Using a model where only elastic neutron scattering occurs will yield incomplete results since there would normally be inelastic neutron scattering by carbon, which is a complex issue, and oxygen, which creates prompt gammas and charged particles detectable by the scintillator.

The output file from this model was post-processed using a MATLAB script, located in Appendix A, designed to extract key parameters of interest. The infor-

mation extracted by the script included the number of single, double, triple (and greater) neutron scatters, the distance between scatters, and the energy deposited by the neutron in each scatter. From this information, distributions of scattering events can be determined. Additionally, the distance between scatters was binned with the corresponding energy to understand the distribution of distances traveled for a given neutron energy. A comparison was also drawn between the Geant4 energy of the neutron and the calculated energy of the neutron, which was determined from the distance between scatters divided by time between scatters (i.e. the velocity of the neutron). If the velocity of the neutron is known then the kinetic energy is easily determined. A comparison of the kinetic energy output by the model and calculated kinetic energy (using the time required for a neutron to travel between scatter points) is made to observe any possible differences in neutron energy. If there are any differences, it could indicate a flaw in the simulation from incorrect user parameter input or basic computational errors in the post-processing.

3.3 Construction of a 14×14 BCF-12 Fiber Bundle Array

After analyzing the results of the Geant4 fiber bundle models, a 14×14 fiber bundle was built using BCF-12 fibers from Saint-Gobain. Although not tested during this research, the bundle will be used in future measurements at AFIT's D-D neutron generator to confirm simulation results. Each fiber in the bundle has a 500 micron diameter, and is 30 cm long. They are then arranged into a square pack 14×14 array, which gives a cross section of $\sim 7 \times 7$ mm. These dimensions were based on a length and cross sectional area suitable to identify the position of interaction within the bundle with a total intrinsic efficiency of greater than $2.0 \pm 0.2\%$ [2]. In an attempt to maintain uniformity of design, a master bundle key was made for repeated duplication of correct length fibers. A long and straight groove was notched

into a piece of wood and a perpendicular notch at 30 cm was made for consistency. The wooden master key is shown in Figure 13. The spool was laid into the master key flush to the left and gently pressed into the groove, it was then cleaved at the perpendicular groove 30 cm to the right. The ends were cleaved using a hot knife. The hot knife is essentially a soldering iron or wood burning kit with an attachable exacto knife tip. The hot knife was used instead of scissors, a regular knife, or wire cleavers because it cleans and quickly cleaves the plastic fibers without the requirement to polish the ends afterward. Essentially the hot knife polishes the surface while cutting the fiber [17]. This process was repeated until all of the 500 micron diameter BCF-12 fiber was cut. This totaled 222 pieces of 30 cm long fiber; 196 of these fibers were used for the creation of the 14×14 array; while 25 fibers were used in a 5×5 array, which served as a test bundle to practice the best way to assemble and glue the bundle for strength and rigidity. The last fiber was kept as a spare in case any of the fibers were damaged in the process of building the fiber array.

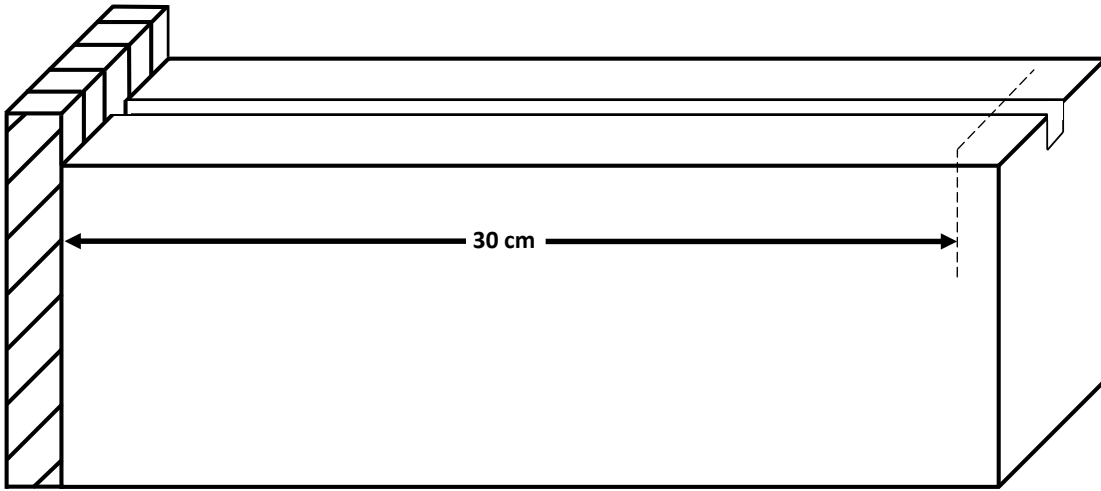


Figure 13. Illustration of the master key. The master key was made out of wood and was used for consistent 30 cm long fiber cuts. The notch along the top was made by drawing a line with a pencil and using a knife to cut down into the wood. The fiber was pulled off of the spool and set flush with the left side (depicted with diagonal lines). The fiber was gently pressed into the groove and cut at 30 cm lengths (designated by the dotted line).

With the single fibers all cut to 30 cm the construction of the 5×5 and 14×14 arrays could begin. The main focus was to ensure consistency with layers so that all ends matched up and were aligned in a square matrix. Careful attention was given to ensure the fibers lined up directly next to and above each other, so that there would not be any fibers shifting into the natural grooves that were created when placing cylindrical fibers next to each other. Double sided tape was placed on a clean table surface. Two small pieces ($\sim 5 \times 5$ fibers in length and width) were placed on each end, flush to the cut edges of the row of fibers. An additional two pieces of double sided tape, approximately the same size, were placed equidistantly apart between the previous two pieces of double sided tape. A total of four pieces of tape per layer were applied (one at each end and two in the middle) thus creating three equidistant (~ 10 cm) sections. A single fiber was placed down making contact with each of the four pieces of double sided tape. Each following fiber was placed next to the previous fiber, ensuring continuous contact with the adjacent fiber and maintaining the four tape contact points until a row of five fibers was formed. Four more pieces of double sided tape were placed on top of the newly formed row of fibers. This process was continued until a 5 row by 5 column fiber bundle array was created, shown in Figure 14. The process proved successful and consistent, so it was utilized in making the larger 14×14 array fiber bundle. Figures 15 and 16 show the finished result of the 14×14 array fiber bundle.

The bundles took on a square rod shape, however, they would slightly deflect along the axis of the rod due to the fibers being wound around a large spool. To straighten out the deflection, white Elmer'sTM glue, wooden blocks, and a hot air gun were used to press and adhere the square rod into a straighter form. This was performed by pressing the array against two blocks while applying, only slightly, a little hot air to remold the structure. The fibers would heat up just enough to be pliable, before

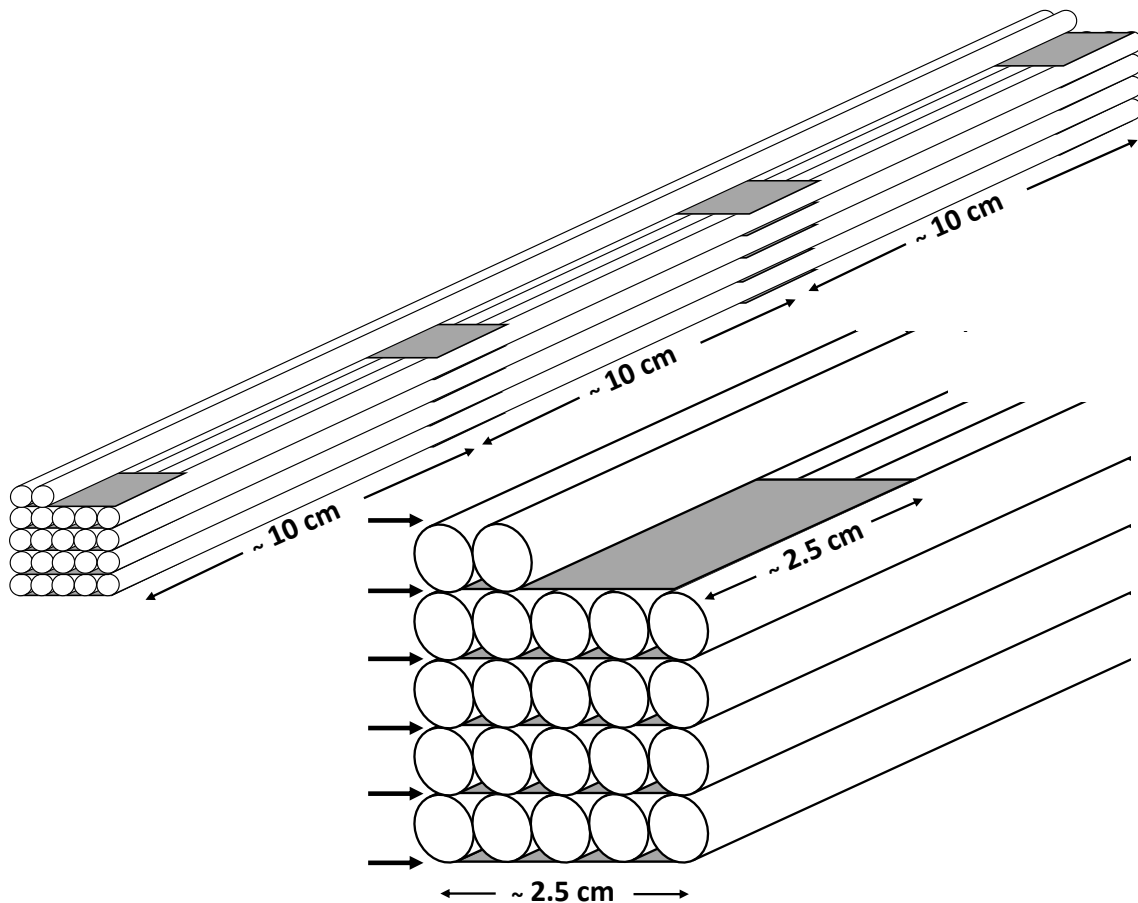


Figure 14. Illustration of the construction of the 5×5 fiber array. The entire bundle is ~ 30 cm long with four pieces of double sided tape, placed ~ 10 cm apart, holding each layer (i.e. row) of fibers. The bottom right is a larger view of the fiber array end. The tape is $\sim 2.5 \times 2.5$ cm in dimension (denoted in gray). The arrows on the left of enhanced image denote the locations of the tape. Note: the fiber bundle is not completely assembled in this image nor drawn to scale for illustrative purposes.

quickly cooling. After this quick procedure the Elmer'sTM glue was applied using a paintbrush, to ensure all fibers were attached to one another in a square matrix. The glue was allowed to dry for an hour. After each side had an hour to dry the bundle was rotated one quarter of a turn (i.e. 90 deg) about its axis to apply hot air for remolding and Elmer'sTM glue for adhering the next side of the square rod fiber bundle. The heating and gluing process was repeated several times, with each side receiving multiple applications of heat and adhesive, until the square rod was straight and hardened with glue, ensuring the fiber bundle no longer deflected.



Figure 15. The “xy-plane” cross-sectional view of the 14×14 BCF-12 fiber bundle array. Each fiber is 500 micron (0.5 mm) in diameter, thus having an approximate height and width of 3.5 mm. Notice, upon shining a light through the fiber you can see light coming through; of course a few fibers appear to have some issues. These issues include angled (non-perpendicular) cleaved ends, crushed (oval-shaped) ends, and dark blemishes from over heated (burnt) plastic ends. Since all the ends were cleaved before construction an additional cleave needs to be made to create a flush surface.

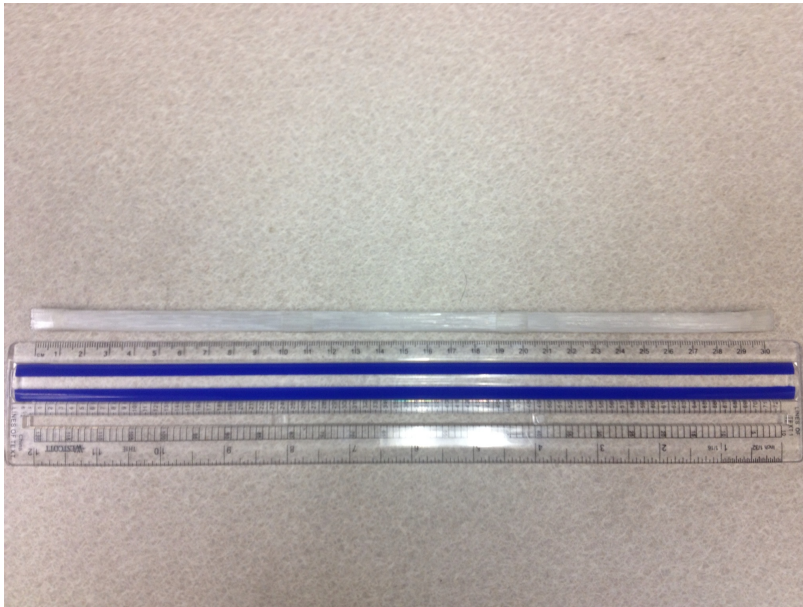


Figure 16. The “z-axis” view of the 14×14 BCF-12 fiber bundle array. The bundle measures 30 cm in length, however, the ends are to be cleaved flush, thus will be shorter after the final cleaves are performed.

In an effort to reduce the amount of light leakage into the fibers from the environment an exterior lining of black vinyl electrical tape was applied. The application of the black vinyl electrical tape is shown in Figure 17. The black electrical tape provided two desirable characteristics. First, the light leakage into the scintillator would be reduced. Second, the fiber bundle would demonstrate an increase in rigidity. The electrical tape was wound from end to the other end leaving approximately 0.5 cm of each end still exposed. The exposed ends were left untaped to perform one last hot knife cleaving to ensure the ends were flush.

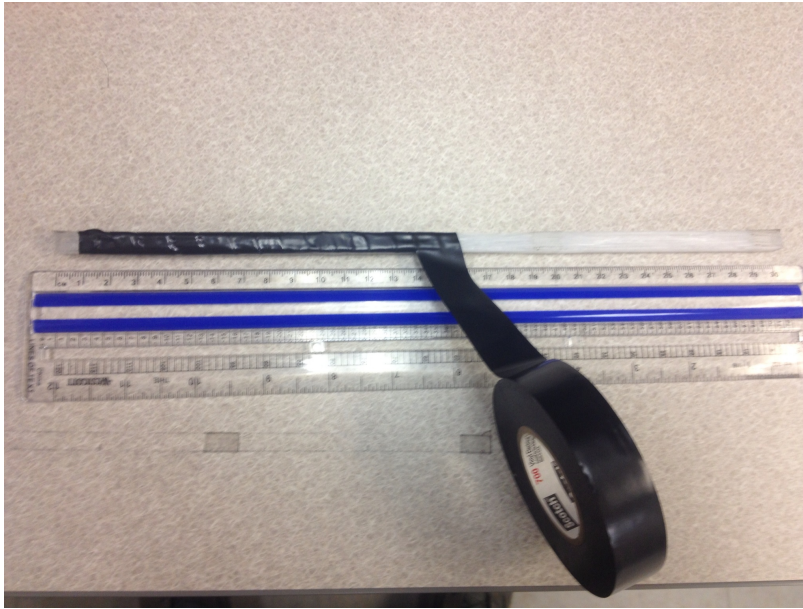


Figure 17. The “z-axis” view of the 14×14 BCF-12 fiber bundle array. The bundle is wrapped in black vinyl electrical tape to help mitigate light leakage out of the bundle. The tape was applied at a approximately a 45 deg angle and three layers were applied.

3.4 Investigation of the DPO7104 Digital Data Acquisition

The process of using the fast digital data acquisition feature of the Tektronix DPO7104 series digital oscilloscope controlled by MATLAB through the TekVISA interface is examined. As discussed in Section 2.6, there are many advantages to using the Tektronix DPO7104, a high speed digital oscilloscope for collecting large

numbers of waveform samples in a matter of a few seconds. In an effort to determine the dead time of this detection system, tests were performed to understand the amount of time it takes to acquire, write, save, and transfer the data. This information can help in determining if this data acquisition technique is fast enough for the types of experiments desired, or if potentially another technique, such as pattern triggering, will need to be utilized.

The two goals of this investigation were to determine the system dead time and understand how the number of points per waveform, number of waveforms, and number of sets of waveforms affected the system dead time. An Agilent 33220A 20MHz Function/Arbitrary Waveform Generator supplied a constant positive pulse, which resembles the shape of the expected output of the SiPMTs. The generated output pulse was set to a specific settings which can be found in Table 8. The frequency was able to range from 1 Hz to 5 MHz. The pulse labeled Arbitrary 1 is a positive pulse with exponential decay, while the pulse labeled Arbitrary 2 is just a regular positive “rounded” square pulse.

Table 8. Characteristics of two arbitrary waveforms generated for the digital oscilloscope dead time experiments. The two types of pulses were generated by the Agilent 33220A 20 MHz Function/Arbitrary Waveform Generator. Both waveforms could range in frequency from 1 Hz to 5 MHz (period of 1 sec to 200 ns).

Identifier (Arb #)	Amplitude (V_{PP})	HiLevel (V)	Offset (V_{DC})	LoLevel (mV)	Width (ns)	Edge Time (ns)
Arb 1	+2.5	2.6	+1.35	100	N/A	N/A
Arb 2	+1.475	1.475	+0.738	+0	20	5

These experiments used a simple set up. The waveform generator is connected to the digital oscilloscope via a BNC cable. The digital oscilloscope is then connected to a laptop or personal computer via an Ethernet cable, where the commands for data collection are executed through a TekVISA interface by a MATLAB script. The MATLAB script used in this investigation and throughout the rest of these experiments

was taken from Appendix D of Gearhart’s thesis [2]. Only a few slight modifications were made to adjust the input, the buffer size, and the output parameters. The final modified MATLAB script used in this research is located in Appendix B.

When the digital oscilloscope receives a signal from the waveform generator, via coaxial cables, the digital oscilloscope outputs the measured signal to the screen while saving the data points into its internal memory. It is helpful to define a few terms (e.g. run, set, waveform, and pulse) to aid in the comprehension of the entire collection process used in this research. The first data point in the displayed (i.e. saved) pulse is denoted as point A in Figure 18. The last point in the displayed (i.e. saved) pulse is denoted as point B. A waveform is comprised of the data points between points A and B. Each waveform has 1000 data points defined by the user via the MATLAB control script. In Figure 18, the numbers 1–6 label the pulses that occur within a waveform as measured by the digital oscilloscope receiving a signal from a SiPMT. The arbitrary waveforms, defined in Table 8, which are produced by the waveform generator will appear different on the digital oscilloscope than the waveform in Figure 18 since they have pulses of equal height and spacing.

Since the single building blocks of the entire data collection are the individual pulses and waveforms, it is necessary to describe the collection of multiple waveforms, which is defined as a set, as well as the collection of multiple sets, which is defined as a run (Figure 19). A single run is composed of an user defined ‘n’ number of sets, which typically ranged from 1–1000. A single set is composed of a user defined ‘m’ number of waveforms, which ranged from 1–10,000. As depicted in Figure 18, the waveform is defined by all the data points between points A and B, and composed of a varying number of pulses.

There were two collection scenarios tested using this MATLAB script to understand how a change in the number of sets collected in a single run affects the collection

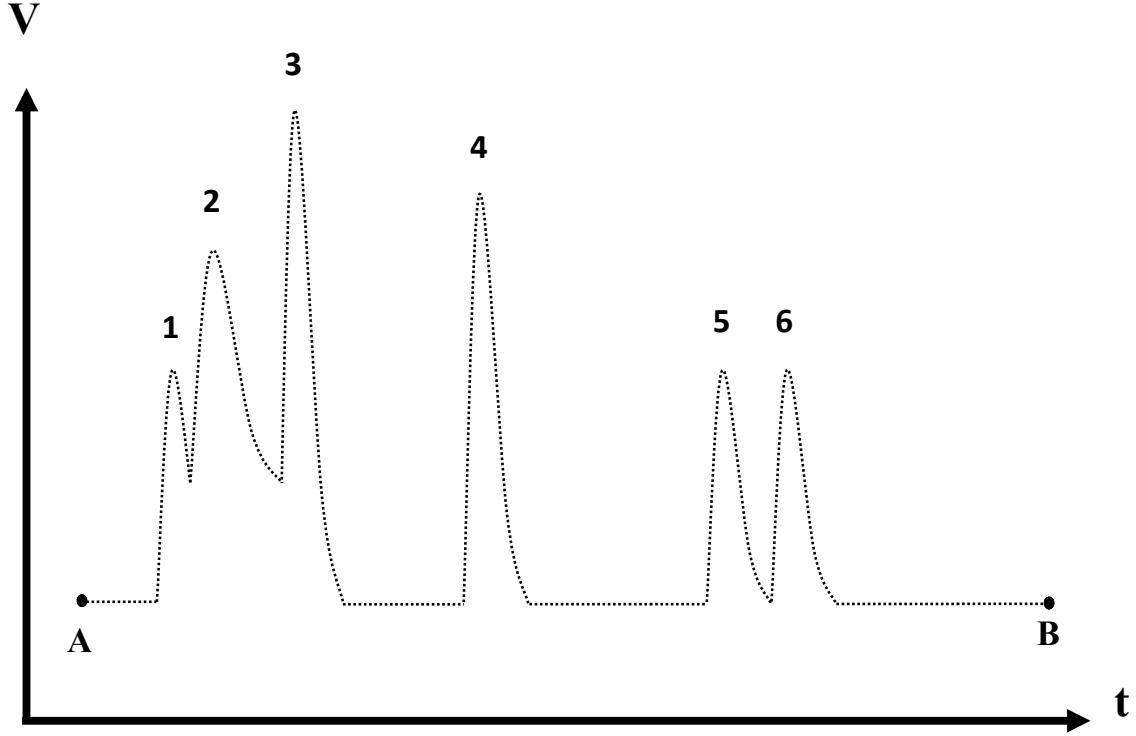


Figure 18. Illustration of a waveform measured and displayed by the Tektronix DPO7104 digital oscilloscope. The waveform depicts a typical response received by the digital oscilloscope from a SiPMT.

time and the fraction of pulses collected. The first scenario selects a high (e.g. 5 MHz) frequency signal and varies the number of data collection sets, while recording the waveforms and collection time. For example, the 5 MHz signal is sent to the digital oscilloscope and a single run of the MATLAB script is initiated after changing the number of sets (i.e. ‘n’). The time that transpires during the single collection run, as well as all the recorded waveforms during the run are saved. For each new 5 MHz signal run, the number of sets is changed to include 11 different values, which are 1, 2, 3, 5, 10, 25, 50, 100, 250, 500, and 1000. Each run holds constant the number of data points per waveform at 1000 and the number of waveforms (i.e. ‘m’) at 1000. For the second scenario the input signal is changed from 5 MHz to 1 kHz (i.e. low frequency) and the same process to gather the run collection time and waveforms for the 5 MHz signal is used. These two scenarios will determine how many pulses are

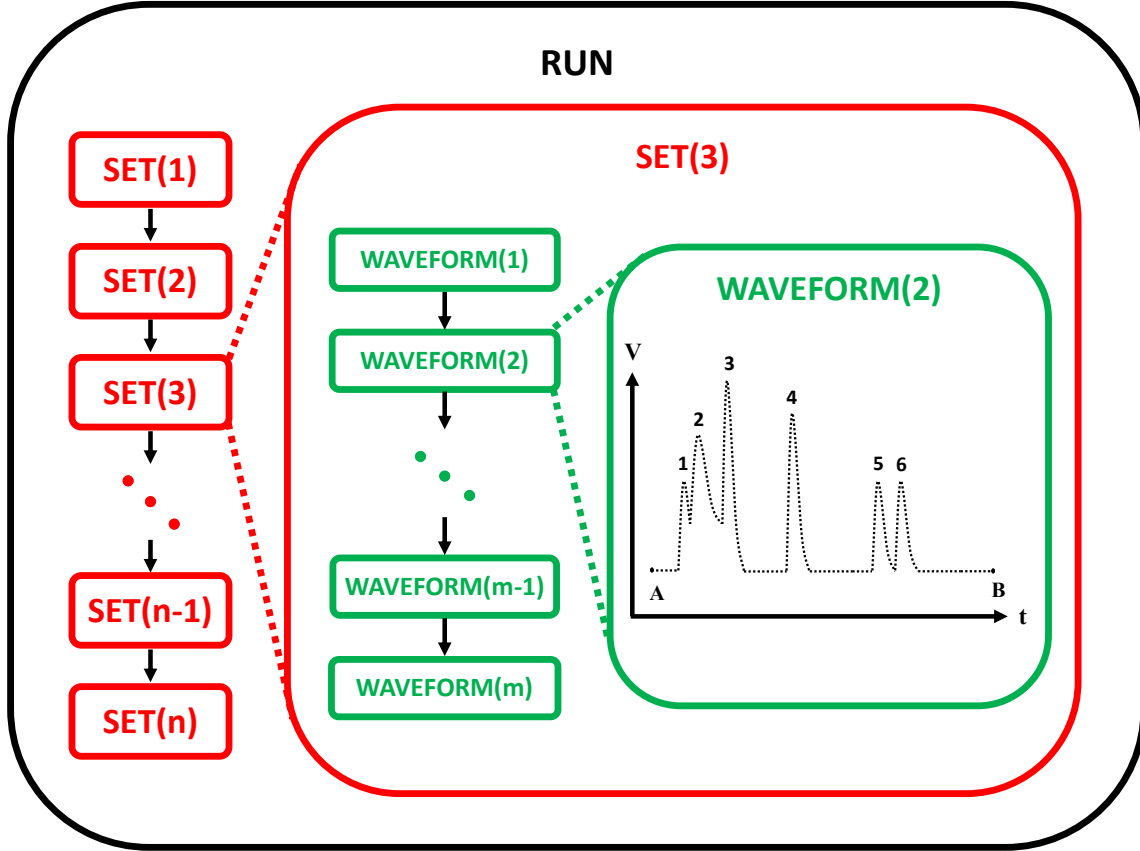


Figure 19. A diagram breaking down a single acquisition run (denoted in black). A single run is composed of set(s) (denoted in red), which is composed of waveform(s) (denoted in green). The run begins and ends with the start and stop of the MATLAB script for the SiPMT data collection.

collected compared to how many pulses theoretically should be collected to provide an approximate efficiency (referred to as “fraction” in this research) at each frequency.

After completion of the two scenarios it is necessary to conduct further investigation into the actual fraction collected out of total possible pulses during the true acquisition function of the MATLAB script. As a result another test is performed to accomplish two goals: 1) understand how the change in frequency, while holding all other parameters constant, affects the collection time; and 2) break down the entire collection process into its four main components: acquire, ask, read, and save. This test included: 1) the actual acquisition (acquire) time, 2) the memory storage (ask) time, 3) the read (read) time, and finally 4) the resizing and saving to the computer

(save) time. Each component of this process is required in order to complete any single acquisition by MATLAB from the Tektronix digital oscilloscope. The “acquire time” represents the actual time the digital oscilloscope is acquiring the input signal. The “ask time” represents the time it takes for the computer to prepare the waveform preamble and binary data to be stored into memory. The “read time” represents the time it takes the computer to read and store all the waveform data to the computer, essentially it is the computer preparing itself to receive the data stored on the digital oscilloscope. The “save time” represents the time it takes the computer to resize and re-save the waveforms as a MATLAB file within the folder containing the MATLAB script. The resize is required to have the data look exactly like the waveforms displayed on the oscilloscope screen. The MATLAB Level 5 MAT-file is composed of a 128-byte header followed by one or more data elements [18].

The entire data collection process requires a few distinct process with each requiring tens to hundreds of lines of coding. To summarize all the actions, decisions, and steps involved in a single run, a flow chart presented from a programming and coding perspective is provided in Figure 20. The flow chart is similar to Figure 19 in defining what a single run entails. This illustration, however, focuses on what tools and equipment are involved in the execution and sharing of information during the acquire, ask, read, and save processes.

The same MATLAB script from the first two scenarios was used for the additional investigation, with the addition of an internal timing function in MATLAB, which is used to determine the time elapsed during each of the four functional areas of the MATLAB script. When the MATLAB script is initiated, the first portion saves all the desired user input parameter values. The script continues by setting up the oscilloscope using the saved parameter values. An internal MATLAB timer is then started by the script to designate the beginning of the acquisition function. The oscilloscope

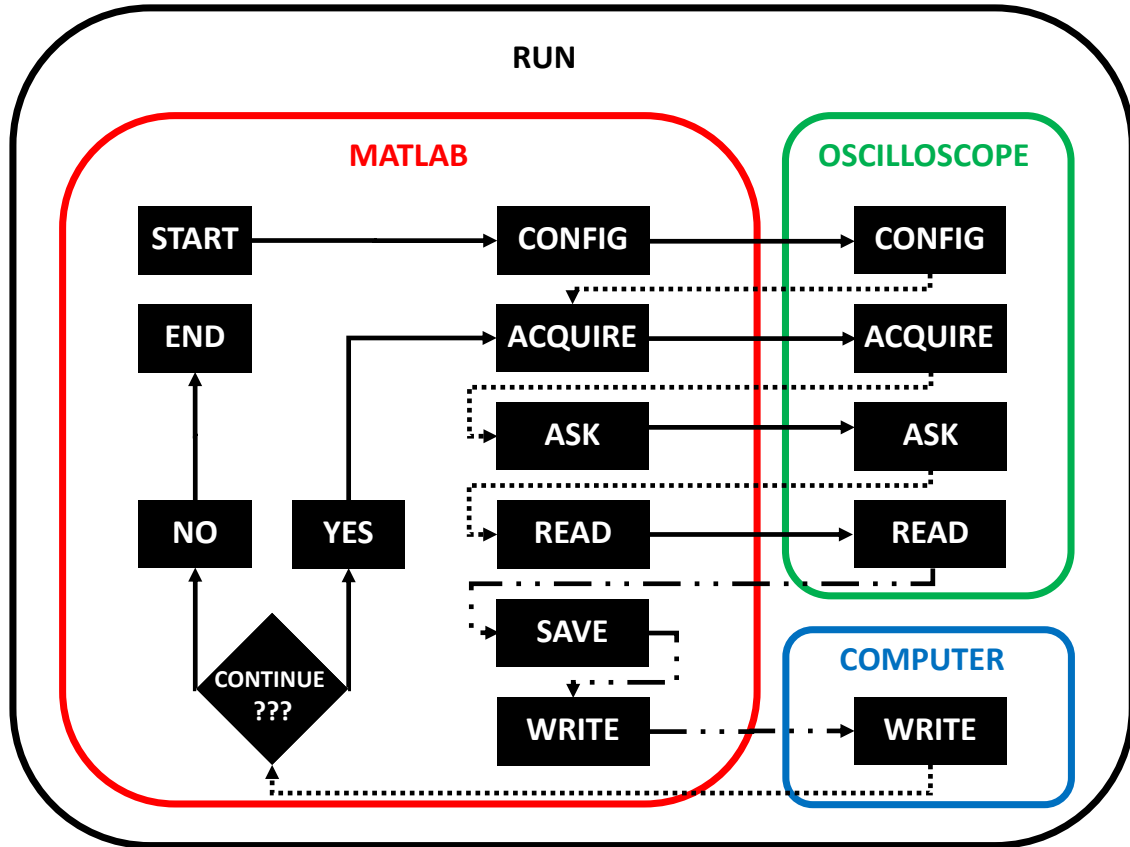


Figure 20. An illustration of a run (denoted in black) from a programming and coding perspective. A run begins when the MATLAB (denoted in red) script is user started. The script progresses through configure, acquire, ask, read, save, write, and continue. The oscilloscope (denoted in green) receives command prompts from MATLAB through TekVISA commands which include configure, acquire, ask, and read. The computer (denoted in blue) receives data from MATLAB to save the run, which is composed of many set(s) containing multiple waveform(s). Solid lines represent a command being executed. Dotted lines represent a move to the next command after the current prompt is completed, where no new command is given and no data is transferred. The half solid, half dotted line represents data being transferred, where no new command is given.

then acquires the signal, collecting until the number of waveforms (user defined 'm' amount) have been reached. A MATLAB timing signature is then requested by the script that marks the end of the acquisition function and the start of the memory storage time. During the memory storage phase, the oscilloscope stores the preamble and binary data into its own memory. Another MATLAB timing mark is then requested to designate the end of the memory storage time and the beginning of the

read time. The oscilloscope at this point reads the information and stores the number of bytes into memory for all the waveform data in channel one and/or channel two (depending on user determined setting of recording one or two channels). Another timing mark is then requested to mark the end of the read time and the beginning of the save time. The oscilloscope is now working with the LAN connected computer to save the current set of waveforms onto the computer as ‘Ch.1.mat’ or ‘Ch.2.mat’ MAT-File, depending on the user’s channel selection. The final timing mark is then requested to mark the end of the save time.

3.5 Scintillation Yield Parametric Study

Scintillation yield efficiency heavily impacts the performance and capability of a proposed time-of-flight neutron spectrometer and is discussed in this section. Specifically, a scintillation yield parametric study devised to understand the minimum neutron energy required to produce adequate photons in a BCF-12 scintillating fiber to be detectable by a photosensor is discussed. Initially, photomultiplier tubes (PMTs) were going to be used for both the single fiber and fiber bundle TOF neutron spectrometer experiments. The specifications of the fast PMTs that were used initially in this research are provided in Appendix C. Unfortunately, one of the PMTs was damaged during preliminary measurements and they were replaced with Hamamatsu’s SiPMTs. This section will also provide a comparison of various Hamamatsu SiPMTs.

For the purposes of this parametric study, the non-quenching factor ($P_{non-quench}$) in Equation 18 was assumed to be 90% (i.e. $P_{non-quench} = 0.9$), which is equivalent to saying the quenching factor is 10% (i.e. $P_{quench} = 0.1$). This loss in scintillation photons will be approximately an order of magnitude less for neutrons below 1 MeV [19], which could be the difference between the TOF neutron spectrometer system working or not working. Other assumptions include the position-of-interaction occurring at

the length bisector (i.e. axial middle) of the fiber, the photons will be isotropically emitted from the point of interaction, and half of the available remaining photons which remain trapped within the fiber will travel toward each end of the fiber. This is not to be confused with half of the photons generated by a neutron scintillation event, since only a small fraction (i.e. $\sim 6\%$) will be trapped within the fiber.

A MATLAB routine, found in Appendix D, was generated to compare the various scintillation photons which can be detected by a particular photosensor, specifically the Hamamatsu S10362-11 series. Equation 18, from Section 2.3.2 was used for estimating the scintillation yield from various scintillating fibers with different geometries and layers of cladding connected to Hamamatsu SiPMTs. The various scintillation yield parameters used in the parametric study are provided in Table 9.

Table 9. The scintillation yield parametric study yield parameters and their values. The scintillation efficiency, ϵ_{scint} , will only change as you change the type of scintillating fiber (e.g. BCF-10, 12, 20, 60, 91A, 92, 98). The trapping efficiency, ϵ_{trap} , changes as a function of fiber geometry (e.g. round versus square fibers). The non-quenching factor, $P_{non-quench}$, is assumed as 90%. The position-of-interaction, x , is fixed at 15 cm (but can be changed to user's desire) to represent the mid-point between the fiber ends (total length of fiber is 30 cm). The quantum efficiency, ϵ_{quant} , is a fixed characteristic of the SiPMT chosen. The model no. indicates whether the property describes the BCF-12 plastic scintillating fiber or the specific Hamamatsu S10362-11 series SiPMT. This table references parameters from Equation 18.

Parameter	Value	Units	Model No.
ϵ_{scint}	8	$\left(\frac{\text{photons}}{\text{keV}}\right)$	BCF-12
ϵ_{trap}	0.0344	—	BCF-12
$P_{non-quench}$	0.9	—	BCF-12
x	15	(cm)	BCF-12
λ_{eff}	270	(cm)	BCF-12
ϵ_{quant}	0.25	—	025C
	0.48	—	050C
	0.74	—	100C

3.6 Spatial and Timing Resolution Parametric Study

Ultimately the achievable spatial and timing resolution for a fiber based TOF neutron spectrometer will drive the feasibility of the approach. This section describes a method for theoretically characterizing these two key design parameters. Using the position and timing uncertainty derivations found in Section 2.5, a MATLAB script was constructed to understand the bounds of a neutron spectrometer for a predetermined spatial and time resolution. Analysis of multiple spatial and time resolution settings is performed by holding one of the parameters constant and changing the other. Holding the time resolution at a fixed value and ranging the spatial resolution, then holding the spatial resolution and ranging the time resolution provides information on how each component affects the overall theoretical energy resolution and its uncertainty, which is then analyzed.

In his research on single scintillating fibers, Takada found a spatial resolution of 16 cm for Saint-Gobain's BCF-20 fiber [5]. One goal for the entire research effort is to find spatial resolutions that improve upon this published value. The values found in Takada's experiments are first used in the MATLAB script as the initial basis for comparison. After analyses of these results a spatial resolution of 1 mm was determined. This spatial resolution value is chosen due to the resulting energy calculation from the MATLAB script having an error less than 10%. Also, the digital oscilloscope used in this experiment can sample up to 20 GHz, which can then sample points on the order of femtoseconds (fs). A crucial factor in the characterization of a neutron time-of-flight spectrometer is the timing resolution between neutron interactions within the plastic scintillating fiber. A problem can arise if a neutron traverses within the scintillator and undergoes multiple scatters within a period of time which the detection system can not distinguish. For example, a 1 MeV neutron has a velocity of 1.39×10^7 m/s. If the neutron travels 1 cm through the scintillator,

it will take ~ 720 ps, but if it were to travel 10 cm, it will take ~ 7.2 ns. This means the timing resolution of this parametric study needs to be on the order of fractions of a nanosecond to have the ability to characterize the time-of-flight between neutron scatters. For the purposes of this parametric study the timing resolution was set at 0.1 nanoseconds.

A MATLAB script, shown in Appendix E, was built containing the derivation of the spatial and timing uncertainties (see Equation 26) of a TOF neutron spectrometer to calculate the energy output, which would be determined by the spectrometer for a given position and time. An array of velocities was generated using a position divided by time. The position ranged from one centimeter to one meter, incrementing by one centimeter, and the time ranged from 0.1–10 ns, incrementing by 0.1 ns. The uncertainties in time and space were fixed to the a desired value. The position and time are then changed in controlled step sizes to observe the limits for which an energy of interest could be determined by the neutron spectrometer. For each range of position and time there will also be an associated error. From this the neutron spectrometer energy output can then be bounded for its effective operational limitations. The outputs desired would be energy, energy uncertainty, and the relative error. A position uncertainty of 1 mm and a timing uncertainty of 0.1 ns were chosen for the parametric study after performing some preliminary analysis. The preliminary analysis determined that the range of acceptable (i.e. relative error of 10% or less) spectrometer performance can only be achieved when we approach these values of spatial and timing uncertainty.

3.7 Single BCF-12 Fiber Readout Using SiPMTs

The devices selected for measuring the light output from the scintillating fibers were a set of Hamamatsu silicon photomultipliers. Initially, Hamamatsu fast PMTs

were planned for the experiment, however due to readout problems and the lack of obtaining a new PMT when one broke, other photosensors were considered. The Hamamatsu S10362-11-025C SiPMT was chosen due to its availability, size, and its previously use in research at AFIT by Jones while investigating YAG:Ce scintillating fiber properties [3].

3.7.1 SiPMT Circuit Construction.

In order to characterize the performance of the SiPMTs and his fiber system, Jones designed multiple light-tight boxes for his experiments. Two of Jones' light-tight box designs were used throughout these experiments. The first one was a custom design aluminum box with cylindrical openings for PMTs, however, this one was discontinued use after one PMT was broken and the time to secure a replacement was prohibitive. The second light-tight box was a black PelicanTM case, which proved to only reduce and not eliminate light entering the inside of the case where the SiPMTs were housed. After a few initial tests of the background counts, it was determined that these light-tight boxes were insufficient because too much light was leaking in causing the photosensors to saturate [3]. A new light-tight box was required. An aluminum box measuring 19 cm long, by 11 cm wide, by 6 cm high with a six-screw removable lid was chosen. The aluminum light-tight box was drilled and fitted with four BNC connectors, two on each short end of the box. This would provide two bias voltage supplies and two output signal connections for each SiPMT photosensor. Each side was labeled with HV (i.e. high voltage) and SIG (i.e. signal) for side A and side B so as to not confuse the connection ports. A depiction of the outside of the aluminum light-tight box is provided in Figure 21. The outside edges where the screws secured the the lid to the box where layered in black electrical tape to reduce light leakage into the box.



Figure 21. The light-tight aluminum box used for SiPMT experimentation. The box measures $19 \times 11 \times 6$ cm and is labeled A and B for the dual ended SiPMT experimentation. Black vinyl electrical tape was used to cover the edges of the lid-box interface to reduce the amount of light leakage into the aluminum box.

The two SiPMTs and the circuit boards were affixed to aluminum jigs which securely held the SiPMTs to be in constant contact with the single BCF-12 fiber. The Hamamatsu SiPMTs used in these experiments are shown in Figure 22. The SiPMT circuits originally used were from Jones' thesis research which resembled a circuit schematic shown previously in Figure 10. However, after much testing using Jones' circuit and receiving no usable signal, a new circuit was built. Three potential readout circuits were considered for this research. The first two circuits suggested by Jones and Hamamatsu respectively, did not produce signals when connected to the power supply. The circuit suggested by Hamamatsu is shown in Figure 23. After troubleshooting both circuits, a new circuit was constructed based upon its similar

use in SiPMT-based time-of-flight positron emission tomography (TOF-PET). The circuit design is shown in Figure 24. It is believed that this new circuit works better because the signal received by the oscilloscope from the circuit is consistent with Geiger-mode SiPMT outputs from the technical manual for Hamamatsu SiPMTs.



Figure 22. The Hamamatsu S10362-11-025C SiPMT. Note the effective active area is 1×1 mm and is depicted by the darker small square within the larger silver square. The SiPMT picture was obtained from the silicon photomultiplier technical brochure and reproduced with permission from Hamamatsu [15].

The completed circuit boards were inserted into the aluminum jigs, which were secured inside the aluminum box with a threaded rod. The threaded rod went through each aluminum jig and was secured on each short end of the aluminum box with washers. The aluminum jigs could be adjusted closer or further apart from one another by moving the washers on the threaded rod. Adjustment of these aluminum jigs is needed to easily secure different sizes of scintillating fiber for multiple length TOF experiments. This setup is shown in Figure 25. The SiPMT circuits were securely held to the aluminum jigs using nylon screws and washers. Nylon screws and washers were used to prevent any shorting of the circuit through the screw contact points into the aluminum jig. The circuit boards were all grounded to the aluminum box by means of a wire connecting the circuit board to one of the BNC connector

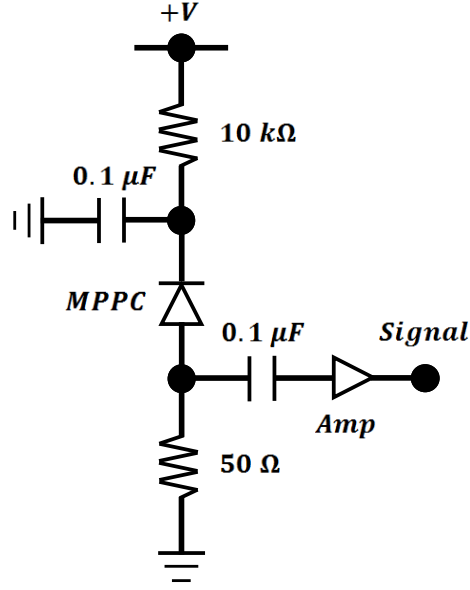


Figure 23. Basic connection diagram suggested by Hamamatsu for their SiPMTs. RG-223/U and RG-58C/U were used to wire the diagram to correctly match the impedance of the circuit. The RG-223/U coaxial cable was used for both the output signal and power and were connected to the box via a BNC connection. The connections inside the box were provided by a female-female BNC union. Four of these unions (two for power and two for signal output) were placed at the ends of the aluminum box. The Hamamatsu suggested SiPMT circuit diagram was obtained from their silicon photomultiplier technical brochure and reproduced with permission from Hamamatsu [15].

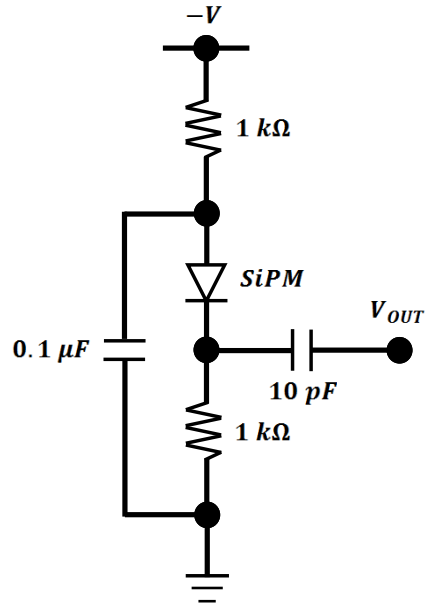


Figure 24. Basic connection diagram used for SiPMT-based TOF-PET detector. The circuit is reproduced with permission from Ronzhin et. al. [4].

ground points. A view of the front and back of the SiPMT circuit secured in the aluminum jig is provided in Figure 26 and 27, respectively. Plastic washers were also used in the securing of the aluminum jigs to the threaded rod to again reduce potential shorting of the circuits. Since, the circuit boards had wires protruding through the board, they were filed down and layered with black electrical tape to minimize shorting of the circuit to the aluminum jig.

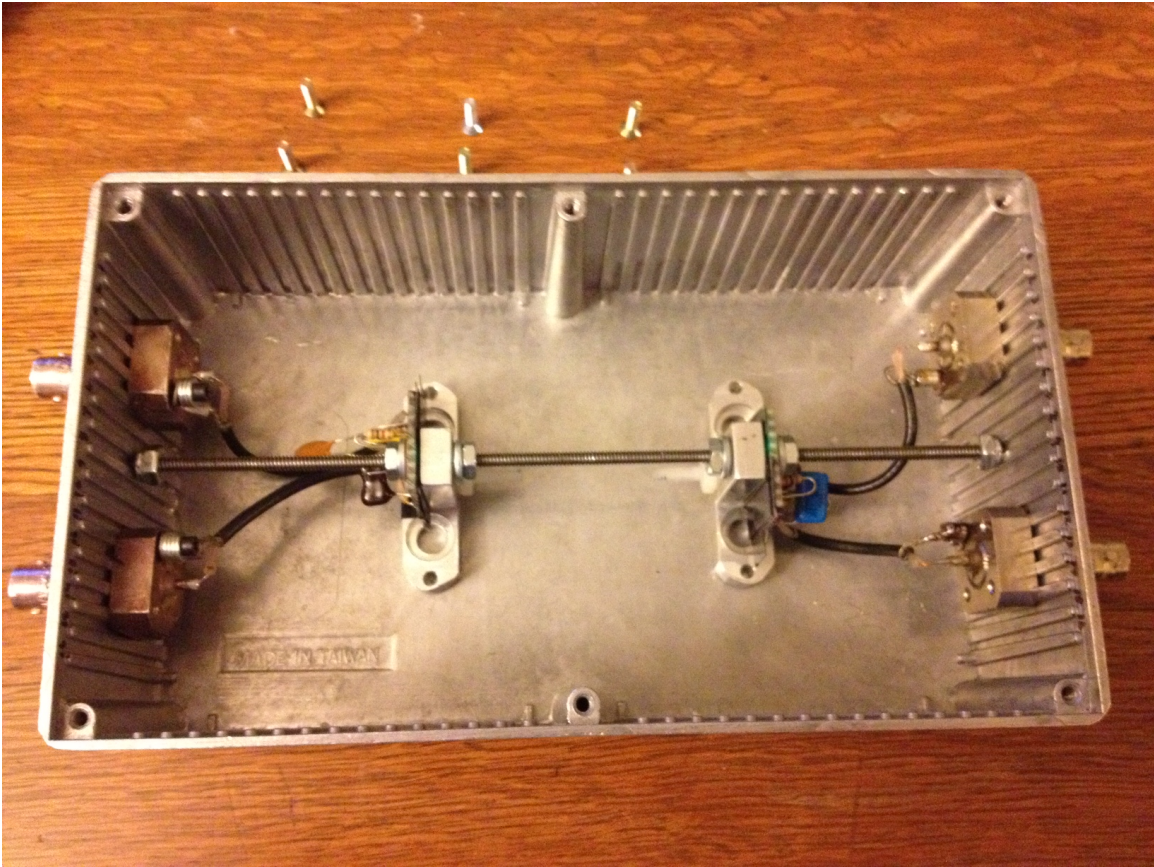


Figure 25. The light-tight aluminum box internal view. Each SiPMT is held securely in each aluminum jig with nylon washers and screws. The threaded rod extends length-wise across the entire inside of the aluminum box with both jigs secured with washers. Each SiPMT circuit connects to two female-female BNC ports via RG-223/U 50 ohm; one for bias voltage supply (-70.15 ± 0.03 V), and one for signal output to the preamplifier. The signal was to the tektronix DPO7104 digital oscilloscope with a T-connector and terminated with a 50 ohm terminator.

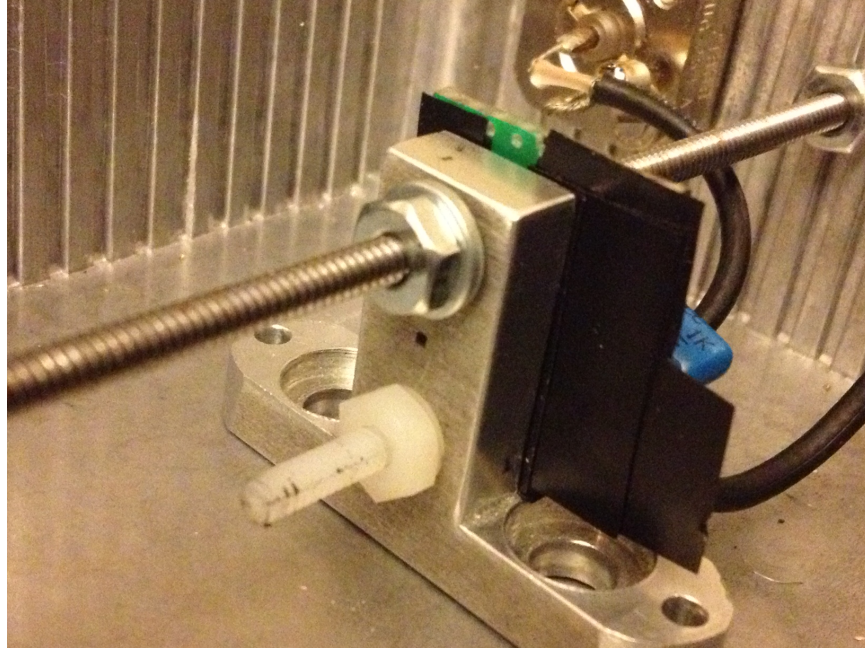


Figure 26. The front-side view of the SiPMT circuit attached to the aluminum jig inside the aluminum light-tight box. The small black box hole in the aluminum jig located between the threaded rod and nylon screw is the hole where the single BCF-12 scintillating fiber would be placed to contact the SiPMT. The hole is slightly larger than $500\text{ }\mu\text{m}$ (0.5 mm).

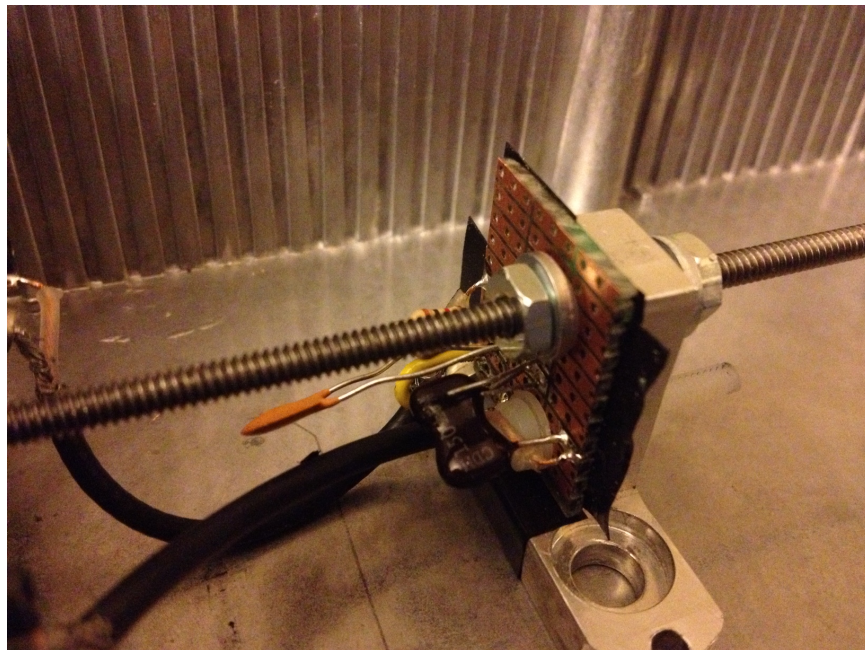


Figure 27. The back-side view of the SiPMT circuit attached to the aluminum jig inside the aluminum light-tight box.

3.7.2 SiPMT Dark Count Verification.

After finding a suitable circuit for the Hamamatsu SiPMTs it was necessary to determine the noise or background of the detection system. The background was then compared to published specification that Hamamatsu has provided to determine if there are any problems with the photosensors or if there is light leakage into the light-tight aluminum box.

The system setup for determining the SiPMT dark count is shown in Figure 11. The SiPMTs were provided a bias voltage of -70.15 ± 0.03 V. The signal output was connected via RG-58C/U coaxial cables to charge sensitive preamplifiers which sent the signal into the Tektronix DPO7104 digital oscilloscope. The oscilloscope was controlled by a MATLAB script through a LAN cable from a laptop. The data collected was post-processed using another MATLAB script. The waveforms being post-processed would contain pulses from the the SiPMTs where no source and no plastic scintillating fiber were present. Hamamatsu provides measured dark count rates for each SiPMT they produce, which was 323,000 and 318,000 counts per second for the two used in this research.

Post-processing was required after the data collection for the pulse height distribution of the dark counts to be determined and compared with the dark count provided by Hamamatsu. A MATLAB script, located in was built to load all the waveforms and find all pulses contained within each waveform and is found in Appendix F. The script uses a point by point inspection of the values, when the values in a sequence change from increasing to decreasing (or vice versa) the max or min is saved. With each waveform containing tens to hundreds of small minima and maxima, a post-processing filter to pull out the pulses of a single SiPMT firing was incorporated. This means that a true SiPMT pulse was recorded when the difference in the local minimum and maximum were greater than 100 mV. This means the pulses were not

counted unless the min to max difference was greater than 100 mV. For count rates below saturation, the number of pulses from the SiPMT are directly proportional to the amount of light created in the scintillator, which is proportional to the energy deposited by an incident neutron. This means that the pulses cannot just be counted, but in fact must be weighted.

The information provided by these background tests of the SiPMT can then help determine the background noise levels of the entire detection system. These results can also identify problems such as shorting across the circuit boards, improper grounding, or more likely problems with light leakage into the aluminum box.

IV. Results & Analysis

Analysis of the parametric studies and experiments performed are presented with some emphasis on a comparison of the results obtained from my experimentation to those obtained by previous research. Parametric studies focused on the uncertainties produced by timing and spatial resolution are discussed and included to determine the limitations and capabilities of using scintillating fibers in combination with a digital oscilloscope for neutron detection. Experiments to determine the requirements for fast digital data acquisition as a means to read and write the data for post-processing methods to be performed on the collected data are also presented. The sections will contain Geant4 single and bundle models, oscilloscope timing findings, scintillation yield expectations, spatial and timing resolution findings, and silicon photomultiplier multi-pixel photon counting findings.

4.1 Geant4 Modeling

The Geant4 modeling results described in this section provide insight into the limitations and design parameters required for a scintillating fiber-type neutron spectrometer. Results of the all the Geant4 models are presented, including a single BCF-12 plastic scintillating fiber modeled with an internal isotropic optical photon source, a fan beam neutron point source, and a 14×14 multi-fiber bundle. Analysis will consist mostly of distributions, comparisons, and interesting features of the data collected by Geant4 models.

4.1.1 Single BCF-12 Fiber.

The single BCF-12 fiber model created in Geant4 for the optical photon source and neutron source provided helpful information into the scintillation yield and neutron

scattering characteristics and is discussed in this section. The main goal of these two single BCF-12 fiber models was to validate the trapping efficiency of the plastic scintillating fiber to be compared with Saint-Gobain's published values.

Using the procedure as outlined in Section 3.1.1, the Geant4 simulations indicate a trapping efficiency of 6.5% for both 1×10^5 and 1×10^6 optical photons. A depiction of the optical photon generation and transport through the fiber is provided in Figure 28.

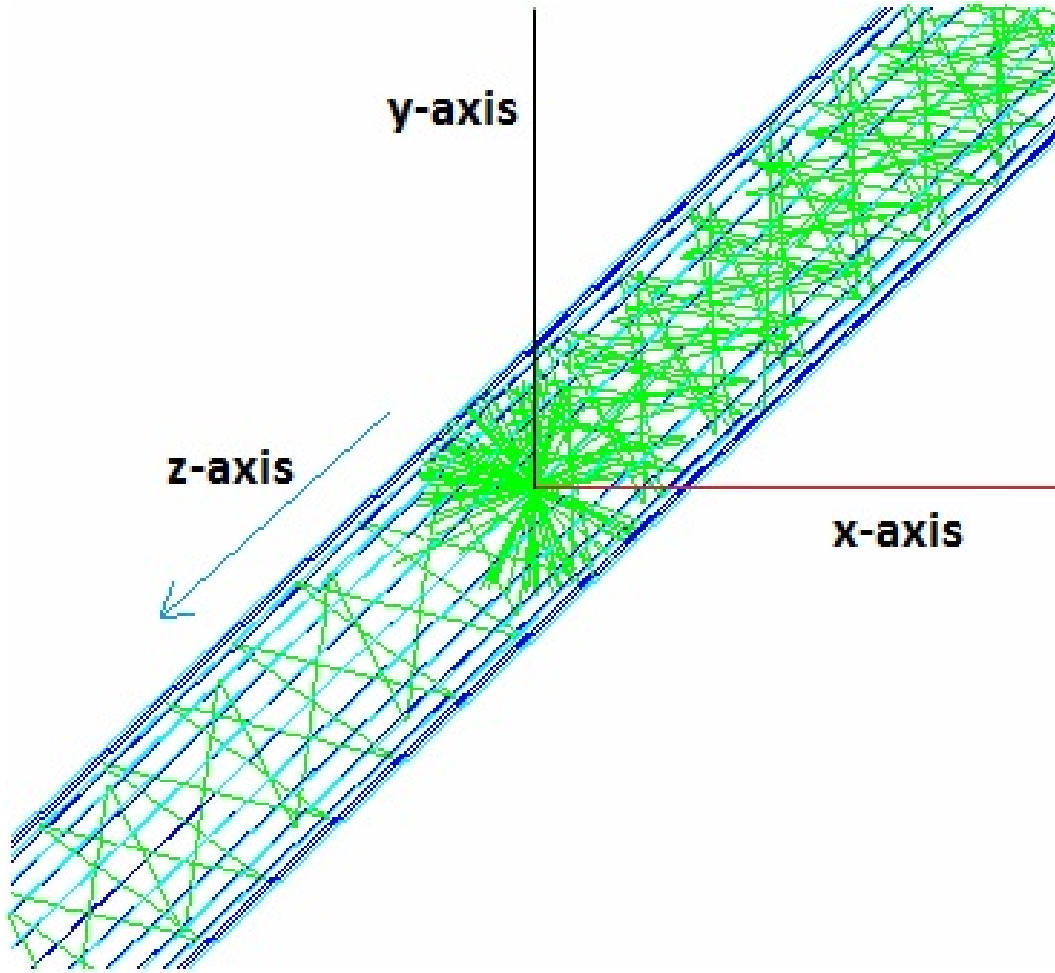


Figure 28. A view of the single BCF-12 fiber created in Geant4. The optical photon source is located at the intersection of the x and y-axis. The green vectors are traces of the optical photon trajectories within the fiber. While difficult to see, the light blue lines depict the outer cladding boundary, and the dark blue lines depict the outer core boundary. Note only the traces of the completely trapped optical photons are shown, and that for illustrative purposes this depicts an optical photon source of 100 generated photons.

For BCF-12, Saint-Gobain claims a trapping efficiency of 3.44% for their round fibers, but the model indicates an efficiency of almost double this value. By using the geometry and material properties of the fiber itself, assuming an isotropic optical photon point source at the center of the fiber, the trapping efficiency of the fiber can be calculated, beginning with

$$\sin(\phi_C) = \frac{r_F}{r_S}, \quad (28)$$

where, ϕ_C is the critical cone angle, r_F is the radius of the plastic scintillating fiber, and r_S is the radius of the isotropic point source. These values are needed to determine how much of the isotropic point source is subtended by the plastic scintillating fiber, which is constrained by the critical cone angle and radius of the fiber. The critical cone angle is a purely material property, based on the difference in the refractive indices of the core and cladding [10]. Solving for r_S with $r_F = 0.25$ mm and $\phi_C = 21.4$ deg gives the following

$$r_S = \frac{r_F}{\sin(\phi_C)} = \frac{0.25 \text{ [mm]}}{\sin\left(21.4 \text{ [deg]} \cdot \frac{\pi \text{ [rad]}}{180 \text{ [deg]}}\right)} = 0.685 \text{ mm}. \quad (29)$$

The solid angle defines how much the plastic scintillating fiber subtends the isotropic point source (i.e. scintillation photons created from a neutron interacting with the scintillator). The solid angle in this case is approximated by the relationship between the surface area within the scintillating fiber which traps the source photons (i.e. 2 circles) and the entire surface area of the source photons (i.e. a sphere). There is some approximation when using the two circles as the surface areas overlaying the spherical surface area due to the fact a sphere is continuously curved while the two circles are tangential and flat to the sphere's surface. A depiction of the photons subtended by the plastic scintillating fiber from an isotropic point source is given in

Figure 29. The solid angle, Ω , is given by

$$\Omega = \frac{2 \cdot SA_F}{SA_S} = \frac{2(\pi r_F^2)}{(4\pi r_S^2)} = \frac{r_F^2}{2 \cdot r_S^2}, \quad (30)$$

where, SA_F is the surface area of the plastic scintillating fiber, and SA_S is the surface area of the isotropic point source within the fiber. Solving for Ω after some manipulation and cancellations with $r_F = 0.25$ mm and $r_S = 0.685$ mm gives

$$\Omega = \frac{2(\pi r_F^2)}{(4\pi r_S^2)} = \frac{r_F^2}{2 \cdot r_S^2} = \frac{(0.25 \text{ [mm]})^2}{2(0.685 \text{ [mm]})^2} = 0.0666. \quad (31)$$

The solid angle subtended by the ends of the fiber from a point source at the center of the fiber is approximately 0.0666, or represented as $\sim 6.7\%$. This is based on the assumption that all scintillation photons generated at the source which have an initial trajectory angle between 0 to $\phi_C = 21.4$ deg, with respect to the fiber axis, will undergo total internal reflection.

The simulation does not account for potential defects in the material, which include air gaps (e.g. oxygen) in the molecular structure of the core as well as other defects that exist in a real fiber. Another potential cause for the discrepancy was the assignment of an initial polarization vector for each generated optical photon, a parameter required by the simulation software. To accommodate this, the photons were randomly assigned initial polarizations, uniformly distributed over all possible values. Closer inspection of how the polarization vector operates in Geant4 could potentially lead to a more appropriate distribution. The polarization vector could cause a discrepancy if the assigned vector value biases optical photons to fall within or outside of critical angle of total internal reflection. This polarization value is also the reason why there are more optical photon traces in the negative z-axial direction than the positive z-axial direction, which can be observed in Figure 28.

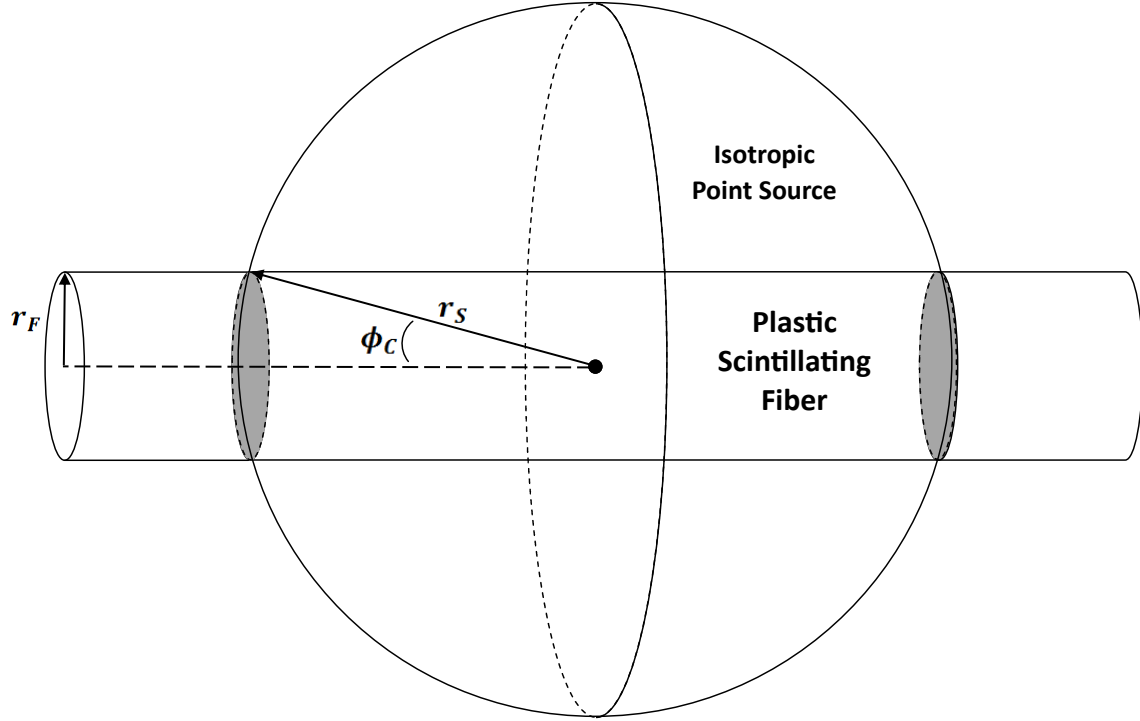


Figure 29. A depiction of the solid angle, Ω , of the point source scintillating photons subtended by the plastic scintillating fiber. The gray shaded region indicates where the plastic scintillating fiber surface and source surface area overlap, which is constrained by the critical cone angle, ϕ_C , radius of the isotropic point source ‘sphere,’ r_S , and the radius of the plastic scintillating fiber, r_F . Note the lengths, radii, and angles are not drawn to scale for illustrative purposes.

4.1.2 14×14 BCF-12 Fiber Array.

The results of the 14×14 BCF-12 plastic scintillating fiber array model built in Geant4 are explained in this section. The bundle was exposed to the same external neutron point source as described in Section 3.1.2, and the fiber bundle was exposed to 1×10^8 generated neutrons. The main purpose of this simulation was to determine the fraction of double (and greater) scattering events, distance between neutron scatters, and the velocity distribution of the neutrons.

As mentioned earlier, a time-of-flight neutron spectrometer requires at least two scatters within the scintillator to back-calculate the energy of the incident neutron. When a neutron elastically scatters it can potentially deposit energy ranging from

near zero to all of its energy. The distance traveled by a neutron in a material before scattering is directly related to its kinetic energy. If the neutron undergoes a second scattering event within the scintillating fiber, the distance and angle of scatter from the first to second event can help us infer the energy of the incident neutron. Multiple neutron scatters provide increased statistical confidence in the energy calculations of incident neutrons scattering within the detector volume. Table 10 shows the distribution of single up through four scattering events for a simulation that generated 1×10^8 neutrons.

Table 10. Distribution of scattering events for the 14×14 BCF-12 fiber array Geant4 simulation exposed to 1×10^8 neutrons.

No. Scatters	Counts	Predicted Intrinsic Efficiency
Single	5436581	5.437%
Double	358907	0.359%
Triple	27583	0.028%
Quad	2541	0.003%

This data can provide valuable information in designing an actual experiment where a 14×14 BCF-12 scintillating fiber bundle is subjected to a neutron source. For example, if exposing a real 14×14 BCF-12 fiber bundle to a D-D neutron generator, the solid angle could be calculated from the neutron source to the cross-sectional surface subtended by the bundle. According to Table 10, if 1×10^4 double scatter events are desired, then ~ 2.8 million neutrons are required to be subtended by the bundle. With a known neutron flux and source location, a user can use these results to predict the measurement time required to collect a specified number of scintillation events within the fiber bundle.

The distribution of the number of counts for each scatter distance from 1st to 2nd scatter, 2nd to 3rd scatter, and 3rd to 4th scatter are provided in Figure 30. This plot demonstrates the most probable distance a neutron travels between scat-

ters. In general, as the neutron loses energy the distance traveled between scatter events decreases, however, the distribution remains highly peaked at low distances due to the small cross sectional area presented by the fiber bundle. The distances separating most scatter events are relatively small, as the neutrons scatter once and leave the fiber bundle. One simple solution to increasing the scattering efficiency would be to increase the fiber bundle size. More scintillating material would increase the probability of neutrons scattering more than once within the bundle. However, if compactness is desired, taking advantage of geometry can help increase scattering efficiency. If the fiber bundle is subjected to a radiation source in its axial direction instead of perpendicular to the axis, then more fiber material is in the path of the neutrons. Since neutrons are more likely to scatter forward, they are more likely to travel down the fiber bundle axis, thus increasing the scattering probability without increasing the size of the fiber bundle itself.

For each neutron scatter event of 1st to 2nd scatter, 2nd to 3rd scatter, and 3rd to 4th scatter the remaining energy of the neutron from the beginning to the end of the scatter was plotted against the distance traveled, shown in Figure 31. In general the distance traveled and energy both reduce with each subsequent scatter. In Figure 31, the neutron energy represents the amount of energy possessed by the neutron immediately following the starting scatter point number. Also, the distance represents the length traveled by the neutron from the starting scatter point number to the final scatter point number. There is a degree of uncertainty in these plots, which is not immediately evident. The x and y locations provided by the Geant4 model output deck provide only the fiber array location numbers. The fibers are 0.5 mm in diameter and the scattering event could have happened anywhere within the 0.25 mm radius, thus the x and y positioning produce an associated positional uncertainty equal to the fiber radius (i.e. ± 0.25 mm). Figure 31, does not include

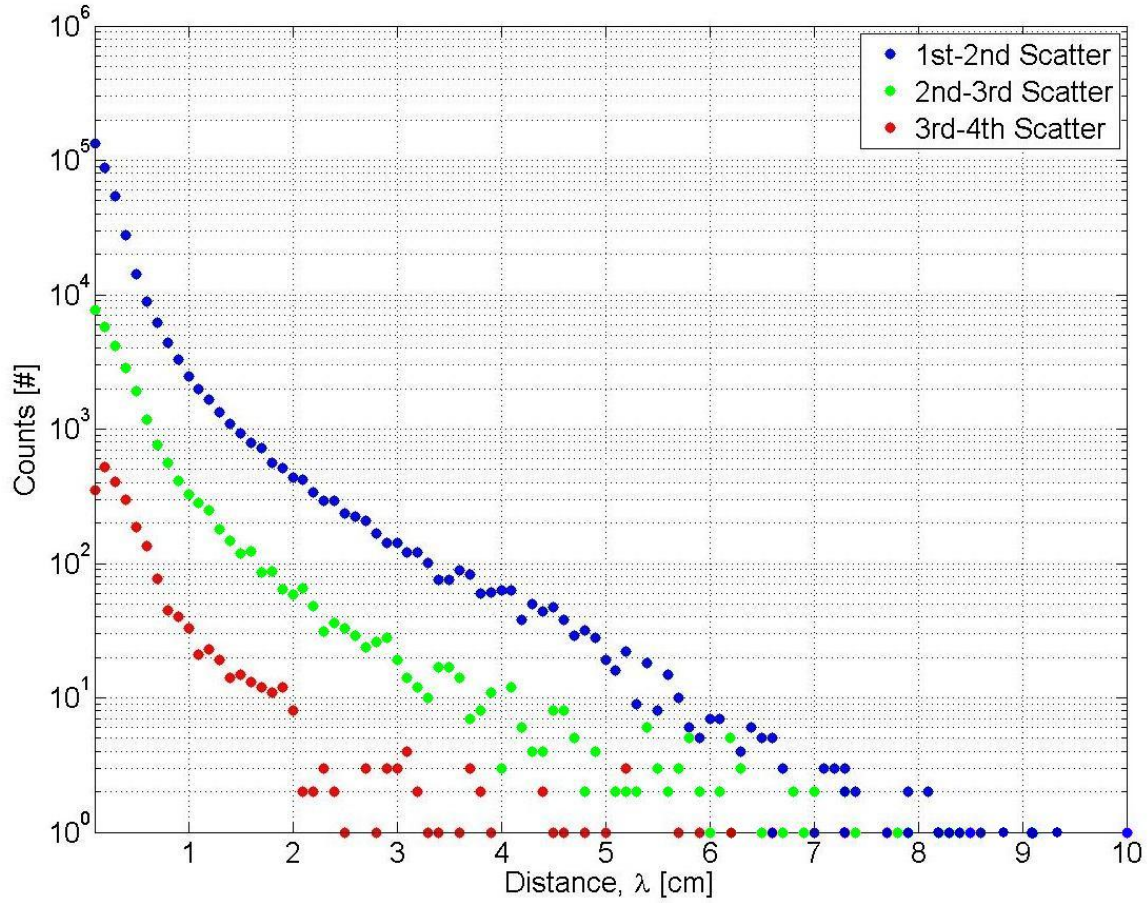


Figure 30. Distribution of counts for distance traveled between 1st to 2nd, 2nd to 3rd, and 3rd to 4th neutron scatter events in the 14×14 BCF-12 fiber bundle. The 1st to 2nd neutron scatter is denoted in blue. The 2nd to 3rd neutron scatter is denoted in green. The 3rd to 4th scatter is denoted in red. The fiber bundle was subjected to 1×10^8 neutrons.

this error in its MATLAB script energy calculations. The position was approximated in the MATLAB post-processing script using the center of the fiber as the location of the scintillation event, which is denoted in the output deck by the x and y location of the fiber in the array. An output deck lists the fiber location in the third column using four digits (i.e. yyxx). For example, a fiber location of ‘0311’ represents the third fiber from the bottom of the bundle in the positive y-direction, and the eleventh fiber from the source side of the bundle in the x-direction. This would equate to a y-coordinate of 1.25 ± 0.25 mm and a x-coordinate of 5.25 ± 0.25 mm, where the

calculation is given by the following

$$\text{Fiber Location } (x, y) = (\{(xx - 1/2) \cdot 0.5 \text{ mm}\}, \{(yy - 1/2) \cdot 0.5 \text{ mm}\}), \quad (32)$$

where, xx is the first two digits in the fiber location output deck pertaining to the x-axis fiber number, and yy is the last two digits in the fiber location output deck pertaining to the y-axis fiber number. Not shown in the calculation, but needed with each x and y fiber location is an error of ± 0.25 mm.

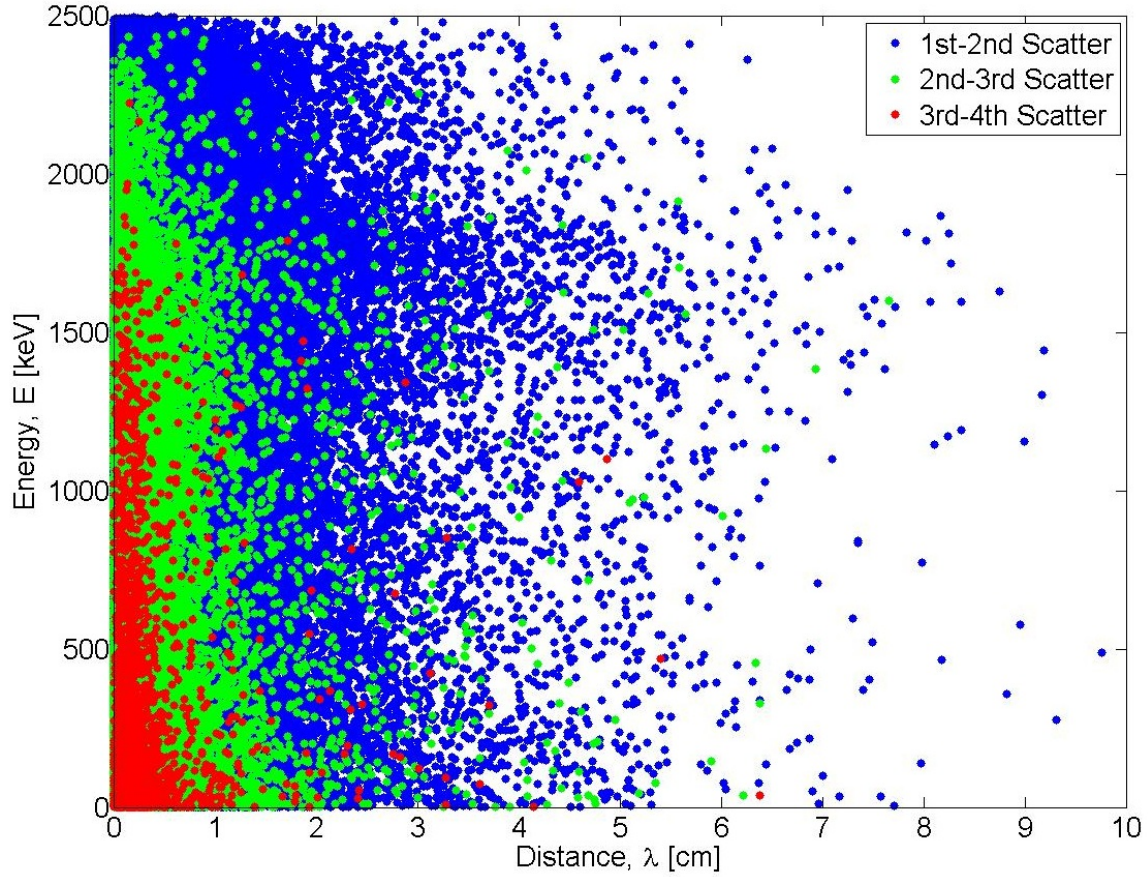


Figure 31. All 1st to 2nd, 2nd to 3rd, and 3rd to 4th neutron scatter event energies and respective distance traveled. The 1st to 2nd neutron scatters are denoted in blue. The 2nd to 3rd neutron scatters are denoted in green. The 3rd to 4th neutron scatters are denoted in red.

The three different scatter plots in Figure 31 are combined to provide a map of how many neutrons traveled a specific distance (dx) at a specific energy (dE). The combined dx and dE map is presented in Figure 32. One of the most unusual characteristics is the double peaks centered around 2 and 2.5 MeV at a scatter distance of approximately 10 mm. I am unsure as to what is causing these two energy peaks to occur so often. It could be one of two problems with either 1) the model or 2) the post-processing calculations. The model only takes into account elastic scattering of neutrons within the scintillating fiber, which could cause preferential energy scattering while neglecting inelastic scattering. Some ways of testing this phenomena include changing the fiber array size and the energy of the incident neutrons to see if the behavior persists or changes. If the source neutron energy is changed and the peaks shift to lower energies where the double peak behavior didn't exist originally, then the issue is most likely an improper request of information by the user or the physics that is applied. If the results persist after changing the size of the fibers or the bundle size, then the geometry of the model is the problem. The next unusual characteristic is the constant number of scatters at 10 mm for all energies ranging from 0.1–1.75 MeV. This demonstrates a constant probability of scattering at 10 mm where energy dependence is non-existent below 1.75 MeV. Again, I am not sure why this constant appears throughout the model. This could be a result of the overall mean free path of neutrons at energies between a few electron-volts to 2.5 MeV is greater than 10 mm, meaning that scattering out of the bundle is more likely than continued scatters within the bundle. The final unusual characteristic can be seen as an inverse distance squared relationship at 2 and 2.5 MeV starting at 10 mm and falling out to 50 mm. It is difficult to see, but there is a slight region that ranges from a distance of 1–3 mm and neutron energy of 0.1 to 2 MeV, which has approximately half as many counts as the 10 mm constant count region.

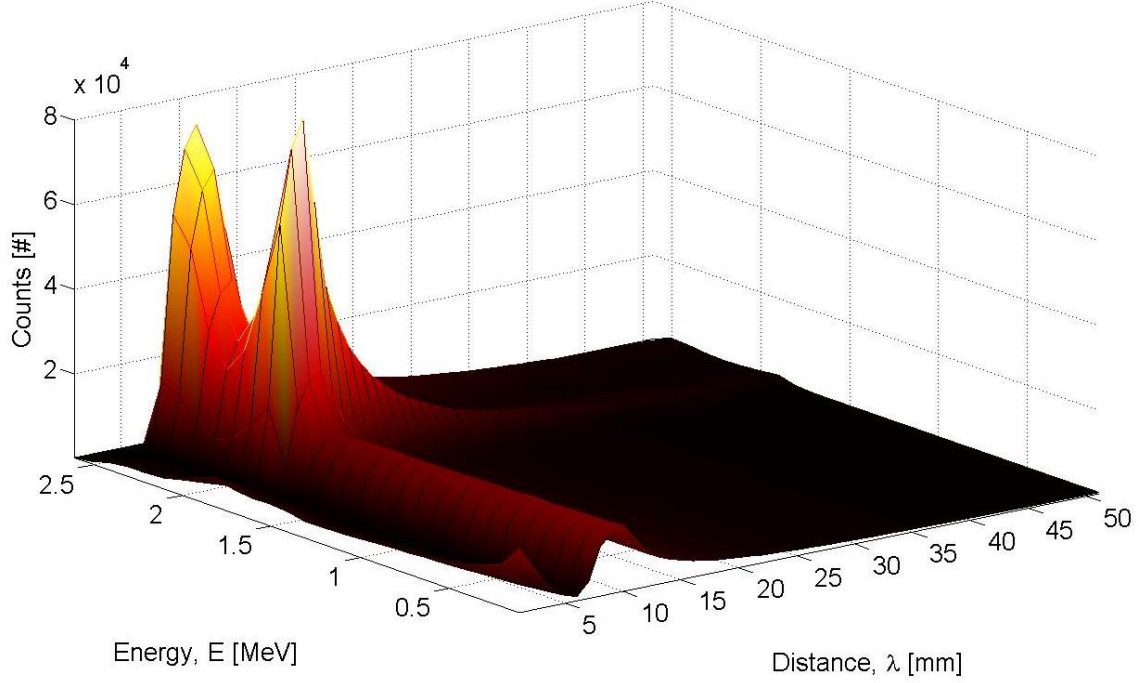


Figure 32. The overall scattering energy and distance traveled distribution for all scattering events combined. Each energy bin represents a dE of 100 keV and each distance bin represents a dx of 1 mm.

Another approach to understanding and verifying the results of the output file generated by the Geant4 simulation was to compare the neutron energy stored in the Geant4 simulation to the calculated energy based on the distance between neutron scatters and the time it took to traverse that distance. The simulation starts the neutron at 2.5 MeV and deposits a certain fraction of energy with each scatter. The velocity of that neutron can be calculated directly by finding the distance between scatters and dividing it by the transit time. Thus, assuming a non-relativistic velocity, the energy of the neutron can be calculated using the classical form for kinetic energy,

$$E = \frac{1}{2} mv^2, \quad (33)$$

where, E represents the kinetic energy of the neutron, m represents the mass of the neutron, and v represents the velocity of the neutron. The comparison was then

made by plotting the Geant4 simulation neutron energy on the x-axis and plotting the calculated neutron energy on the y-axis. The plots of these comparisons for 1st to 2nd, 2nd to 3rd, and 3rd to 4th neutron scatter events are given in Figure 33.

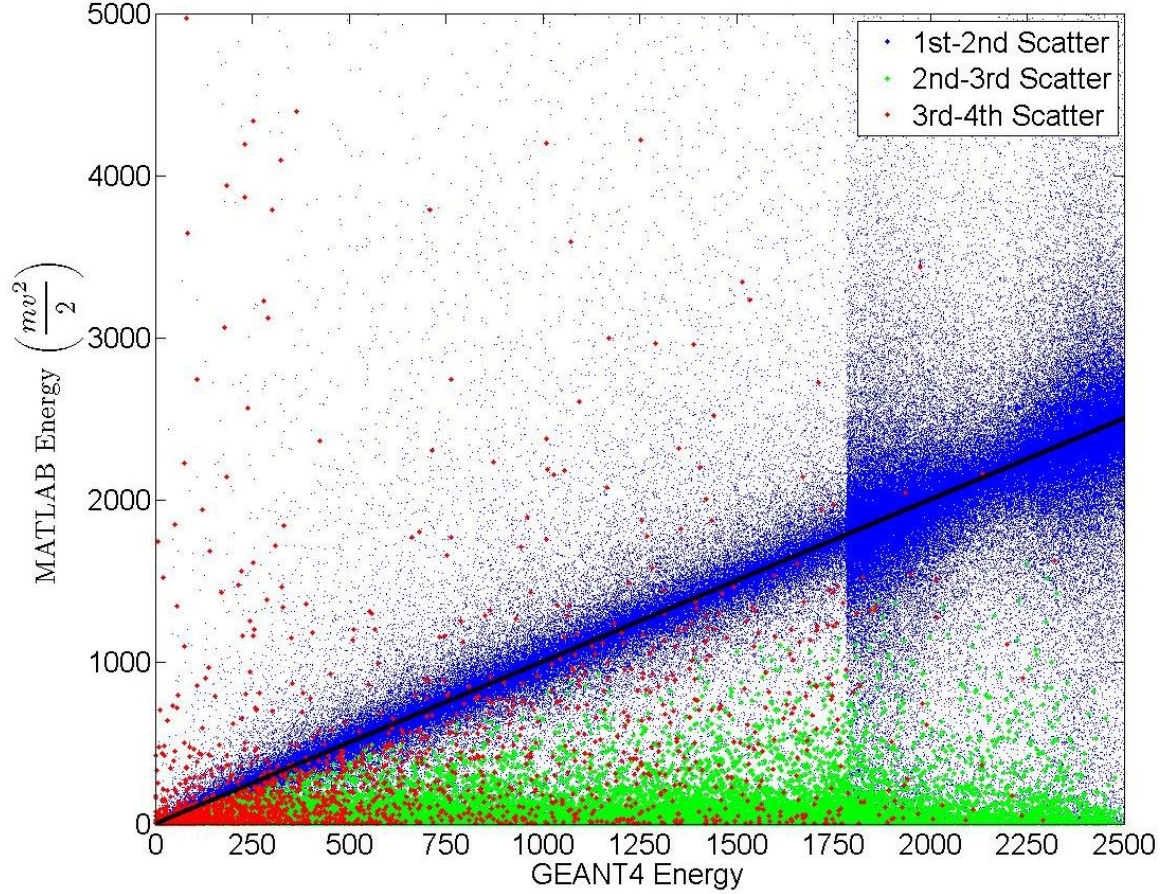


Figure 33. Comparison of the Geant4 and MATLAB calculated neutron energies for 1st to 2nd, 2nd to 3rd, and 3rd to 4th neutron scatter events. The majority of 1st to 2nd neutron scatter points follow the $\text{Geant4} = \text{Energy} \left(\frac{1}{2}mv^2 \right)$ line, denoted in black. Note: the data marker size for 2nd to 3rd and 3rd to 4th neutron scatter events is larger than the 1st to 2nd neutron scatter events to increase visibility on the plot.

In all cases the energy should not exceed 2.5 MeV since only down-scattering of neutrons occurs. In all the plots the Geant4 simulation neutron energy (i.e. x-axis) never exceeds the 2500 keV boundary. However, the calculated neutron energy, based on v^2 , varied greatly for all scattering situations. To aid in a quick recognition of the expected equality of data a black line is provided in Figure 33. The black line

represents $x = y$ (i.e. Geant4 Energy = Energy $(1/2mv^2)$). A good fit would mean that all the data points should form a line exactly along the black line.

For the first to second neutron scatters in Figure 33, the majority of points follow a broad line that is close to the black line. However, there are obvious problems with the calculated energies. The first is the vast number of points that exceed the 2.5 MeV threshold. The next is that the same unusual pattern, shown in Figure 32, of the large number of 2 and 2.5 MeV scattered neutrons. For the second to third neutron scatters in Figure 33, the points do not follow the black line, meaning a bad fit. In fact, the data behaves almost opposite to that of the 1st to 2nd scatter, where the calculated energy underestimates the energy compared to the Geant4 value. In fact, all points are found below the black line. For the third to fourth neutron scatters in Figure 33, the points are more concentrated below the black line, however, there is a fair number of extremely unrealistic and overestimated values calculated by MATLAB. A large portion of data points are located extremely higher than expected.

Overall, the simulated neutron scattering behavior exhibited within the plastic scintillating fiber bundle is unusual and unexpected. The first to second neutron scatters mostly demonstrate matching values (follow the black line, Figure 33) for almost all neutron energies from 0 to 2.5, with the exception of the regions around 2 and 2.5 MeV. The second to third neutron scatter neutron energies are underestimated by the MATLAB post-processing script values. The third to fourth neutron scatter energies shows some resemblance to the 2nd to 3rd neutron scatter energies, except there are some scatters which are greatly overestimated by the MATLAB post-processing script, when compared to the Geant4 simulation. It is not clear why the neutron energy values change drastically from scatter to scatter when comparing the kinetic energy calculation, from Equation 33, to the Geant4 simulation energies.

4.2 Digital Oscilloscope Findings

The various timing experiments, data collection techniques and results from the digital oscilloscope are presented in this section. The fast acquisition mode of the Tektronix DPO7104 digital oscilloscope proved to be an interesting feature when controlled by MATLAB through a LAN cable by means of TekVISA. The original MATLAB script for performing fast acquisition on the Tektronix scope was written by Gearhart [2]. The script was modified for the various experiments performed in this research, and the procedures for these experiments were described previously in Section 3.4.

An important component of the neutron spectrometer detection system is having a data collection system fast enough to capture the neutron double scatter events from the responses generated by the SiPMTs. To determine the speed and responsiveness of the digital oscilloscope, multiple timed data collection experiments were performed using the procedures detailed in Section 3.4. The results for the complete collection times are found in Tables 11 and 12. Table 11 shows the results when the frequency is held at 5000 kHz, and Table 12 shows the results when the frequency is 1 kHz. Recall the definition and depiction of the a waveform from Section 2.6 (Figure 18).

Tables 11 and 12 reveal that for equivalent size sets the 5 MHz signal is collected faster than the 1 kHz signal. Plotting the sets and applying a linear fit provides the time per set, which is 1.82 and 2.95 seconds per set for the 5 MHz and 1 kHz, respectively. The fraction term is defined as the number of pulses that are collected out of total possible pulses. Calculating the fraction term requires solving for the total number of pulses collected, as well as the total number of possible pulses. The total number of collected pulses is

$$N_{CP} = N_S \cdot N_{W/S} \cdot N_{P/W} , \quad (34)$$

where, N_{CP} is the number of collected pulses, N_S is the number of sets, $N_{W/S}$ is the number of waveforms per set, and $N_{P/W}$ is the number of pulses per waveform. The total number of possible pulses is

$$N_{PP} = f \cdot t, \quad (35)$$

where, N_{PP} is the number of possible pulses, f is the frequency of the signal, and t is the amount of time it takes the digital oscilloscope to collect the number of sets requested. After solving for Equations 34 and 35, they are combined to form Equation 36 which calculates the fraction term and is

$$F = \frac{N_{CP}}{N_{PP}}, \quad (36)$$

where, F is the fraction term. This fraction is based on the entire acquisition time, which only occurs during the first part of the MATLAB script. The other three functions are the ask, read, and save; presented in Figure 35.

Table 11. Collection times for a 5000 kHz pulse, where each set is comprised of 1000 waveforms ($N_{W/S}$).

Frequency f (kHz)	Sets N_S	Pulse/Wvfrm $N_{P/W}$	Time t (sec)	Fraction F
5000	1	5	1.7426	0.00057
5000	2	5	3.6744	0.00054
5000	3	5	5.4353	0.00055
5000	5	5	9.4352	0.00053
5000	10	5	18.0862	0.00055
5000	25	5	45.9288	0.00054
5000	50	5	91.5124	0.00055
5000	100	5	183.0905	0.00055
5000	250	5	459.0819	0.00054
5000	500	5	921.4503	0.00054
5000	1000	5	1818.4000	0.00055

Table 12. Collection times for a 1 kHz pulse, where each set is comprised of 1000 waveforms ($N_{W/S}$).

Frequency f (kHz)	Sets N_S	Pulse/Wvfrm $N_{P/W}$	Time t (sec)	Fraction F
1	1	1	2.8491	0.351
1	2	1	5.5149	0.363
1	3	1	8.4308	0.356
1	5	1	13.9045	0.360
1	10	1	29.2551	0.342
1	25	1	69.6045	0.359
1	50	1	139.7677	0.358
1	100	1	284.2040	0.352
1	250	1	716.8098	0.349
1	500	1	1480.7000	0.338
1	1000	1	N/A	N/A

An initial comparison of the varying number of sets taken at 5000 kHz and 1kHz reveals the time required for collection is less for signals with higher frequency. This is due to the fact that the higher frequency signal produces more pulses in a shorter amount of time and the lower frequency signal produces pulses over a longer amount of time. A simple illustration showing this difference in frequencies is provided in Figure 34. The consequence of a higher frequency signal input is an increased difficulty in collecting all the possible pulses during the acquisition. This is shown in the fraction column of Tables 11 and 12, where more of the lower frequency signal was collected than the higher frequency. Additionally, the fraction of total pulses collected did not change as the number of acquisition sets changed. This indicates that each acquisition set within a collection run takes approximately the same amount of time to complete.

The placement of internal MATLAB timing functions to breakdown the entire collection system into four distinct functions of acquire, ask, read, and save provides a better understanding of the actual time it takes to acquire waveforms. These four stages also provide the true total of possible pulses the digital oscilloscope could collect

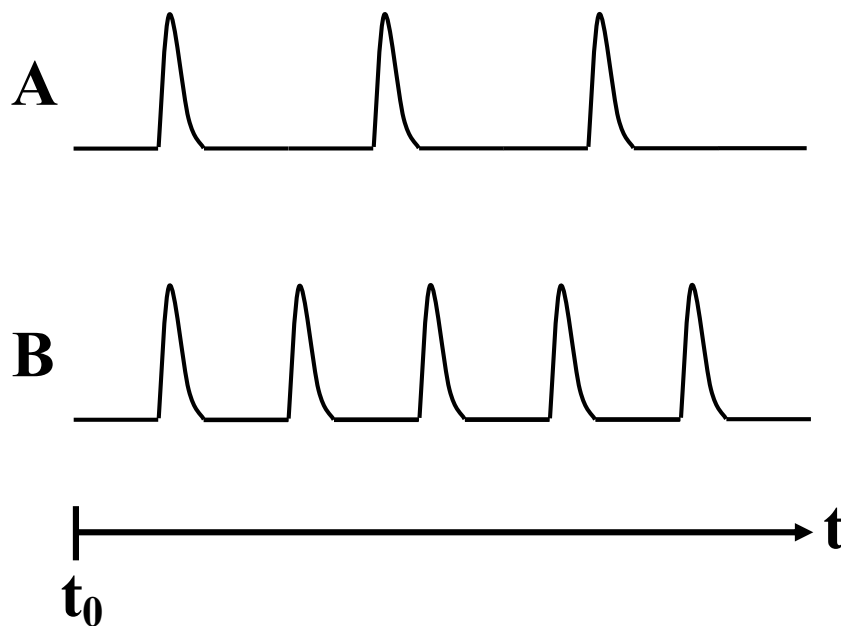


Figure 34. Comparison of two different frequency signals. Signal A has a lower frequency than signal B. If the same amount of time, t , is used to collect signals A and B, then it is expected that a greater number of pulses (or counts) will register for signal B than for signal A. Same logic follows that for a desired number of pulses (counts), signal B will take less time (t) to reach the desired number than signal A.

during the acquire phase of the run. The frequency was varied from 0.1–5000 kHz, the set number was held constant and the number of waveforms per set was varied in decades from 1–1000. The results, located in Appendix G, for 1 and 10 waveforms per set are provided in Table 16 and the results for 100 and 1000 waveforms per set are provided in Table 17. The collection times can be more easily analyzed when plotted, as shown in Figure 35.

There are a few distinguishable relationships between the collection times, frequency, and waveforms per set. The first relationship observed is between the number of waveforms per set and the collection time. The acquire, read, and save times increased as the number of waveforms per set increased. There was negligible change in ask time as the waveforms per set increased. As more data is collected (e.g. increase in waveforms per set) it takes more time to perform the same tasks because more

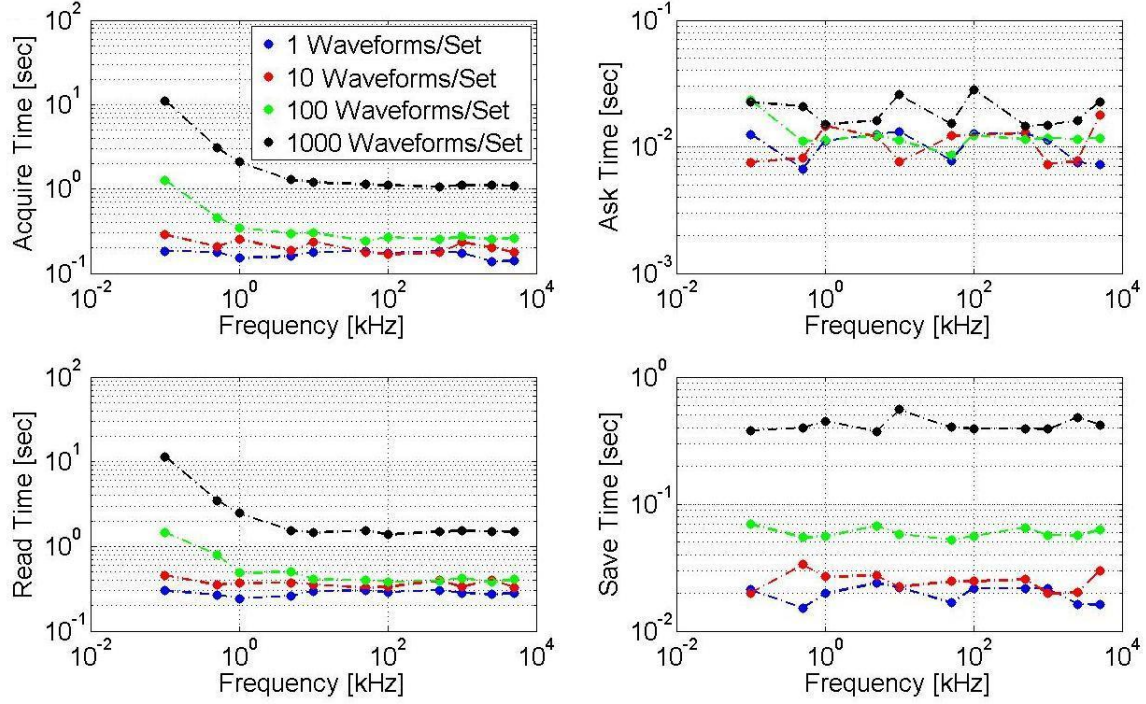


Figure 35. Comparison of the various time components of a single fast digital data acquisition. The four plots show how each of the functions in a single acquisition affect the total time to perform the data collection. (*Top Left*) The “acquire time” directly relates to a change in frequency and/or waveform per set. (*Top Right*) The “ask time” demonstrates a negligible adjustment to a change in frequency and/or waveform per set. (*Bottom Left*) The “read time” reacts the same as the acquire time, where there is a direct relationship between the read time and a variation in frequency and/or waveform per set. (*Bottom Right*) The “save time” demonstrates no relation with frequency, but directly relates to a change in waveform per set. Both the acquire time and read time dominate the entire collection time by two orders of magnitude for frequencies less than 10 kHz, when compared to the ask time and save time. The acquire and read times are only one order of magnitude larger in time for frequencies greater than 10 kHz. Note: the legend in the acquisition time vs frequency plot applies to all four plots.

information (i.e. more memory) is required to process the task. Another relationship determined is that with increasing frequency the time required for acquisition and read time reduces. If the frequency increases it takes less time to acquire and read the same amount of requested waveforms per set, as an increase in frequency translates to an increase in pulses over the same duration of time; recall Figure 34. In general, the ask and save times stayed constant with increasing frequency. While these appear to be simple correlations, a trade-off between the user defined variables

(e.g. number of data points per waveform, number of waveforms per set, number of sets, oscilloscope time per division, and frequency) is needed to determine an appropriate balance of overall collection time and fidelity of measured data points. In an experimental setting, however, the pulse frequency will be a function of, among other factors, the fiber bundle size, the number of incident neutrons, and the neutron's kinetic energy.

One such case is evident in the fraction of pulses collected as a function of frequency. A few variables affect the fraction of total pulses collected, including the oscilloscope sample rate, the number of pulses per waveform, the number of points per waveform, the number of sets, and the frequency of the incoming signal. Figure 36 demonstrates several of these effects on the fraction of total pulses collected. The two relationships depicted in Figure 36 are 1) the fraction of total pulses collected by the oscilloscope decreases with increasing frequency, and 2) the fraction of total pulses collected increases with increasing number of waveforms per set. The more interesting feature of this plot is in the relationship shown at the highest frequencies. At the highest frequencies the fraction seems to remain roughly constant on a log scale. This is due to the fact that the frequencies are sufficiently high that even though the sample rate was not changed, more of the pulses were captured in a single waveform. All of the frequencies at or below 1 MHz had only one pulse per waveform, while the 2.5 and 5 MHz frequencies had 3 and 5 pulses per waveform, respectively.

A few important considerations are helpful to efficiently and effectively use the Tektronix DPO7104 digital oscilloscope fast digital data acquisition setting to obtain fast signals, which is needed in TOF neutron spectroscopy. These considerations include time and diligence in running multiple tests varying all the parameters to collect fast signals. These tests provide information as to the time, collection efficiency, system dead time, and data uncertainty. All of the parameters can then be

adjusted to provide the experimental conditions needed to bound the fast digital data acquisition results to an appropriate scope required for successful experimentation. In this research a desired scope of experimentation would attempt to distinguish the difference in the position measurements of the fast signals to within a centimeter and the timing measurements of the fast signal to within 1–2 ns. A more detailed discussion of experimental bounds and uncertainty is presented in Section 4.4.

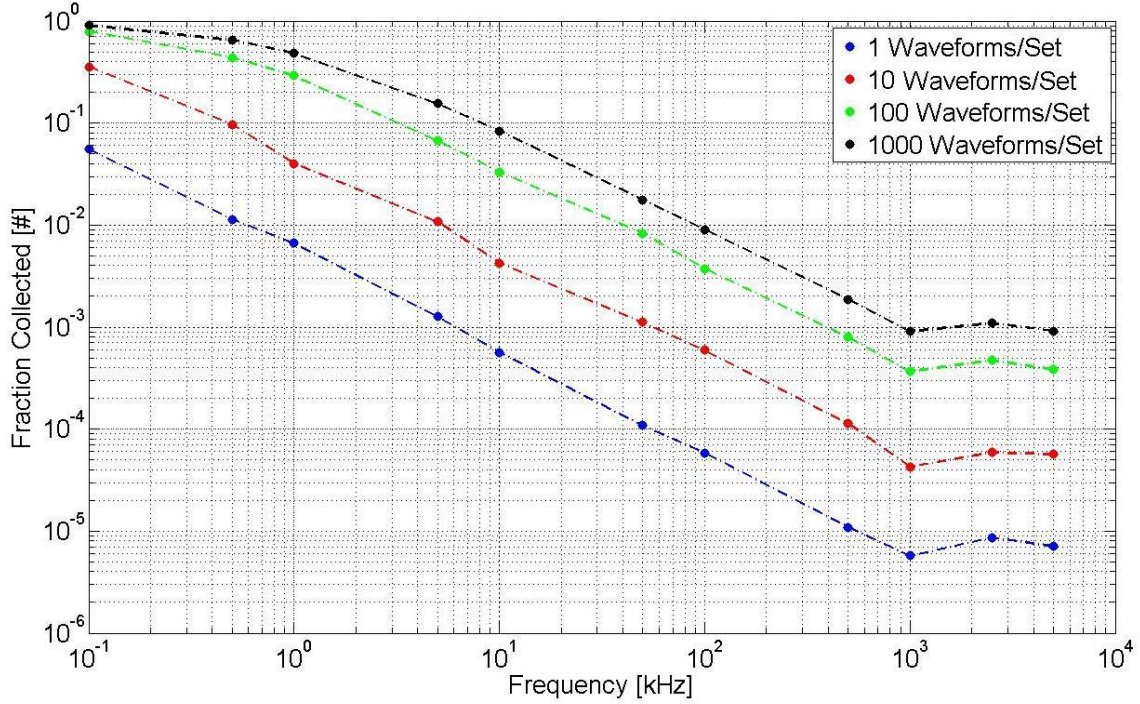


Figure 36. The fraction of the total pulses collected by the digital oscilloscope as the frequency (f), number of waveforms per set ($N_{W/S}$), and number of pulses per waveform changes ($N_{P/W}$).

4.3 Scintillation Yield Findings

A MATLAB routine was generated to compare the various scintillation photons which can be detected by a particular photosensor, specifically the Hamamatsu S10362-11 series. The energy deposited by an incident neutron was varied from 0–2.5 MeV, while the SiPMTs used in these experiments were 025C models. Theoretically,

the dark counts produced by these SiPMTs are on the level of approximately $1 - 3$ photons per $10 \mu\text{s}$. This means the minimal background to overcome is at least output pulses on the scale of 2 photon pulses. Other additional background noise is produced in the overall detection system and environment. Depending on the other equipment in the overall detection system (e.g. NIM bin, preamplifiers, oscilloscope, power supply) and the environment (i.e. the laboratory equipment in the same room, neighboring computers, electrical wiring in the building, boiler in the building turning on/off), both producing noise, the additional background noise can be anywhere from two to tens of photon pulses. Essentially, the equipment and the building provide too noisy of an environment for precise measurements on the 1 to 100s of photon detection scale. The photosensor threshold of detection for incoming scintillation events then needs to surpass this value to be distinguished from background noise. The data plotted in Figure 37 shows the minimum energy deposition, per scattering event, resulting in the collection of optical photons for several types of scintillating fibers.

According to Figure 37, if 20 total photons are collected by the BCF-12 fiber dual-readout Hamamatsu S10362-11-025C SiPMTs, the anticipated amount of energy imparted by the neutron is between $300 - 700 \text{ keV}$, depending on the geometry and layers of cladding of the fiber. The number of photons collected by the SiPMTs increases with trapping efficiency. The square geometry has a greater trapping efficiency than round fibers, as do fibers with multiple cladding layers. Hamamatsu also has other SiPMTs in the same series with varying numbers of pixels and efficiencies. These experiments used the 025C series SiPMT; the 050C and 100C series SiPMTs have a greater quantum efficiencies, allowing for lower levels of deposited neutron energy to be detectable by the scintillating fiber and SiPMT system. Due to time and budget constraints, however, the only available SiPMTs for the initial testing were the 025Cs.

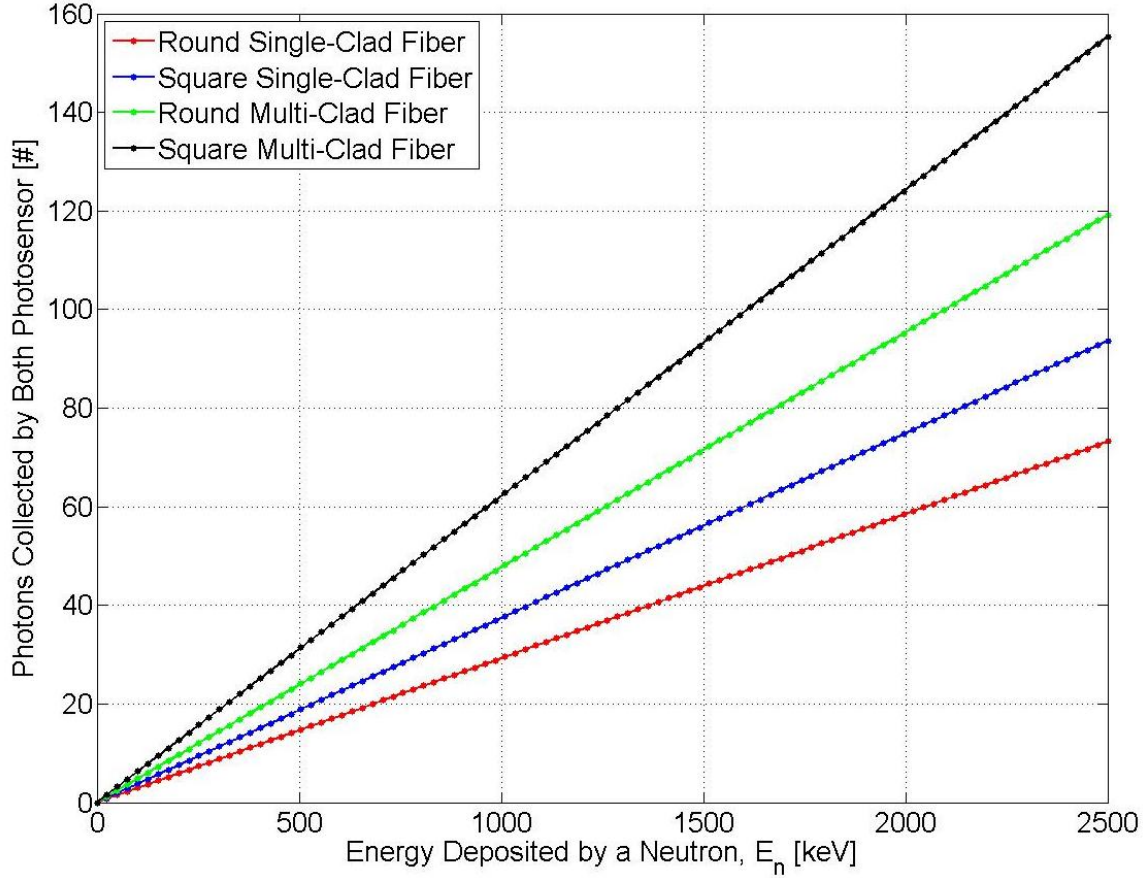


Figure 37. Comparison of approximate number of scintillation photons detected by a SiPMT as a function of trapping efficiency. This assumes using a Hamamatsu S10362-11-025C Series SiPMT and a BCF-12 plastic scintillating fiber 30 cm in length with the position-of-interaction occurring at the middle of the fiber. The trapping efficiency of the the Saint-Gobain fibers changes with the fiber geometry and layers of cladding. In order of top to bottom in the legend the trapping efficiencies increase as 3.44%, 4.50%, 5.60%, and 7.30%.

4.4 Spatial and Timing Resolution

The results pertaining to the spatial and timing resolution parametric study will be presented and analyzed in this section. A time-of-flight plastic scintillating fiber bundle neutron spectrometer is only helpful if the timing and spatial resolution are very precise. This section presents theoretical approximations and calculations to predict the spatial and timing resolution limits. Future research at the AFIT D-D neutron generator will be performed to validate these predictions.

The algorithm used for this parametric study calculated the energy, the energy uncertainty, and the relative error associated with the energy calculation. These calculations were performed with the position uncertainty defined as 1 mm and the timing uncertainty defined as 0.1 ns; these values were chosen to bound the overall relative percent uncertainty to less than 10%. The energy and its uncertainty for the energy range of 0–3 MeV is shown in Figure 38. This energy range was chosen as it corresponds to the energy of the neutrons generated by a D-D neutron generator. The energy is calculated using the kinetic energy equation from Section 4.1.2, Equation 33. The velocity is calculated using two matrices of distance and time, where the distance, dx , ranges from 1–100 cm, and the time, t , ranges from 1–10 ns. The energy uncertainty was calculated using Equation 27, where the same ranges in distance and time are used with a distance uncertainty (σ_z) set to 1 mm and a timing uncertainty (σ_t) set to 0.1 ns.

The results show an interesting relationship between the energy, position, and time, where the position drastically produces greater change than changes in time. This means that for a relative percent change in position will more greatly affect the energy than the the same relative percent change in time. For acceptable results the uncertainty should not be greater than 10%. A relative energy uncertainty (i.e. σ_E/E) equal to 0.10 (i.e. 10%) would provide the “acceptable” position and timing limitations of a TOF neutron spectrometer. This relative uncertainty was calculated and is depicted in Figure 39. The plot shows contour lines, which represent the relative energy uncertainty. The relative energy uncertainty greatly increases at ~ 1.75 nanoseconds for all positions and 2 cm for all times. The 10% uncertainty threshold occurs at about 2 cm and 2 ns. This means that the energy and its uncertainty are considered acceptable (i.e. having a relative error less than 10%) if the position and time are greater than 2 cm and 2 ns, respectively.

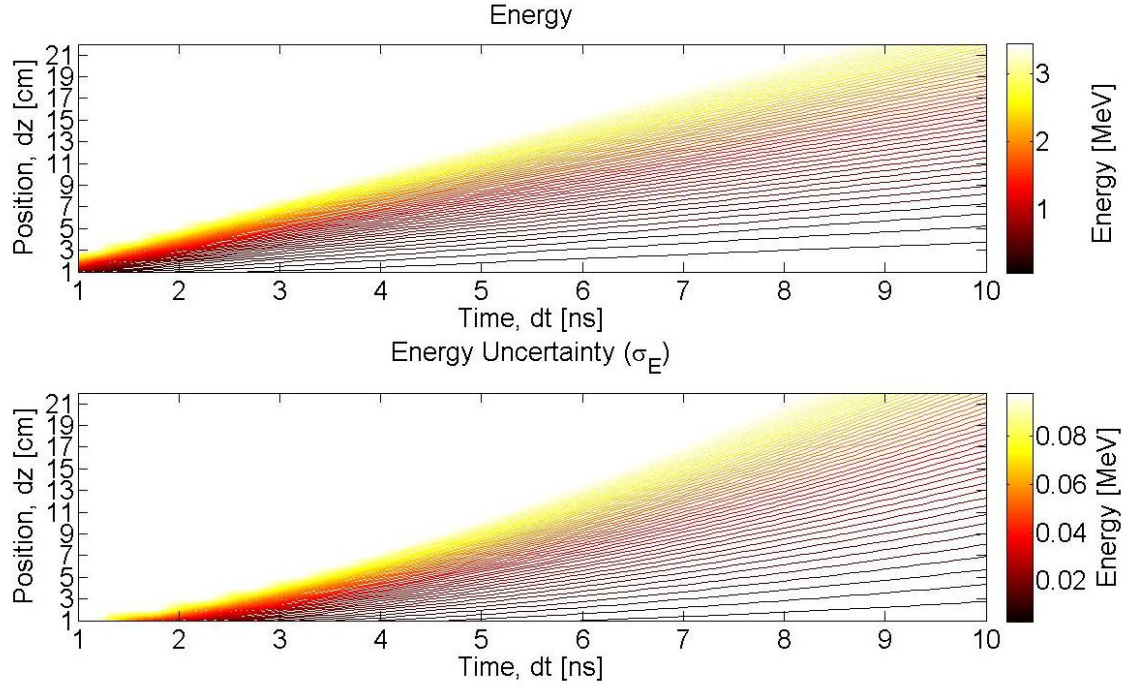


Figure 38. The energy and its uncertainty for calculated energies of 0-3 MeV and below based on a position uncertainty of 1 mm and timing uncertainty of 0.1 ns. Note for illustrative purposes the white region in the top left corners of both plots can be ignored since to get the appropriate scale the values were fixed.

Calculating the energy of a neutron traversing through a scintillator using position and time measurements with uncertainties of 1 mm and 1 ns, respectively, as inputs to Equation 39 produces an answer with a relative error of approximately 10% or less, provided two conditions are met. The conditions include: 1) the measured value of distance (i.e. position) is greater than ~ 2 cm, and 2) the measured time is greater than ~ 2 ns. Take as a sample calculation, a neutron measured traveling 5 cm into a scintillator and taking 3 ns to traverse this distance, denoted as a green circle in Figure 39. These measured values result in a calculated energy of 1.45 ± 0.141 MeV; where the relative error is approximately 8% since the measured values are less than the 10% relative error contour, denoted in blue, shown in Figure 39.

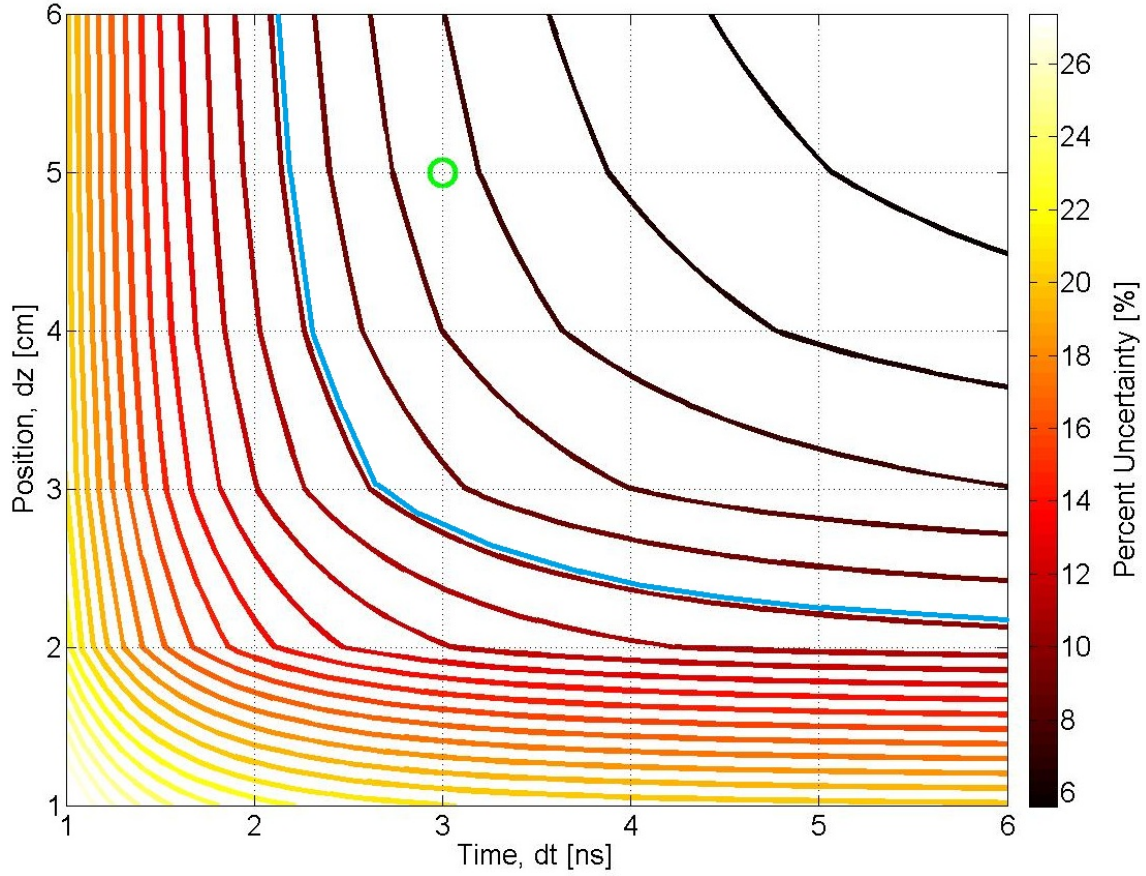


Figure 39. Percent uncertainty shown as the relative percent uncertainty of σ_E with respect to energy, E . The contours show a sharp increase below ~ 1.75 ns and below 2 cm. This is where the ten percent uncertainty threshold is obtained for a position uncertainty of 1 mm and a timing uncertainty of 0.1 ns. The green circle denotes an energy of 1.45 ± 0.141 MeV at a position of 5 cm and time of 3 ns. The blue contour line denotes a relative error of 10%.

4.5 SiPMT Findings

This section describes the various experiments and attempts to use and collect dark count information from the silicon photomultiplier multi-pixel photon counting photosensors. The information provided will be more of a discussion and summary of data collected from the SiPMTs since working with the silicon photomultipliers required many trial and error sessions. The overall goal was to verify the dark counts of the Hamamatsu S10362-11-025C SiPMTs. The two SiPMTs used in these experiments had manufacturer specified dark count measurements of 323 kcps for the

SiPMT A and 318 kcps (Channel 1) for SiPMT B (Channel 2). As mentioned in Section 3.6, there were several SiPMT circuit board diagrams utilized for providing a bias voltage and means to readout the signal from the SiPMT. To save on time and to reduce repetition of experiments, only data from the final circuit board design will be presented in this analysis of the background counts of the SiPMTs without a fiber or radiation source present.

The two SiPMTs mounted on the circuit board in Figure 24 were placed inside aluminum jigs, mounted inside the aluminum box with the voltage sources connected and set at -70 ± 0.03 Volts. The signal outputs were connected to two separate preamplifiers, which were then connected to Channel 1 and Channel 2 of the oscilloscope. With no source or fiber present, 2 million pulses (i.e. waveforms) were recorded for each channel. An example of the output signal from the SiPMTs when fast acquisition mode is on is shown in Figure 40. Notice the pulses at the trigger point increase in amplitude by approximately 0.3 V increments. The output displayed on the oscilloscope is as expected, since each photon detected will cause equivalent incremental step increases in the voltage output.

The post-processing of data provides several pieces of information, including the pulse height distribution of each SiPMT. The calculated number of dark counts are only an approximation, as the single photon pulse height was not verified. The smallest single photon pulse height was estimated based on data collected, then used to estimate the number of photons resulting in pulses greater than those from single photons. The distribution of pulses from SiPMT A (i.e. Channel 1) and SiPMT B (i.e. Channel 2) are given in Figure 41. The distribution shows the single and double firing pixels at 0.125 and 0.25 V, respectively, which is similar to the distribution found in Jones' research [3]. On close inspection, the two distributions are nearly identical, with the number of counts varying slightly. There is also a slight decrease

in the peak voltages from Channel 1 to Channel 2.

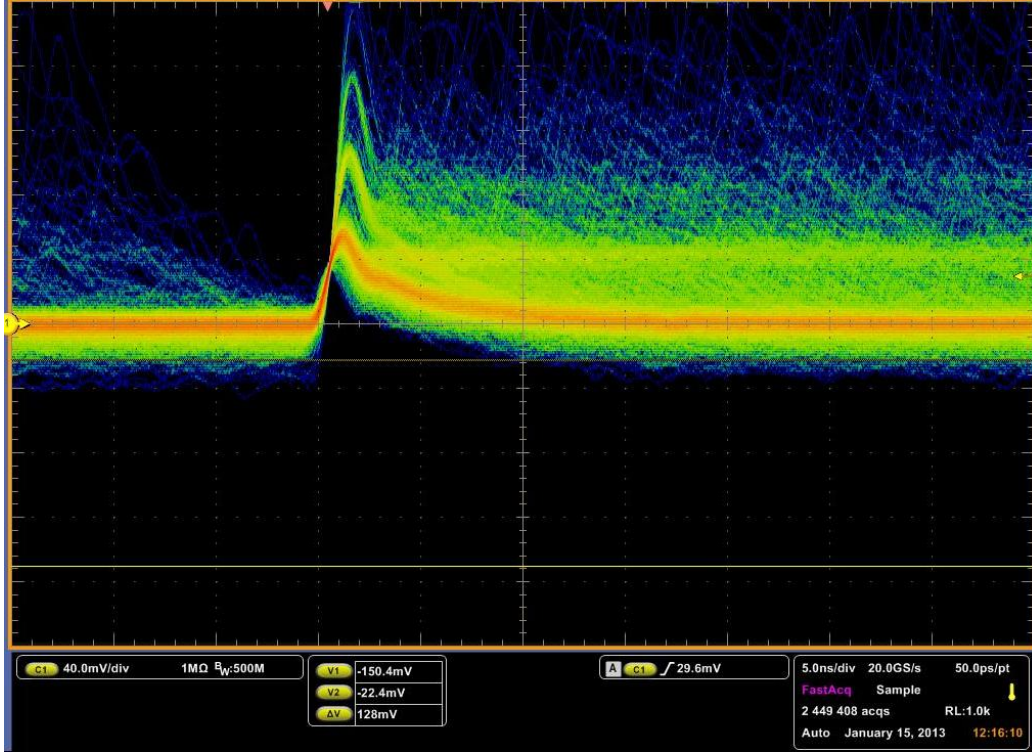


Figure 40. A snapshot of the oscilloscope showing a sample of the pulses produced by Hamamatsu S10362-11-025C SiPMT. The Tektronix DPO7104 digital oscilloscope was used with fast acquisition setting turned on. The the y-axis is at 40 mV/div and the x-axis is at 5 ns/div. The trigger level was set to 30 mV.

The dark counts were calculated using a single photon pulse height of 0.1 V. This means that a 0.3 V pulse will be counted as 3 photons (i.e. 3 dark counts). The MATLAB script first went through the data finding all the local minimum and maximum points, analyzing each waveform and marking the local minimums and maximums when the data stopped increasing or decreasing, providing potential pulse heights for inspection. If a pulse height was determined to be above 0.1 V, it was considered a photon induced event. Each photon induced pulse was then divided by 0.1 V to determine if it was a multi-photon induced pulse; after eliminating all true pulses, dark count rates of approximately 414 kcps and 475 kcps were recorded for SiPMT A and B, respectively. These are higher than the manufacturer's reported values, but well below the maximum rate of 600 kcps specified for both devices.

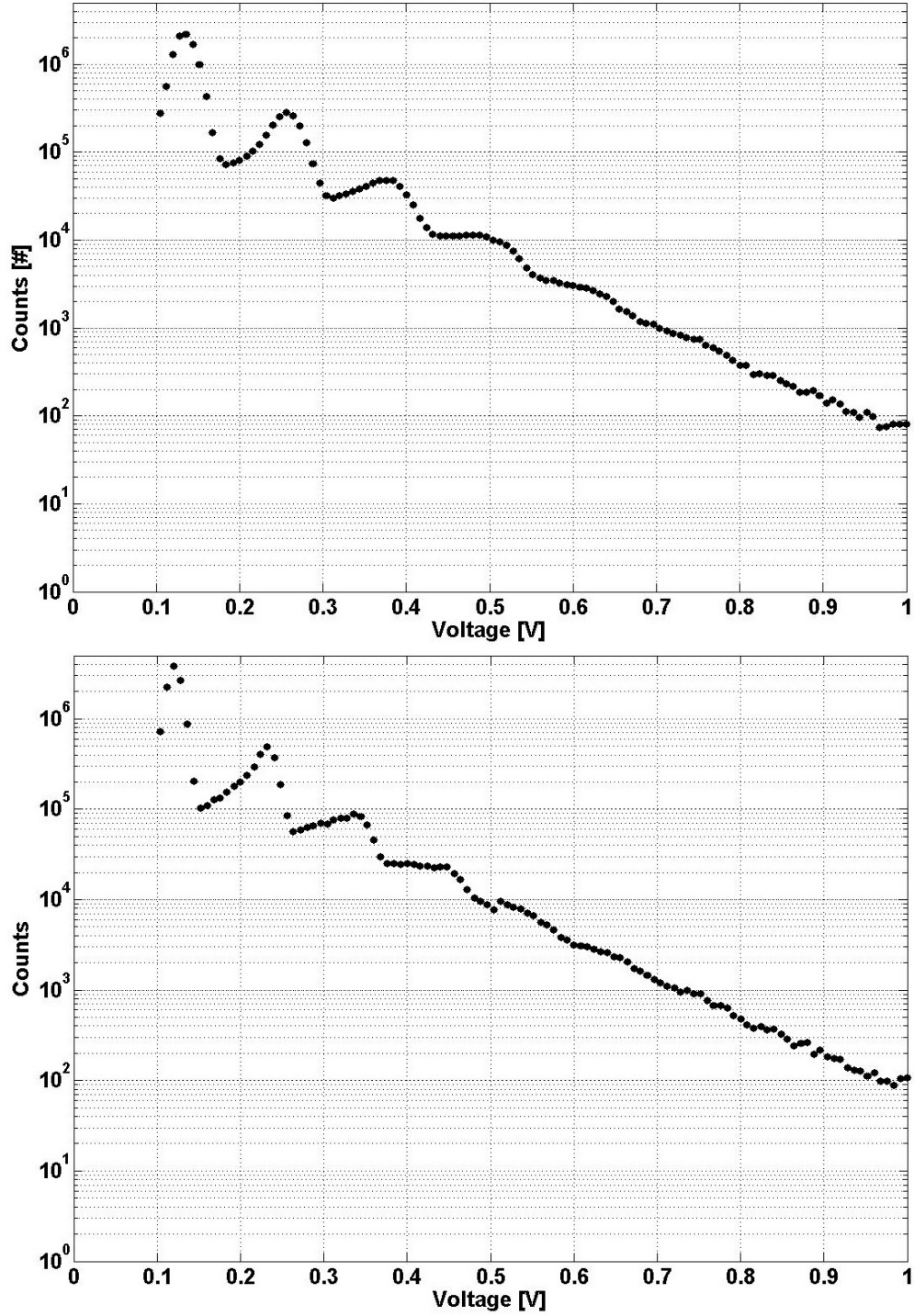


Figure 41. (*Top*) The pulse height distribution of the dark counts from SiPMT A (Channel 1). The peaks are centered at approximately 0.125, 0.25, 0.375, and 0.5 V. (*Bottom*) The pulse height distribution of the dark counts from SiPMT B (Channel 2). The peaks are centered at approximately 0.12, 0.23, 0.34, and 0.45 V. The voltage was set to -70 ± 0.03 V. There was no source or scintillating fiber present in the aluminum light-tight box. Each pulse peak represents an additional pixel firing from the SiPMT.

V. Conclusion & Recommendations

The premise of a novel time-of-flight neutron spectrometer composed of an array of plastic scintillating fibers connected to a silicon photomultiplier is founded on the basic concepts of a scintillator material with a high efficiency, photosensors with high efficiency, and an fiber bundle array with a high probability of double neutron scatters. This research attempted to address the limiting boundaries of various components of a neutron spectrometer based on BCF-12 plastic scintillating fibers. The hope is this research can be continued with an experimental follow-up to compare the modeling results with real data.

Organic plastic scintillating fibers coupled with highly efficient SiPMTs for neutron spectroscopy is only promising if the fibers and SiPMT are efficient. The SiPMTs produced by Hamamatsu range from 25 to 80% in efficiency. The BCF-12 fibers produced by Saint-Gobain have a trapping efficiency of 3.44%. If other more efficient fibers exist, then I would greatly recommend using them. The double scattering of neutrons in the scintillator is crucial, and the 14×14 BCF-12 plastic scintillating fiber bundle simulation demonstrated that only 0.359% of the neutrons incident on the 30 cm long fiber would actually double scatter. The number of double scatters can be increased by changing the trajectory of the incident neutrons, say for neutrons incident in the direction of the axial direction. A 14×14 fiber bundle composed of 500 μm diameter fibers is $\sim 7 \times 7$ mm, if the array size were increased the double scatter efficiency would increase.

The 14×14 BCF-12 scintillating fiber bundle created in Geant4 provides valuable simulated data for processing pertinent information pertaining to neutron scattering, energy deposition, location of scattering events, distances, and times of the scatters. All of this can be used to obtain desired information on expected performance of a plastic scintillating bundle as a TOF neutron spectrometer. Experiments can be

performed on the modeled 14×14 BCF-12 bundle to see how well the real bundle compares to the model. The Geant4 simulations provide, at a minimum the fundamental basis that a TOF neutron spectrometer can be built out of scintillating fibers attached to a photosensor.

Scintillators require extremely fast data acquisition since the photons are traveling close to the speed of light. The Tektronix DPO7104 digital oscilloscope controlled by MATLAB through TekVISA via a LAN cable provides fast data collection and transfer. While this research only found that small fractions of the total incident pulses will actually get recorded by the oscilloscope, some better coding of the communication between the oscilloscope and computer could increase the efficiency. The advantage of this oscilloscope is its ability to distinguish between points on the pico and femto second time scales.

Some of the boundaries at which a proposed TOF neutron spectrometer can perform were determined. Based on the timing and spatial uncertainties and error propagation, the position resolution and timing resolution can help to quickly determine if a scintillator will be able to resolve the position-of-interaction well enough for its intended application. For a spatial uncertainty of 1 mm and a timing uncertainty of 0.1 ns the uncertainty in time and position quickly reach a relative error of 10% at approximately 1.75 ns and below 2 cm, respectively. Changing the established time and spatial uncertainties to a desired or experimentally determined value and then evaluating those parameters in the parametric studies performed here, will allow for timing and spatial bounds to be understood for current or future materials.

The actual construction, testing, and experimentation of the aluminum light-tight boxes with the SiPMTs only proved that making a light-tight apparatus is extremely difficult and that the Hamamatsu silicon photomultiplier multi-pixel photon counting sensors are extremely sensitive. The higher the quantum efficiency the better, thus

the model 100C is highly recommended. The BCF-12 fibers are only generating ~ 800 photons per MeV. Combine this with a very low trapping efficiency, quenching, attenuation length losses and the number of photons reaching the end of a fiber is severely reduced from thousands to tens of scintillation photons. Depending on the dark counts and other background noise the minimal energy deposited by a neutron required to distinguish a scatter from background is between $300 - 700$ keV, depending on the quantum efficiency of the photosensor.

Finally, all the simulations, parametric studies, and experiments performed here are provided in the hope that the research is continued. Experimental data using the 14×14 BCF-12 scintillating fiber bundle would be a great start in continued research towards the goal of a TOF neutron spectrometer composed of plastic scintillating fibers. The Geant4 model results allows for future experimental results to be compared. The AFIT D-D generator can provide the neutron source for the experiment. The 14×14 bundle should be subjected to neutrons from the D-D neutron generator for approximately 30 minutes to have an equivalent comparison to the 1×10^6 Geant4 model results. The experiment requires that the fiber bundle is placed lengthwise parallel and 6 inches away from the D-D neutron generator. The range of energies expected to be witnessed from this exposure to the neutron generator will range from $0.3 - 2.3$ MeV. A spatial and timing resolution of 1 mm and 1 ns will be needed to compare experimental measurements to the analyses performed in this research. The analyses on the timing and spectroscopy requirements for a plastic scintillating fiber bundle time-of-flight neutron spectrometer has provided a firm foundation and to warrant additional experiments to compliment the research. The spatial and timing parametric studies will provide great insight to better understand the resolution levels required for highly precise TOF neutron spectrometers with plastic scintillating fibers, which remains a promising field of research.

Appendix A. 14×14 BCF-12 Plastic Scintillating Fiber Geant4 Post-Processing Script

```
%Written by 2d Lt Paul A. Clement
%29 January 2012
%Neutron Scattering in Fiber Bundle Post-Processing

% -----
% Updates:
% -----
% 2 Apr 13 - "...Ver2.txt" files only due to addition of scattering times
% 5 Apr 13 - Comparison of MATLAB (v^2) calculations to GEANT4 code energy
%           output in form of plots added

close all
clear all
clc

% Start Clock
tic;

fprintf('\nProgram Has Started...\n')

%% Load GEANT4 Output File

% List of outputs for the simulations ran should be one the following:
% test1mnVer2.txt
% test5mnVer2a.txt
% test5mnVer2b.txt
% test10mnVer2.txt
% test100mnVer2.txt

Raw_Data = load('E:\Masters Thesis\GEANT4\clement geant4\fb-build\test100mnVer2.txt');
% ^-- Check path and change accordingly, CHANGE HERE ^-----^ (*.txt)
% Column 1 = neutron # [unitless]
% Column 2 = scatter # [unitless]
% Column 3 = y/x-axis fiber identifier [unitless]
%           thousands/hundreds position is y-axis
%           tens/ones position is x-axis
% Examples: 1104 --> y-axis = 11, x-axis = 4
%           300 --> y-axis = 3, x-axis = 0
% Column 4 = location in fiber in [mm] from z-axis center
% Column 5 = energy in [keV] imparted from collision
% Column 6 = time in [ps] at scatter w.r.t. neutron birth

% Sample Raw_Data
% 59 1 309 -21.3482005336216 1325.60422901997 1066.86528777748
% 0 0 0 0 0 0
% 105 1 100 -35.2520903974052 1263.15390159812 1698.81495918306
% 0 0 0 0 0 0
% 117 1 304 -26.5427878736108 228.517024084795 1310.07943337441
% 117 2 405 -26.8525676978072 632.237877118428 1332.21273046707
% 0 0 0 0 0 0
% 136 1 113 1.96765346606238 68.8682387677773 407.051507238058
% 0 0 0 0 0 0

% Remove zero rows in "Raw_Data"
Raw_Data( all(~Raw_Data,2), : ) = [];

%% Scattering Events and Energy Deposition

fprintf('\nScattering Tallies and Energy Deposition has Started...\n')
```

```

% Definitions
m_n = 1.008665*931.494*1.602E-13/(3E8)^2; % [kg] Mass of a Neutron
keV_per_J = (1/1.602E-16); % (1 [keV] / 1.602E-16 [J])

% Initialize
n_f = 14; % <-- Number of fibers in each row and column
n_particles = 10E6; % <-- Number of incident neutron particles (CHANGE)
scatters(4,1) = zeros;
y_loc(n_particles,4) = zeros;
x_loc(n_particles,4) = zeros;
z_loc(n_particles,4) = zeros;
fiber_bundle_s = zeros(n_f+1); % <-- Need desired amount +1 in dimensions for pcolor
fiber_bundle_d = zeros(n_f+1); % <-- Need desired amount +1 in dimensions for pcolor
fiber_bundle_m = zeros(n_f+1); % <-- Need desired amount +1 in dimensions for pcolor
fiber_bundle_q = zeros(n_f+1); % <-- Need desired amount +1 in dimensions for pcolor
scatt_energy(n_particles,4) = zeros;
remain_energy1(n_particles,1) = zeros;
remain_energy2(n_particles,1) = zeros;
remain_energy3(n_particles,1) = zeros;
remain_energy4(n_particles,1) = zeros;
dist_btwn_scatt1(n_particles,1) = zeros;
dist_btwn_scatt2(n_particles,1) = zeros;
dist_btwn_scatt3(n_particles,1) = zeros;
dist_btwn_scatt4(n_particles,1) = zeros;
dEdx_s(26,126) = zeros; % <-- Need desired amount +1 in dimensions for pcolor
dEdx_d(26,126) = zeros; % (26 bins of 100 [keV], 101 bins of 1 [mm])
dEdx_m(26,126) = zeros;
dEdx_q(26,126) = zeros;
time_s(n_particles,1) = zeros;
time_d(n_particles,1) = zeros;
time_m(n_particles,1) = zeros;
time_q(n_particles,1) = zeros;
velocity_s(n_particles,1) = zeros;
velocity_d(n_particles,1) = zeros;
velocity_m(n_particles,1) = zeros;
velocity_q(n_particles,1) = zeros;
E_calc_s(n_particles,1) = zeros;
E_calc_d(n_particles,1) = zeros;
E_calc_m(n_particles,1) = zeros;
E_calc_q(n_particles,1) = zeros;
E_to_E_calc_s(n_particles,2) = zeros;
E_to_E_calc_d(n_particles,2) = zeros;
E_to_E_calc_m(n_particles,2) = zeros;
E_to_E_calc_q(n_particles,2) = zeros;
j = 1;

% Scatter Tallies and Energy Imparted in each Fiber
for i = 1:length(Raw_Data)
    % Single
    if Raw_Data(i,2) == 1
        scatters(1,1) = scatters(1,1) + 1; % <-- Scatter Tally
        y_loc(j,1) = ((Raw_Data(i,3)-mod(Raw_Data(i,3),100))/100)+1; % <-- Fiber y-axis Location
        x_loc(j,1) = (mod(Raw_Data(i,3),100))+1; % <-- Fiber x-axis Location
        z_loc(j,1) = Raw_Data(i,4);
        fiber_bundle_s(y_loc(j,1),x_loc(j,1)) = fiber_bundle_s(y_loc(j,1),x_loc(j,1))...
            + Raw_Data(i,5);
        % ^-- Energy Deposited in [keV]
        scatt_energy(j,1) = Raw_Data(i,5); % <-- Retable neutron scatters
        % ^-- Columns 1-4 correspond to scatters 1-4 in [keV]
        remain_energy1(j,1) = 2500 - scatt_energy(j,1);
        % ^-- Remaining E_n after 1st scatter in [keV]
        dist_btwn_scatt1(j,1) = sqrt(((x_loc(j,1)*250E-4 - 1))^2 ...
            + ((y_loc(j,1) - 0)*250E-4)^2 ...
            + ((Raw_Data(i,4) - 0)*1E-1)^2);
        % ^-- Distance traveled between 0th and 1st n-scatter in [cm]
        dEdx_s(floor(remain_energy1(j,1)/100)+1,floor(dist_btwn_scatt1(j,1)*10)+1) = ...

```

```

    dEdx_s(floor(remain_energy1(j,1)/100)+1,floor(dist_btwn_scatt1(j,1)*10)+1) + 1;
    % ^-- Produces heat map, or contour map, or pcolor map
    time_s(j,1) = Raw_Data(i,6);
    % ^-- Time from neutron birth to 1st scatter in [ps]
    velocity_s(j,1) = dist_btwn_scatt1(j,1)/time_s(j,1)*(1E12/1)*(1/1E2);
    % ^-- Velocity of neutron from birth to 1st scatter in [m/s]
    E_calc_s(j,1) = 0.5*m_n*(velocity_s(j,1))^2*keV_per_J;
    % ^-- Energy (calc) of neutron from birth to 1st scatter in [keV]
    E_to_E_calc_s(j,1) = 2500;
    % ^-- Energy provided by GEANT4 model from birth to 1st scatter in [keV]
    E_to_E_calc_s(j,2) = E_calc_s(j,1);
    % ^-- Energy (calc) provided by MATLAB code from birth to 1st scatter in [keV]
% Double
elseif Raw_Data(i,2) == 2
    scatters(2,1) = scatters(2,1) + 1;
    y_loc(j-1,2) = ((Raw_Data(i,3)-mod(Raw_Data(i,3),100))/100)+1; % <-- Fiber y-axis Location
    x_loc(j-1,2) = (mod(Raw_Data(i,3),100))+1; % <-- Fiber x-axis Location
    z_loc(j-1,2) = Raw_Data(i,4);
    fiber_bundle_d(y_loc(j-1,2),x_loc(j-1,2)) = fiber_bundle_d(y_loc(j-1,2),x_loc(j-1,2))...
        + Raw_Data(i,5);
    % ^-- Energy Deposited in [keV]
    scatt_energy(j-1,2) = Raw_Data(i,5); % <-- Retable neutron scatters
    % ^-- Columns 1-4 correspond to scatters 1-4 in [keV]
    remain_energy2(j-1,1) = remain_energy1(j-1,1) - scatt_energy(j-1,2);
    % ^-- Remaining E_n after 2nd scatter in [keV]
    dist_btwn_scatt2(j-1,1) = sqrt(((x_loc(j-1,2) - x_loc(j-1,1))*250E-4)^2 ...
        + ((y_loc(j-1,2) - y_loc(j-1,1))*250E-4)^2 ...
        + ((Raw_Data(i,4) - Raw_Data(i-1,4))*1E-1)^2);
    % ^-- Distance traveled between 1st and 2nd n-scatter in [cm]
    dEdx_d(floor(remain_energy2(j-1,1)/100)+1,floor(dist_btwn_scatt2(j-1,1)*10)+1) = ...
        dEdx_d(floor(remain_energy2(j-1,1)/100)+1,floor(dist_btwn_scatt2(j-1,1)*10)+1) + 1;
    % ^-- Produces heat map, or contour map, or pcolor map
    time_d(j-1,1) = Raw_Data(i,6) - time_s(j-1,1);
    % ^-- Time from 1st to 2nd n-scatter in [ps]
    velocity_d(j-1,1) = dist_btwn_scatt2(j-1,1)/time_d(j-1,1)*(1E12/1)*(1/1E2);
    % ^-- Velocity of neutron from 1st to 2nd n-scatter in [m/s]
    E_calc_d(j-1,1) = 0.5*m_n*(velocity_d(j-1,1))^2*keV_per_J;
    % ^-- Energy (calc) of neutron from 1st to 2nd n-scatter in [keV]
    E_to_E_calc_d(j-1,1) = remain_energy1(j-1,1);
    % ^-- Energy provided by GEANT4 model from 1st to 2nd n-scatter in [keV]
    E_to_E_calc_d(j-1,2) = E_calc_d(j-1,1);
    % ^-- Energy (calc) provided by MATLAB code from 1st to 2nd n-scatter in [keV]
    j = j - 1;
% Triple
elseif Raw_Data(i,2) == 3
    scatters(3,1) = scatters(3,1) + 1;
    y_loc(j-1,3) = ((Raw_Data(i,3)-mod(Raw_Data(i,3),100))/100)+1; % <-- Fiber y-axis Location
    x_loc(j-1,3) = (mod(Raw_Data(i,3),100))+1; % <-- Fiber x-axis Location
    z_loc(j-1,3) = Raw_Data(i,4);
    fiber_bundle_m(y_loc(j-1,3),x_loc(j-1,3)) = fiber_bundle_m(y_loc(j-1,3),x_loc(j-1,3))...
        + Raw_Data(i,5);
    % ^-- Energy Deposited in [keV]
    scatt_energy(j-1,3) = Raw_Data(i,5); % <-- Retable neutron scatters
    % ^-- Columns 1-4 correspond to scatters 1-4 in [keV]
    remain_energy3(j-1,1) = remain_energy2(j-1,1) - scatt_energy(j-1,3);
    % ^-- Remaining E_n after 3rd scatter in [keV]
    dist_btwn_scatt3(j-1,1) = sqrt(((x_loc(j-1,3) - x_loc(j-1,2))*250E-4)^2 ...
        + ((y_loc(j-1,3) - y_loc(j-1,2))*250E-4)^2 ...
        + ((Raw_Data(i,4) - Raw_Data(i-1,4))*1E-1)^2);
    % ^-- Distance traveled between 2nd and 3rd n-scatter in [cm]
    dEdx_m(floor(remain_energy3(j-1,1)/100)+1,floor(dist_btwn_scatt3(j-1,1)*10)+1) = ...
        dEdx_m(floor(remain_energy3(j-1,1)/100)+1,floor(dist_btwn_scatt3(j-1,1)*10)+1) + 1;
    % ^-- Produces heat map, or contour map, or pcolor map
    time_m(j-1,1) = Raw_Data(i,6) - time_d(j-1,1);
    % ^-- Time from 2nd to 3rd n-scatter in [ps]
    velocity_m(j-1,1) = dist_btwn_scatt3(j-1,1)/time_m(j-1,1)*(1E12/1)*(1/1E2);

```

```

    % ^-- Velocity of neutron from 2nd to 3rd n-scatter in [m/s]
    E_calc_m(j-1,1) = 0.5*m_n*(velocity_m(j-1,1))^2*keV_per_J;
    % ^-- Energy (calc) of neutron from 2nd to 3rd n-scatter in [keV]
    E_to_E_calc_m(j-1,1) = remain_energy2(j-1,1);
    % ^-- Energy provided by GEANT4 model from 2nd to 3rd n-scatter in [keV]
    E_to_E_calc_m(j-1,2) = E_calc_m(j-1,1);
    % ^-- Energy (calc) provided by MATLAB code from 2nd to 3rd n-scatter in [keV]
    j = j - 1;
% Quad or More
elseif Raw_Data(i,2) >= 4
    scatters(4,1) = scatters(4,1) + 1;
    y_loc(j-1,4) = ((Raw_Data(i,3)-mod(Raw_Data(i,3),100))/100)+1; % <-- Fiber y-axis Location
    x_loc(j-1,4) = (mod(Raw_Data(i,3),100))+1; % <-- Fiber x-axis Location
    z_loc(j-1,4) = Raw_Data(i,4);
    fiber_bundle_q(y_loc(j-1,4),x_loc(j-1,4)) = fiber_bundle_q(y_loc(j-1,4),x_loc(j-1,4))...
        + Raw_Data(i,5);
    % ^-- Energy Deposited in [keV]
    scatt_energy(j-1,4) = Raw_Data(i,5); % <-- Retable neutron scatters
    % ^-- Columns 1-4 correspond to scatters 1-4 in [keV]
    remain_energy4(j-1,1) = remain_energy3(j-1,1) - scatt_energy(j-1,4);
    % ^-- Remaining E_n after 4th scatter in [keV]
    dist_btwn_scatt4(j-1,1) = sqrt(((x_loc(j-1,3) - x_loc(j-1,2))*250E-4)^2 ...
        + ((y_loc(j-1,3) - y_loc(j-1,2))*250E-4)^2 ...
        + ((Raw_Data(i,4) - Raw_Data(i-1,4))*1E-1)^2);
    % ^-- Distance traveled between 3rd and 4th n-scatter in [cm]
    dEdx_q(floor(remain_energy4(j-1,1)/100)+1,floor(dist_btwn_scatt4(j-1,1)*10)+1) = ...
        dEdx_q(floor(remain_energy4(j-1,1)/100)+1,floor(dist_btwn_scatt4(j-1,1)*10)+1) + 1;
    % ^-- Produces heat map, or contour map, or pcolor map
    time_q(j-1,1) = Raw_Data(i,6) - time_m(j-1,1);
    % ^-- Time from 3rd to 4th n-scatter in [ps]
    velocity_q(j-1,1) = dist_btwn_scatt4(j-1,1)/time_q(j-1,1)*(1E12/1)*(1/1E2);
    % ^-- Velocity of neutron from 3rd to 4th scatter in [m/s]
    E_calc_q(j-1,1) = 0.5*m_n*(velocity_q(j-1,1))^2*keV_per_J;
    % ^-- Energy (calc) of neutron from 3rd to 4th scatter in [keV]
    E_to_E_calc_q(j-1,1) = remain_energy3(j-1,1);
    % ^-- Energy provided by GEANT4 model from 3rd to 4th scatter in [keV]
    E_to_E_calc_q(j-1,2) = E_calc_q(j-1,1);
    % ^-- Energy (calc) provided by MATLAB code from 3rd to 4th scatter in [keV]
    j = j - 1;
else
    continue
end
j = j + 1;

% Print percent complete
percent = i/length(Raw_Data)*100;
fprintf('\nScattering Tallies and Energy Deposition is at %8.4f %% taking %6.2f sec',percent, toc)
end

fprintf('\nScatter Tallies and Energy Deposition is Complete taking %6.2f sec...\n',toc)

fiber_bundle_t = fiber_bundle_q + fiber_bundle_m + fiber_bundle_d + fiber_bundle_s;

dEdx_t = dEdx_q + dEdx_m + dEdx_d + dEdx_s;
dEdx_final = dEdx_t(1:26,1:51);

%% Plot Scattering Events (Un-Normalized)

figure(1)
bar(scatters,0.5,'k');
hold on
text(1:1:4,scatters,num2str(scatters,'%0.0f'),...
    'HorizontalAlignment','center','VerticalAlignment','bottom','fontsize',20)
%title('Histogram of Neutron Scatters in a 14x14 BCF-12 PSF Bundle','fontsize',20);
xlabel('Scatters by a Single Neutron [#'],'fontsize',20);

```

```

ylabel('Counts [#]', 'fontsize', 20);
set(gca, 'box', 'on', 'fontsize', 20);
set(gcf(1), 'units', 'normalize', 'outerposition', [0 0 1 1]);

fprintf('\nHistogram of Scattering (Normalized) Complete taking %6.2f sec...\n', toc)

%% Plot Scattering Events (Normalized)

figure(2)
bar(scatters./(n_particles*10), 0.5, 'k');
hold on
text(1:1:4, scatters./(n_particles*10), num2str(scatters./(n_particles*10), '%0.5f'), ...
    'HorizontalAlignment', 'center', 'VerticalAlignment', 'bottom', 'fontsize', 20)
%title('Normalized Histogram of Number of Neutron Scatters in a 14x14 BCF-12 PSF Bundle', ...
%    'fontsize', 20);
xlabel('Scatters by a Single Neutron [#]', 'fontsize', 20);
ylabel('Fraction of Incident Neutrons [#]', 'fontsize', 20);
set(gca, 'box', 'on', 'fontsize', 20);
set(gcf(2), 'units', 'normalize', 'outerposition', [0 0 1 1]);

fprintf('\nHistogram of Scattering (Un-Normalized) Complete taking %6.2f sec...\n', toc)

%% Plot Scattering with Energy Deposition Events

figure(3)
subplot(2,2,1)
pcolor(fiber_bundle_t);
colormap(hot(128));
colorbar;
title('Total Energy Deposition', 'fontsize', 20);
xlabel('x-axis Fiber [#]', 'fontsize', 20);
ylabel('y-axis Fiber [#]', 'fontsize', 20);
set(gca, 'box', 'on', 'fontsize', 20, ...
    'xlim', [1 15], 'xtick', (2:2:14), 'xtickLabel', (2:2:14), ...
    'ylim', [1 15], 'ytick', (2:2:14), 'ytickLabel', (2:2:14));

subplot(2,2,2)
pcolor(fiber_bundle_s);
colormap(hot(128));
colorbar;
title('1st Scatter Energy Deposition', 'fontsize', 20);
xlabel('x-axis Fiber [#]', 'fontsize', 20);
ylabel('y-axis Fiber [#]', 'fontsize', 20);
set(gca, 'box', 'on', 'fontsize', 20, ...
    'xlim', [1 15], 'xtick', (2:2:14), 'xtickLabel', (2:2:14), ...
    'ylim', [1 15], 'ytick', (2:2:14), 'ytickLabel', (2:2:14));

subplot(2,2,3)
pcolor(fiber_bundle_d);
colormap(hot(128));
colorbar;
title('2nd Scatter Energy Deposition', 'fontsize', 20);
xlabel('x-axis Fiber [#]', 'fontsize', 20);
ylabel('y-axis Fiber [#]', 'fontsize', 20);
set(gca, 'box', 'on', 'fontsize', 20, ...
    'xlim', [1 15], 'xtick', (2:2:14), 'xtickLabel', (2:2:14), ...
    'ylim', [1 15], 'ytick', (2:2:14), 'ytickLabel', (2:2:14));

subplot(2,2,4)
pcolor(fiber_bundle_m+fiber_bundle_q);
colormap(hot(128));
colorbar;
title('3rd & 4th Scatters Energy Deposition', 'fontsize', 20);
xlabel('x-axis Fiber [#]', 'fontsize', 20);
ylabel('y-axis Fiber [#]', 'fontsize', 20);

```



```

set(gca,'box','on','fontsize',20,...
    'xlim',[1 15],'xtick',(2:2:14),'xtickLabel',(2:2:14),...
    'ylim',[1 15],'ytick',(2:2:14),'ytickLabel',(2:2:14));

set(gcf,'units','normalize','outerposition',[0 0 1 1]);

fprintf('\nFiber Bundle Cross-Section Scatter Heat Map Complete taking %6.2f sec...\n',toc)

%% Remove "Zero Rows" and "Zero Columns"

% Remove zero rows in "x_loc, y_loc, z_loc"
x_loc( all(~x_loc,2), : ) = [];
y_loc( all(~y_loc,2), : ) = [];
z_loc( all(~z_loc,2), : ) = [];

% Remove zero rows in "dist_btwn_scatt"
dist_btwn_scatt1( all(~dist_btwn_scatt1,2), : ) = [];
dist_btwn_scatt2( all(~dist_btwn_scatt2,2), : ) = [];
dist_btwn_scatt3( all(~dist_btwn_scatt3,2), : ) = [];
dist_btwn_scatt4( all(~dist_btwn_scatt4,2), : ) = [];

% Remove zero rows in "scatt_energy"
scatt_energy( all(~scatt_energy,2), : ) = [];
% Remove zero columns in "scatt_energy" <-- Just an Example if needed
%scatt_energy( :, all(~scatt_energy,1) ) = [];

% Remove zero rows in "remain_energy"
remain_energy1( all(~remain_energy1,2), : ) = [];
remain_energy2( all(~remain_energy2,2), : ) = [];
remain_energy3( all(~remain_energy3,2), : ) = [];
remain_energy4( all(~remain_energy4,2), : ) = [];

% Remove zero rows in "time"
time_s( all(~time_s,2), : ) = [];
time_d( all(~time_d,2), : ) = [];
time_m( all(~time_m,2), : ) = [];
time_q( all(~time_q,2), : ) = [];

% Remove zero rows in "velocity"
velocity_s( all(~velocity_s,2), : ) = [];
velocity_d( all(~velocity_d,2), : ) = [];
velocity_m( all(~velocity_m,2), : ) = [];
velocity_q( all(~velocity_q,2), : ) = [];

% Remove zero rows in "E_calc"
E_calc_s( all(~E_calc_s,2), : ) = [];
E_calc_d( all(~E_calc_d,2), : ) = [];
E_calc_m( all(~E_calc_m,2), : ) = [];
E_calc_q( all(~E_calc_q,2), : ) = [];

% Remove zero rows in "E_calc"
E_to_E_calc_s( all(~E_to_E_calc_s,2), : ) = [];
E_to_E_calc_d( all(~E_to_E_calc_d,2), : ) = [];
E_to_E_calc_m( all(~E_to_E_calc_m,2), : ) = [];
E_to_E_calc_q( all(~E_to_E_calc_q,2), : ) = [];

fprintf('\nFiber Bundle Removing Rows/Columns of Zeros Complete taking %6.2f sec...\n',toc)

%% Histogram of Distance (Lambda) Between Scatters

% Histogram of 1st to 2nd Scatter
figure(4)
%subplot(3,1,1)
hist(dist_btwn_scatt2(:,1),100)

```

```

hold on
%title('Histogram of Distance Between 1st to 2nd n-Scatter','fontsize',20);
xlabel('Distance, \lambda [cm]','fontsize',20);
ylabel('Counts [#]','fontsize',20);
set(gca,'box','on','fontsize',20);
set(gcf,'units','normalize','outerposition',[0 0 1 1]);
h = findobj(gca,'type','patch');
set(h,'facecolor','c','edgecolor','k')

% Histogram 2nd to 3rd Scatter
figure(5)
%subplot(3,1,2)
hist(dist_btwn_scatt3(:,1),100)
hold on
%title('Histogram of Distance Between 2nd to 3rd n-Scatter','fontsize',20);
xlabel('Distance, \lambda [cm]','fontsize',20);
ylabel('Counts [#]','fontsize',20);
set(gca,'box','on','fontsize',20);
set(gcf,'units','normalize','outerposition',[0 0 1 1]);
h = findobj(gca,'type','patch');
set(h,'facecolor','c')

% Histogram 3rd to 4th Scatter
figure(6)
%subplot(3,1,3)
hist(dist_btwn_scatt4(:,1),100)
hold on
%title('Histogram of Distance Between 3rd to 4th n-Scatter','fontsize',20);
xlabel('Distance, \lambda [cm]','fontsize',20);
ylabel('Counts [#]','fontsize',20);
set(gca,'box','on','fontsize',20);
set(gcf,'units','normalize','outerposition',[0 0 1 1]);
h = findobj(gca,'type','patch');
set(h,'facecolor','c','edgecolor','k')

%set(gcf,'units','normalize','outerposition',[0 0 1 1]);

%% Scatter Plot of Energy vs. Distance

% Scatter Plot of 1st to 2nd Scatter
figure(7)
%subplot(3,1,1)
scatter(dist_btwn_scatt2(:,1),remain_energy2(:,1),'b.')
hold on
%title('Energy and Distance Between 1st to 2nd n-Scatter','fontsize',20);
xlabel('Distance, \lambda [cm]','fontsize',20);
ylabel('Energy, E [keV]','fontsize',20);
set(gca,'box','on','fontsize',20);
set(gcf,'units','normalize','outerposition',[0 0 1 1]);

% Scatter Plot of 2nd to 3rd Scatter
figure(8)
%subplot(3,1,2)
scatter(dist_btwn_scatt3(:,1),remain_energy3(:,1),'b.')
hold on
%title('Energy and Distance Between 2nd to 3rd n-Scatter','fontsize',20);
xlabel('Distance, \lambda [cm]','fontsize',20);
ylabel('Energy, E [keV]','fontsize',20);
set(gca,'box','on','fontsize',20);
set(gcf,'units','normalize','outerposition',[0 0 1 1]);

% Scatter Plot of 3rd to 4th Scatter
figure(9)
%subplot(3,1,3)
scatter(dist_btwn_scatt4(:,1),remain_energy4(:,1),'b.')

```

```

hold on
%title('Energy and Distance Between 3rd to 4th n-Scatter','fontsize',20);
xlabel('Distance, \lambda [cm]','fontsize',20);
ylabel('Energy, E [keV]','fontsize',20);
set(gca,'box','on','fontsize',20);
set(gcf(9),'units','normalize','outerposition',[0 0 1 1]);

%set(gcf(7),'units','normalize','outerposition',[0 0 1 1]);

fprintf('\nFiber Bundle Histogram of Rho Complete taking %6.2f sec...\n',toc)

%% Energy and Distance (Lambda) Between Scatters Binning Contour Map

figure(10)
%subplot(2,1,1)
pcolor(dEdx_final);
hold on
colormap(hot(128));
colorbar;
title(colorbar,'Counts [#]','fontsize',20)
%title('Distribution of Energy and Distance Between All n-Scatters','fontsize',20);
xlabel('Distance, \lambda [mm]','fontsize',20);
ylabel('Energy, E [MeV]','fontsize',20);
set(gca,'box','on','fontsize',20,...
    'xlim',[1 51],'xtick',(5:5:50),'xtickLabel',(5:5:50),...
    'ylim',[1 26],'ytick',(5:5:25),'ytickLabel',(0.5:0.5:2.5));
set(gcf(10),'units','normalize','outerposition',[0 0 1 1]);

figure(11)
%subplot(2,1,2)
mesh(dEdx_final,'FaceColor','interp');
hold on
colormap(hot(128));
%colorbar;
%title(colorbar,'Counts [#]','fontsize',20)
%title('Distribution of Energy and Distance Between All n-Scatters');
xlabel('Distance, \lambda [mm]','fontsize',20);
ylabel('Energy, E [MeV]','fontsize',20);
zlabel('Counts [#]','fontsize',20);
set(gca,'fontsize',20,...
    'xlim',[1 51],'xtick',(5:5:50),'xtickLabel',(5:5:50),...
    'ylim',[1 26],'ytick',(5:5:25),'ytickLabel',(0.5:0.5:2.5));
% Uncomment one of the sets below (top = 1 mn, mid = 5 mn, bottom = 100 mn)
%set(gca,'zlim',[1 1000],'ztick',(0:250:1000),'ztickLabel',(0:250:1000));
%set(gca,'zlim',[1 10000],'ztick',(0:2500:10000),'ztickLabel',(0:2.5:10));
%set(gca,'zlim',[1 80000],'ztick',(0:20000:80000),'ztickLabel',(0:2:8));
set(gcf(11),'units','normalize','outerposition',[0 0 1 1]);

%set(gcf(10),'units','normalize','outerposition',[0 0 1 1]);

fprintf('\nFiber Bundle dE and dx Binning Complete taking %6.2f sec...\n',toc)

%% Comparison of GEANT4 Energy to MATLAB Energy (E:E_calc)

% Initialize
x = (0:1:2500);
y = x;

% Not really important (uncomment if really needed)

% figure(12)
% scatter(E_to_E_calc_s(:,1),E_to_E_calc_s(:,2),'b.')
% hold on
% %lsline;

```

```

% plot(x,y,'r-');
% title('Compare GEANT4 & MATLAB Energy for 0 to 1st n-Scatter','fontsize',20);
% xlabel('GEANT4 Energy','fontsize',20);
% ylabel('MATLAB Energy  $\left(\frac{mv^2}{2}\right)$ ','interpreter','latex','fontsize',20);
% set(gca,'box','on','fontsize',20,...
%     'xlim',[2499 2501],'xtick',(2499:0.5:2501),'xtickLabel',(2499:0.5:2501),...
%     'ylim',[1300 2500],'ytick',(1300:200:2500),'ytickLabel',(1300:200:2500));
% set(gcf(12),'units','normalize','outerposition',[0 0 1 1]);

%%
figure(13)
scatter(E_to_E_calc_d(:,1),E_to_E_calc_d(:,2),'b.')
hold on
lsline;
plot(x,y,'r-');
%title('Compare GEANT4 & MATLAB Energy for 1st to 2nd n-Scatter','fontsize',20);
xlabel('GEANT4 Energy','fontsize',20);
ylabel('MATLAB Energy  $\left(\frac{mv^2}{2}\right)$ ','interpreter','latex','fontsize',20);
set(gca,'box','on','fontsize',20,...
    'xlim',[0 2500],'xtick',(0:250:2500),'xtickLabel',(0:250:2500),...
    'ylim',[0 10000],'ytick',(0:1000:10000),'ytickLabel',(0:1000:10000));
set(gcf(13),'units','normalize','outerposition',[0 0 1 1]);

%%
figure(14)
scatter(E_to_E_calc_m(:,1),E_to_E_calc_m(:,2),'b.')
hold on
lsline;
plot(x,y,'r-');
%title('Compare GEANT4 & MATLAB Energy for 2nd to 3rd n-Scatter','fontsize',20);
xlabel('GEANT4 Energy','fontsize',20);
ylabel('MATLAB Energy  $\left(\frac{mv^2}{2}\right)$ ','interpreter','latex','fontsize',20);
set(gca,'box','on','fontsize',20,...
    'xlim',[0 2500],'xtick',(0:250:2500),'xtickLabel',(0:250:2500),...
    'ylim',[0 2500],'ytick',(0:250:2500),'ytickLabel',(0:250:2500));
set(gcf(14),'units','normalize','outerposition',[0 0 1 1]);

%%
figure(15)
scatter(E_to_E_calc_q(:,1),E_to_E_calc_q(:,2),'b.')
hold on
lsline;
plot(x,y,'r-');
%title('Compare GEANT4 & MATLAB Energy for 3rd to 4th n-Scatter','fontsize',20);
xlabel('GEANT4 Energy','fontsize',20);
ylabel('MATLAB Energy  $\left(\frac{mv^2}{2}\right)$ ','interpreter','latex','fontsize',20);
set(gca,'box','on','fontsize',20,...
    'xlim',[0 2500],'xtick',(0:250:2500),'xtickLabel',(0:250:2500),...
    'ylim',[0 10000],'ytick',(0:1000:10000),'ytickLabel',(0:1000:10000));
set(gcf(15),'units','normalize','outerposition',[0 0 1 1]);

fprintf('\nFiber Bundle Comparison of GEANT4 to MATLAB E Calculations Complete taking %6.2f sec...\n',toc)

%% Completion Output

% Stop Clock
elapsed_time = toc;
fprintf('\nFiber Bundle Neutron Scattering Simulation Post Processing took %6.2f [s]\n',elapsed_time)

```

Appendix B. Dual Ended Readout Oscilloscope Script

```
%% Data Input
clc;
clear all;
close all;

%% Connection Variables
visa_brand = 'tek'; % set to 'tek' for textronix scopes
visa_address = 'TCPIP::169.254.235.51::INSTR'; % use oscilloscope ip address
buffer = 10000 * 1024; %10000 KiB (Originally --> 2000 * 1024; %2000 KiB)

%% Configuration Variables
nFrames = 1000; % Number of waveforms to capture in FastFrame mode
nRecord = 1000; % Number of points in each individual waveform
nSets = 10; % How many datasets do you want to record?

%% Set scope timing properties
Time_Window = 100E-9; %width of time axis

%% Set properties for Channel #1
Ch1_status= 'ON' ;% Turns input for channel 1 on/off
Ch1_Termination = 1E6 ;% Sets input impedance in Ohms (use 50)
Ch1_VPos = 0.0; % from -5.0 to 5.0 (the divisions on vertical axis)
Ch1_HPos = 5; % from 0 to 100 (divisions across the horizontal axis)
Ch1_Offset = 0.0; % [V]
Ch1_Scale = 0.500; % [V]

%% Set properties for Channel #2
Ch2_status= 'OFF' ;% Turns input for channel 2 on/off
Ch2_Termination = 1E6 ;% Sets input impedance in Ohms (use 50)
Ch2_VPos = 0.0; % from -5.0 to 5.0 (the divisions on vertical axis)
Ch2_HPos = 5; % from 0 to 100 (divisions across the horizontal axis)
Ch2_Offset = 0.0; % [V]
Ch2_Scale = 0.500; % [V]

%% Set Trigger Settings
Trigger_Type='Edge' ; % Edge mode trigger
Trigger_Edge_Slope='Rise' ; % Falling slope
Trigger_Level=0.250 ; % Set trigger voltage level
Trigger_Mode='Normal' ; % Set trigger to Normal, apparently "Auto" is bad

%-----%
%                               End Data Input                               %
%-----%

%% Initialize Scope

%% Open Instrument
fclose('all'); % close any open files - useful if this script was interrupted and you want to use it again
dpo = visa(visa_brand, visa_address, 'InputBuffer', buffer, 'OutputBuffer', buffer); % create visa object,
no instrument driver required!
fopen(dpo); % open the instrument so that commands can be written to it

%fwrite(dpo,'*RST'); % Reset scope to factory defaults - reset any inadvertant scope setting changes.
fprintf('Scope reset to factory defaults.\n');

%% Configure Scope
%% Configuration Variables
fprintf('Configuring scope...');
frames = nFrames; % Number of waveforms to capture in FastFrame mode
record = nRecord; % Number of points in each individual waveform

%% Set properties for Channel #1
if strcmpi('ON',Ch1_status)
    Ch1VPos = Ch1_VPos; % from -5.0 to 5.0 (the divisions on vertical axis)
```

```

    Ch1HPos = Ch1_HPos; % from 0 to 100 (divisions across the horizontal axis)
    Ch1Offset = Ch1_Offset; % [V]
    Ch1Scale = Ch1_Scale; % [V]
    fwrite(dpo,['Ch1:Termination ' num2str(Ch1_Termination)]) % Sets input impedance in Ohms (use 50)
    fwrite(dpo,['Select:Ch1 ' Ch1_status]); % Turns input for channel 1 on
    fprintf(dpo,'ch1:Scale %i', Ch1Scale); % Sets vertical scale for channel 1
    fprintf(dpo,'Ch1:Position %i', Ch1VPos); % Aligns channel 1
    fprintf(dpo,'Ch1:Offset %i', Ch1Offset); % Sets channel 1 offset
end

%%%%% Set channel #2 Properties
if strcmpi('ON',Ch2_status)
    Ch2VPos = Ch2_VPos; % from -5.0 to 5.0 (the divisions on vertical axis)
    Ch2HPos = Ch2_HPos; % from 0 to 100 (divisions across the horizontal axis)
    Ch2Offset = Ch2_Offset; % [V]
    Ch2Scale = Ch2_Scale; % [V]
    fwrite(dpo,['Ch2:Termination ' num2str(Ch2_Termination)]) % Sets input impedance in Ohms (use 50)
    fwrite(dpo,['Select:Ch2 ' Ch2_status]); % Turns input for channel 2 on
    fprintf(dpo,'ch2:Scale %i', Ch2Scale); % Sets vertical scale for channel 2
    fprintf(dpo,'CH2:Position %i', Ch2VPos); % Aligns channel 2
    fprintf(dpo,'Ch2:Offset %i', Ch2Offset); % Sets channel 2 offset
end

%%%%% Set scope timing properties
TimeWindow = Time_Window; %width of time axis
TimeStep = TimeWindow/record; % Returns seconds per point
timearray = (1:1:record)*(TimeWindow/record)*1E9; % Array of time
fprintf(dpo,'Horizontal:Scale %i', TimeWindow); % Sets time scale
fprintf(dpo,'Horizontal:AcqLength %i', record); % Sets time resolution

%%%%%vSet Trigger Settings%%%%%

fwrite(dpo,['Trigger:A:Type ' Trigger_Type]); % Edge mode trigger
fwrite(dpo,['Trigger:A:Edge:Slope ' Trigger_Edge_Slope]); % Falling slope
fwrite(dpo,['Trigger:A:Level ' num2str(Trigger_Level)]); % Set trigger voltage level
fprintf(dpo,['Trigger:A:Mode ' Trigger_Mode]); % Set trigger to Normal, apparently "Auto" is bad

%%%%% Create variable with data channels
Data_Channels=[];
if strcmpi('on',Ch1_status)
    Data_Channels='Ch1';
end
if strcmpi('on',Ch2_status) && isempty(Data_Channels)
    Data_Channels='Ch2';
elseif strcmpi('on',Ch2_status)
    Data_Channels=[Data_Channels ' ', Ch2'];
end

%%%%% Write general commands to 0-scope
fwrite(dpo,'ACQ:STATE 0'); % Turn off acquisition before we change scope settings
fwrite(dpo,'HEAD 0'); % Turn off header information
fwrite(dpo,'ACQUIRE:MODE SAMPLE'); %Sets sampling mode to Sample mode
fwrite(dpo,'ACQUIRE:SAMPLINGMODE RT'); % Set Real Time sampling mode
fwrite(dpo,'HOR:MODE MANUAL'); % Enable manual adjustment of horizontal settings
fprintf(dpo,'HOR:MODE RECORD %i', record); % Set number of points on horizontal axis
fwrite(dpo,'HOR:FAST:STATE 1'); % Turn on FastFrame mode
fprintf(dpo,'HOR:FAST:COUNt %i', frames); % Set number of waveforms to capture per FastFrame acquisition
fprintf(dpo,'DATA:START 0'); % Sets the beginning of the individual waveform data to transfer (use 0)
fprintf(dpo,'DATA:STOP %i', record); % Sets the end of the individual waveform data to transfer
fwrite(dpo,'DATA:ENCDG SRIBINARY'); % Set data encoding to least significant byte first, signed integer
fprintf(dpo,'WFMInpre:ENCDG BINARY'); % Sets incoming data to binary format
fprintf(dpo,'WFMInpre:BN_FMT RI'); % Set signed integer
fprintf(dpo,'WFMInpre:BYT_OR LSB'); %Transfer Least Significant Bit first
fprintf(dpo,'WFMInpre:BYT_NR 1'); %Set 1 byte format = int8
fprintf(dpo,'WFMOutpre:BYT_NR 1'); %Set 1 byte format = int16
fprintf(dpo,'WFMOutpre:BN_FMT RI'); %Set signed integer

```

```

fprintf(dpo,'WFMOutpre:BYT_OR_LSB'); %Transfer Least Significant Bit first
fwrite(dpo,['DATA:SOURCE ' Data_Channels]); % Sets data source to Channel 1, 2, 3, 4

query(dpo,'WFMOutpre:YMult?');
if strcmpi('on', Ch1_status)
    Ch1YMult = str2double(query(dpo,'WFMOutpre:YMult?')); % Returns vertical scale factor
    Ch1Yoff = -Ch1VPos*Ch1Scale; % Calculate offset from zero
    fprintf(dpo,'Horizontal:Position %i', Ch1HPos); % Places signal at designated horizontal location
end
if strcmpi('on', Ch2_status)
    Ch2YMult = str2double(query(dpo,'WFMOutpre:YMult?')); % Returns vertical scale factor
    Ch2Yoff = -Ch2VPos*Ch2Scale; % Calculate offset from zero
    fprintf(dpo,'Horizontal:Position %i', Ch2HPos); % Places signal at designated horizontal location
end

fprintf('Done!\n');

%% ACQUIRE DATA

sets=nSets;
acq_time(sets) = zeros;
ask_time(sets) = zeros;
read_time(sets) = zeros;
save_time(sets) = zeros;
%tic % Start run time clock
if strcmpi('on',Ch1_status)
    Ch1 = zeros(nRecord,nFrames);
end
if strcmpi('on',Ch2_status)
    Ch2 = zeros(nRecord,nFrames);
end

for i=1:sets
    tic;
    fprintf(dpo,'Acquire:StopAfter Sequence'); % Stop acquiring after FastFrame acquisition
    fwrite(dpo,'ACQ:STATE 1'); % Turn on acquisition
    fprintf('Acquiring data set #%i.....', i);
    dpo.Timeout = 1000; % Adjust MATLAB timeout so it is longer than the acquisition duration
    query(dpo,'*opc?'); % Will return "1" when the acquisition is complete - used to sync curve command
    dpo.Timeout = 10; % Decrease timeout time now that the acquisition is done
    fprintf('Done!\n');
    acq_time(i) = toc;

    fprintf(' Asking for waveforms...');
    fwrite(dpo, 'curve?'); % Ask for waveforms - waveform preamble and binary data will be stored in memory
    fprintf('Done!\n');
    ask_time(i) = toc - acq_time(i);

    fprintf(' Reading waveforms...');
    fread(dpo,1); % Read and throw away first character in preamble - should be a "#"
    bytes = str2double(char((fread(dpo,1)))); % Read and store the number of bytes in memory
    fread(dpo, bytes); % Read and throw away the appropriate number of characters remaining in the preamble
    header = (1+1+bytes);
    if strcmpi('on',Ch1_status)
        raw1 = fread(dpo, record*frames,'int8'); % Read and store all of the waveform data - no separation
        between individual waveforms
    end
    if strcmpi('on',Ch2_status)
        raw2 = fread(dpo, record*frames,'int8'); % Read and store all of the waveform data - no separation
        between individual waveforms
    end
    fprintf('Done!\n');
    fread(dpo,1); % Read and throw away the termination character that Curve? adds
    read_time(i) = toc - ask_time(i);
end

```

```

start = 1;
stop = nRecord;
for j=1:frames %(Originally j=1:record)
    if strcmpi('on',Ch1_status)
        Ch1(1:record, j) = raw1(start:stop);
    end
    if strcmpi('on',Ch2_status)
        Ch2(1:record, j) = raw2(start:stop);
    end
    start = stop+1;
    stop = start+record-1;
end
if strcmpi('on',Ch1_status)
    Ch1 = (Ch1YMult*Ch1+Ch1Yoff); % Apply scale and offset to match the physical voltage values
    savename = ['Ch1_' num2str(i) '.mat']; % name the current batch of waveforms
    save(savename,'Ch1') % save the current batch of waveforms
end
if strcmpi('on',Ch2_status)
    Ch2 = (Ch2YMult*Ch2+Ch2Yoff); % Apply scale and offset to match the physical voltage values
    savename = ['Ch2_' num2str(i) '.mat']; % name the current batch of waveforms
    save(savename,'Ch2') % save the current batch of waveforms
end
save_time(i) = toc - read_time(i);
end
fprintf('***** %i waveforms recorded! *****\n', sets*frames);
timeElapsed = toc % End run time clock

fprintf('\nacq_time = %4.4f [sec]',mean(acq_time))
fprintf('\nask_time = %4.4f [sec]',mean(ask_time))
fprintf('\nread_time = %4.4f [sec]',mean(read_time))
fprintf('\nsave_time = %4.4f [sec]\n',mean(save_time))

fclose(dpo);

```


Appendix C. Hamamatsu H3378-50 PMT Specifications

Two H3378-50s photomultiplier tubes were used until one was damaged beyond repair. The advantage of these this PMT over the SiPMTs (MPPCs) is that they are better suited for applications requiring low-noise, high-sensitivity detection of light that is not collimated precisely. Tables 13, 14, and 15 provide the H3378-50 PMT's assembly, cathode, and anode specifications, respectively. Figure 42 provides a depiction of a typical Hamamatsu cylindrical PMT module.

Table 13. Hamamatsu photomultiplier tube H3378-50 assembly characteristics. The photocathode material for this PMT is bialkali (Sb-Rb-Cs or Sb-K-Cs) and the window material is quartz (synthetic silica). This information was reproduced with permission from Hamamatsu [20].

Dia. (mm)	Gain	Supply Voltage (V)	Max Supply Voltage (V)	Divider Current (mA)	Dim. (mm)
51	2.5×10^6	3000	3500	0.52	$\phi 60 \times 200$

Table 14. Hamamatsu photomultiplier tube H3378-50 cathode characteristics. This information was reproduced with permission from Hamamatsu [21].

Luminous ($\mu\text{A}/\text{lm}$)	Blue Sensitivity Index (CS 5-58)	Radiant (mA/W)
80	10.0	80



Figure 42. A typical Hamamatsu cylindrical PMT module which closely resembles the H3378-50 PMT. The figure is reproduced with permission from Hamamatsu [20].

Table 15. Hamamatsu photomultiplier tube H3378-50 anode characteristics. This information was reproduced with permission from Hamamatsu [21].

Luminous (A/lm)	Gain	Dark Current		Time Response			Pulse Linearity	
		Typ. (nA)	Max (nA)	Rise Time (ns)	Transit Time (ns)	Transit Time Spread (ns)	2% (mA)	5% (mA)
200	2.5×10^6	100	800	0.7	16	0.37	100	150

Appendix D. Scintillation Yield Script

```
%Written by 2d Lt Paul A. Clement
%27 February 2012
%Photon Parametric Study

close all
clear all
clc

% Start Clock
tic;

fprintf('\nParametric Study Has Started...\n')

%% Definitions

fiber_length = 1;      % [cm] length of fiber
travel = 30/2;         % [cm] distance traveled to photosensor (hits middle)
E_n = (0:1:2.5E3);     % [keV] Neutron Energy
photon_gen = 8;        % [Photons/keV]
attn_length = 270;     % [cm]
quench = 1.0;          % [Unitless]
trap_eff = 0.0344;     % [Unitless]
quan_eff_25C = 0.25;   % [Unitless]
quan_eff_50C = 0.48;   % [Unitless]
quan_eff_100C = 0.74;  % [Unitless]

%% Program

photon_25C = 0.5*E_n.*photon_gen*exp(-travel/attn_length)*quench*trap_eff*quan_eff_25C; % [Photons]

photon_50C = 0.5*E_n.*photon_gen*exp(-travel/attn_length)*quench*trap_eff*quan_eff_50C; % [Photons]

photon_100C = 0.5*E_n.*photon_gen*exp(-travel/attn_length)*quench*trap_eff*quan_eff_100C; % [Photons]

figure(1)
plot(E_n,photon_25C,'r-','linewidth',3)
hold on
plot(E_n,photon_50C,'b-','linewidth',3)
plot(E_n,photon_100C,'g-','linewidth',3)
xlabel('Energy Deposited by a Neutron, E_n [keV]','fontsize',20);
ylabel('Photons Collected a Single SiPM MPPC [#]','fontsize',20);
%title('Photons Collected After Incident Neutron Interaction','fontsize',20);
legend('Hamamatsu S10362-11-025C','Hamamatsu S10362-11-050C',...
       'Hamamatsu S10362-11-100C','fontsize',20,'location','northwest');
set(gca,'box','on','xgrid','on','ygrid','on','fontsize',20);
set(figure(1),'units','normalize','outerposition',[0 0 1 1]);

%% Final Output

% Stop Clock
elapsed_time = toc;
fprintf('\nParametric Study took %1.3f [s]\n',elapsed_time)
```

Appendix E. Spatial and Timing Resolution Uncertainty Script

```
% Written by Maj Ben Kowash
% Revised and Studies by 2d Lt Paul A. Clement
% 27 February 2012
% TOF Parametric Study

close all
clear all
clc

% Start Clock
tic;

fprintf('\nTOF Parametric Study Has Started...\n')

%% Definitions

m_n = 1.008665*931.494*1.602E-13/(3E8)^2; % [kg] Mass of a Neutron

% Conversions
MeV_per_J = (1/1.602E-13); % (1 [MeV] / 1.602E-13 [J])
ns_per_s = (1E9/1); % (1E9 [ns] / 1 [s])
ps_per_s = (1E12/1); % (1E12 [ps] / 1 [s])
cm_per_m = (1E2/1); % (1E2 [cm] / 1 [m])

dz = 0.01:0.01:1; % [m]
dt = 0.1E-9:0.1E-9:10E-9; % [sec]

sigma_z = 0.001; % [m] Uncertainty in Position
sigma_t = 0.1E-9; % [sec] Uncertainty in Time

% Initialize
vel(length(dz),length(dt)) = zeros;
sigma_E(length(dz),length(dt)) = zeros;
E(length(dz),length(dt)) = zeros;

for i=1:length(dz)

    for j=1:length(dt)

        % Velocity (vel)
        vel(i,j) = dz(i)./dt(j); % [m/s]

        % Energy Uncertainty (sigma_E)
        % (sigma_E)^2 = (dE/dz)^2*(sigma_z)^2 + (dE/dt)^2*(sigma_t)^2
        % (dE/dz) = m_n*(dz/dt^2)
        % (dE/dt) = -m_n*(dz^2/dt^3)
        sigma_E(i,j) = sqrt((-m_n*dz(i)/dt(j)^2)^2 * sigma_z^2 ...
            + (m_n*dz(i)^2/dt(j)^3)^2 * sigma_t^2);
        sigma_E(i,j) = sigma_E(i,j).*MeV_per_J; % [MeV]

        % Energy (E)
        E(i,j) = 0.5*m_n*(vel(i,j)^2).*MeV_per_J; % [MeV]

    end

end

rel_error = sigma_E./E*100; % [%]

%% Plotting of Energy and Energy Uncertainty
```

```

% Define Energy Plot Bounds
E_dz_min = 1; % [cm]
E_dz_max = 22; % [cm]
E_dz_ss = E_dz_max/11; % [cm] step size for Energy y-axis
E_dt_min = 10; % [ns] (x10)
E_dt_max = 100; % [ns] (x10)
E_dt_ss = E_dt_max/10; % [ns] (x10) step size for Energy x-axis

% Define Energy Uncertainty Bounds
sigma_E_dz_min = E_dz_min; % [cm]
sigma_E_dz_max = E_dz_max; % [cm]
sigma_E_dz_ss = sigma_E_dz_max/11; % [cm] step size for Energy Uncertainty x-axis
sigma_E_dt_min = E_dt_min; % [ns] (x10)
sigma_E_dt_max = E_dt_max; % [ns] (x10)
sigma_E_dt_ss = sigma_E_dt_max/10; % [ns] (x10) step size for Energy Uncertainty x-axis

figure(1)

% Energy
subplot(2,1,1)
[~,h] = contour(dt(:,E_dt_min:E_dt_max)*ns_per_s,...
    dz(:,E_dz_min:E_dz_max)*cm_per_m,...
    E(E_dz_min:E_dz_max,E_dt_min:E_dt_max),100); %<-- uncomment for contour
%pcolor(dt(:,E_dt_min:E_dt_max)*ns_per_s,...
%    dz(:,E_dz_min:E_dz_max)*cm_per_m,...
%    E(E_dz_min:E_dz_max,E_dt_min:E_dt_max) %<-- uncomment for pcolor
%mesh(dt(:,E_dt_min:E_dt_max)*ns_per_s,...
%    dz(:,E_dz_min:E_dz_max)*cm_per_m,...
%    E(E_dz_min:E_dz_max,E_dt_min:E_dt_max),'facecolor','interp') %<-- uncomment for mesh
set(gca,'fontsize',20,...
    'xlim',[E_dt_min/10 E_dt_max/10],'xtick',(E_dt_min/10:E_dt_ss/10:E_dt_max/10),...
    'xticklabel',(E_dt_min/10:E_dt_ss/10:E_dt_max/10),...
    'ylim',[E_dz_min E_dz_max],'ytick',(E_dz_min:E_dz_ss:E_dz_max),...
    'yticklabel',(E_dz_min:E_dz_ss:E_dz_max),...
    'zlim',[0 3],'ztick',(0:0.1:3),'zticklabel',(0:0.2:3))
    %^--- , 'zlim',(0 max(E(:)))
%set(h,'showtext','on','levellistmode','manual','textstep',get(h,'levelstep')*2)
title('Energy','fontsize',20)
xlabel('Time, dt [ns]','fontsize',20)
ylabel('Position, dz [cm]','fontsize',20)
zlabel('Energy, E [MeV]','fontsize',20)
colormap('hot')
title(colorbar,'Energy [MeV]','fontsize',20)

% Energy Uncertainty
subplot(2,1,2)
[~,h] = contour(dt(:,sigma_E_dt_min:sigma_E_dt_max)*ns_per_s,...
    dz(:,sigma_E_dz_min:sigma_E_dz_max)*cm_per_m,...
    sigma_E(sigma_E_dz_min:sigma_E_dz_max,sigma_E_dt_min:sigma_E_dt_max),50);
%<-- uncomment for contour
%pcolor(dt(:,E_dt_min:E_dt_max)*ns_per_s,...
%    dz(:,E_dz_min:E_dz_max)*cm_per_m,...
%    sigma_E(E_dt_min:E_dt_max,E_dz_min:E_dz_max)) %<-- uncomment for pcolor
%mesh(dt(:,E_dt_min:E_dt_max)*ns_per_s,...
%    dz(:,E_dz_min:E_dz_max)*cm_per_m,...
%    sigma_E(E_dt_min:E_dt_max,E_dz_min:E_dz_max),'facecolor','interp') %<-- uncomment for mesh
set(gca,'fontsize',20,...
    'xlim',[sigma_E_dt_min/10 sigma_E_dt_max/10],...
    'xtick',(sigma_E_dt_min/10:sigma_E_dt_ss/10:sigma_E_dt_max/10),...
    'xticklabel',(sigma_E_dt_min/10:sigma_E_dt_ss/10:sigma_E_dt_max/10),...
    'ylim',[sigma_E_dz_min sigma_E_dz_max],...
    'ytick',(sigma_E_dz_min:sigma_E_dz_ss:sigma_E_dz_max),...
    'yticklabel',(sigma_E_dz_min:sigma_E_dz_ss:sigma_E_dz_max),...
    'zlim',[0 3],'ztick',(0:0.1:3),'zticklabel',(0:0.2:3))

```

```

%---- , 'zlim', (0 max(E(:)))
%set(h, 'showtext', 'on', 'textstep', get(h, 'levelstep')*10)
title('Energy Uncertainty (\sigma_E)', 'fontsize', 20)
xlabel('Time, dt [ns]', 'fontsize', 20)
ylabel('Position, dz [cm]', 'fontsize', 20)
zlabel('Energy Uncertainty, \sigma_E [MeV]', 'fontsize', 20)
colormap('hot')
colorbar
title(colorbar, 'Energy [MeV]', 'fontsize', 20)

set(gcf, 'units', 'normalize', 'outerposition', [0 0 1 1])

figure(2)
[~,h] = contour(dt(:, sigma_E_dt_min:sigma_E_dt_max)*ns_per_s,...
    dz(:, sigma_E_dz_min:sigma_E_dz_max)*cm_per_m,...
    rel_error(sigma_E_dz_min:sigma_E_dz_max, sigma_E_dt_min:sigma_E_dt_max), 25);
%-- uncomment for contour
%pcolor(dt(:, E_dt_min:E_dt_max)*ns_per_s,...
%    dz(:, E_dz_min:E_dz_max)*cm_per_m),...
%    rel_error(E_dt_min:E_dt_max, E_dz_min:E_dz_max)) %<-- uncomment for pcolor
%mesh(dt(:, E_dt_min:E_dt_max)*ns_per_s,...
%    dz(:, E_dz_min:E_dz_max)*cm_per_m,...
%    rel_error(E_dt_min:E_dt_max, E_dz_min:E_dz_max), 'facecolor', 'interp') %<-- uncomment for mesh
set(gca, 'fontsize', 20,...
    'xlim', [sigma_E_dt_min/10 sigma_E_dt_max/10],...
    'xtick', (sigma_E_dt_min/10:sigma_E_dt_max/10),...
    'xticklabel', (sigma_E_dt_min/10:sigma_E_dt_max/10),...
    'ylim', [sigma_E_dz_min sigma_E_dz_max],...
    'ytick', (sigma_E_dz_min:sigma_E_dz_max),...
    'yticklabel', (sigma_E_dz_min:sigma_E_dz_max),...
    'zlim', [0 3], 'ztick', (0:0.1:3), 'zticklabel', (0:0.2:3))
%---- , 'zlim', (0 max(E(:)))
set(h, 'showtext', 'on', 'textstep', get(h, 'levelstep')*100)
%title('$\left(\frac{\sigma_E}{E}\right)\cdot 100$', 'interpreter', 'latex', 'fontsize', 20)
xlabel('Time, dt [ns]', 'fontsize', 20)
ylabel('Position, dz [cm]', 'fontsize', 20)
zlabel('Energy Uncertainty, \sigma_E [MeV]', 'fontsize', 20)
colormap('hot')
colorbar
title(colorbar, 'Percent Uncertainty [%]', 'fontsize', 20)

set(gcf, 'units', 'normalize', 'outerposition', [0 0 1 1])

%%

E_2500keV = E;
E_2500keV(E_2500keV > 3.5) = 3.5;

sigma_E_2500keV = sigma_E;
sigma_E_2500keV(sigma_E_2500keV > 0.1) = 0.1;

rel_error_2500keV = sigma_E_2500keV./E_2500keV*100; % [%]

figure(3)

% Energy
subplot(2,1,1)
[~,h] = contour(dt(:, E_dt_min:E_dt_max)*ns_per_s,...
    dz(:, E_dz_min:E_dz_max)*cm_per_m,...
    E_2500keV(E_dz_min:E_dz_max, E_dt_min:E_dt_max), 50); %<-- uncomment for contour
%pcolor(dt(:, E_dt_min:E_dt_max)*ns_per_s,...
%    dz(:, E_dz_min:E_dz_max)*cm_per_m,...
%    E_2500keV(E_dz_min:E_dz_max, E_dt_min:E_dt_max)) %<-- uncomment for pcolor
%mesh(dt(:, E_dt_min:E_dt_max)*ns_per_s,...
%    dz(:, E_dz_min:E_dz_max)*cm_per_m,...

```

```

% E_2500keV(E_dz_min:E_dz_max,E_dt_min:E_dt_max),'facecolor','interp') %<-- uncomment for mesh
set(gca,'fontsize',20,...
    'xlim',[E_dt_min/10 E_dt_max/10],'xtick',(E_dt_min/10:E_dt_ss/10:E_dt_max/10),...
    'xticklabel',(E_dt_min/10:E_dt_ss/10:E_dt_max/10),...
    'ylim',[E_dz_min E_dz_max],'ytick',(E_dz_min:E_dz_ss:E_dz_max),...
    'yticklabel',(E_dz_min:E_dz_ss:E_dz_max),...
    'zlim',[0 3],'ztick',(0:0.1:3),'zticklabel',(0:0.2:3))
    %^--- , 'zlim',(0 max(E(:)))
%set(h,'showtext','on','levellistmode','manual','textstep',get(h,'levelstep')*2)
title('Energy','fontsize',20)
xlabel('Time, dt [ns]','fontsize',20)
ylabel('Position, dz [cm]','fontsize',20)
zlabel('Energy, E [MeV]','fontsize',20)
colormap('hot')
title(colorbar,'Energy [MeV]','fontsize',20)

% Energy Uncertainty
subplot(2,1,2)
[~,h] = contour(dt(:,sigma_E_dt_min:sigma_E_dt_max)*ns_per_s,...
    dz(:,sigma_E_dz_min:sigma_E_dz_max)*cm_per_m,...
    sigma_E_2500keV(sigma_E_dz_min:sigma_E_dz_max,sigma_E_dt_min:sigma_E_dt_max),50);
% ^--- uncomment for contour
%pcolor(dt(:,E_dt_min:E_dt_max)*ns_per_s,...
%    dz(:,E_dz_min:E_dz_max*cm_per_m),...
%    sigma_E_2500keV(E_dt_min:E_dt_max,E_dz_min:E_dz_max)) %<-- uncomment for pcolor
%mesh(dt(:,E_dt_min:E_dt_max)*ns_per_s,...
%    dz(:,E_dz_min:E_dz_max)*cm_per_m,...
%    sigma_E_2500keV(E_dt_min:E_dt_max,E_dz_min:E_dz_max),'facecolor','interp') %<-- uncomment for mesh
set(gca,'fontsize',20,...
    'xlim',[sigma_E_dt_min/10 sigma_E_dt_max/10],...
    'xtick',(sigma_E_dt_min/10:sigma_E_dt_ss/10:sigma_E_dt_max/10),...
    'xticklabel',(sigma_E_dt_min/10:sigma_E_dt_ss/10:sigma_E_dt_max/10),...
    'ylim',[sigma_E_dz_min sigma_E_dz_max],...
    'ytick',(sigma_E_dz_min:sigma_E_dz_ss:sigma_E_dz_max),...
    'yticklabel',(sigma_E_dz_min:sigma_E_dz_ss:sigma_E_dz_max),...
    'zlim',[0 3],'ztick',(0:0.1:3),'zticklabel',(0:0.2:3))
    %^--- , 'zlim',(0 max(E(:)))
%set(h,'showtext','on','textstep',get(h,'levelstep')*10)
title('Energy Uncertainty (\sigma_E)','fontsize',20)
xlabel('Time, dt [ns]','fontsize',20)
ylabel('Position, dz [cm]','fontsize',20)
zlabel('Energy Uncertainty, \sigma_E [MeV]','fontsize',20)
colormap('hot')
colorbar
title(colorbar,'Energy [MeV]','fontsize',20)

set(figure(3),'units','normalize','outerposition',[0 0 1 1])

figure(4)
[~,h] = contour(dt(:,sigma_E_dt_min:sigma_E_dt_max)*ns_per_s,...
    dz(:,sigma_E_dz_min:sigma_E_dz_max)*cm_per_m,...
    rel_error_2500keV(sigma_E_dz_min:sigma_E_dz_max,sigma_E_dt_min:sigma_E_dt_max),25);
% ^--- uncomment for contour
%pcolor(dt(:,E_dt_min:E_dt_max)*ns_per_s,...
%    dz(:,E_dz_min:E_dz_max*cm_per_m),...
%    rel_error(E_dt_min:E_dt_max,E_dz_min:E_dz_max)) %<-- uncomment for pcolor
%mesh(dt(:,E_dt_min:E_dt_max)*ns_per_s,...
%    dz(:,E_dz_min:E_dz_max)*cm_per_m,...
%    rel_error_2500keV(E_dt_min:E_dt_max,E_dz_min:E_dz_max),'facecolor','interp') %<-- uncomment for mesh
set(gca,'fontsize',20,...
    'xlim',[sigma_E_dt_min/10 sigma_E_dt_max/10],...
    'xtick',(sigma_E_dt_min/10:sigma_E_dt_ss/10:sigma_E_dt_max/10),...
    'xticklabel',(sigma_E_dt_min/10:sigma_E_dt_ss/10:sigma_E_dt_max/10),...
    'ylim',[sigma_E_dz_min sigma_E_dz_max],...
    'ytick',(sigma_E_dz_min:sigma_E_dz_ss:sigma_E_dz_max),...

```

```

        'yticklabel',(sigma_E_dz_min:sigma_E_dz_ss:sigma_E_dz_max),...
        'zlim',[0 3],'ztick',(0:0.1:3),'zticklabel',(0:0.2:3))
        %^--- , 'zlim',(0 max(E(:)))
set(h,'showtext','on','textstep',get(h,'levelstep')*100)
%title('$\left(\frac{\sigma_E}{E}\right)\cdot 100$', 'interpreter','latex','fontsize',20)
xlabel('Time, dt [ns]','fontsize',20)
ylabel('Position, dz [cm]','fontsize',20)
zlabel('Energy Uncertainty, \sigma_E [MeV]','fontsize',20)
colormap('hot')
colorbar
title(colorbar,'Percent Uncertainty [%]','fontsize',20)

set(figure(4),'units','normalize','outerposition',[0 0 1 1])

%% Final Output

% Stop Clock
elapsed_time = toc;
fprintf('\nTOF Parametric Study took %1.3f [s]\n',elapsed_time)

```


Appendix F. Peak Counting (Dark Count) Script

```
%% Post Processing Peak Counting

close all
clear all
clc

% Start clock
tic;

% File information
total_files = 1950;
max_of_pulse = [zeros];
n = 1000;
peak_count = 0;

% Corrections
voltage_shift = 0.00;

% e_charge = 1.602*10^-19;
% SiPM_gain = 2.75*10^5;
% preamp_gain = 100;
%
% Q = e_charge*SiPM_gain*preamp_gain;
% C = 110*10^-12;
%
% photon_pulse_height = Q/C;

photon_pulse_height = 0.100; % [V]

% Loop to load all sets of waveforms
for i = 1:total_files

    % Load each waveform set
    Waveforms = load(['J:\Masters Thesis\New Experiments\Aluminum Box\Ch1\Ch1_' num2str(i) '.mat']);

    % Plot Waveforms
    % figure(1)
    % hold on
    % plot(Waveforms.Ch1(:,1000)+voltage_shift)
    % title('Waveforms')
    % xlabel('Channel # [1 ns/pt]')
    % ylabel('Voltage [V]')

    %SGWaveforms = sgolayfilt(Waveforms.Ch1(:,x)+voltage_shift,3,11);

    % Plot SGWaveforms
    % figure(2)
    % hold on
    % plot(SGWaveforms)
    % title('SGWaveforms')
    % xlabel('Channel # [1 ns/pt]')
    % ylabel('Voltage [V]')

    for j = 1:1000
        [zmax,imax,zmin,imin]= extrema(Waveforms.Ch1(:,j)+voltage_shift);
        m = 1;
        amp = 0;
        amplitude(40,2E6) = zeros;

        for k = 1:length(zmax)
            if zmax(k,1) > photon_pulse_height
                if imax(1,1) < imin(1,1)
                    if k > 1
```

```

        amp(m,1) = zmax(k,1) - zmin(k-1,1);
    end
else
    amp(m,1) = zmax(k,1) - zmin(k,1);
end
if amp(m,1) > photon_pulse_height
    amplitude(m,(j+(i*1000)-1000)) = amp(m,1);
    peak_count = peak_count + floor(amp(m,1)/photon_pulse_height);
end
m = m + 1;
end
end
end

% figure(1)
% plot(imax,zmax,'ro')
% plot(imin,zmin,'go')

% figure(2)
% plot(imax,zmax,'ro')
% plot(imin,zmin,'go')

% Percentage complete
fprintf('\nLoading Waveforms is %4.2f %% complete',i/total_files*100)
fprintf('\nTime taken thus far is %4.1f [sec]',toc)
fprintf('\nTime remaining is ~ %4.1f [sec] or ~%4.1f [min]\n', ...
        toc/(i/total_files)-toc,(toc/(i/total_files)-toc)/60)
end

%% Final Output

% Plot histogram of Waveforms
figure(3)
hold on
hist(amplitude(:),1000)
title('Histogram of Pulse Height at Trigger Point Ch1 Background')
xlabel('Voltage [V]')
ylabel('Counts')

dark_count = peak_count/(20*total_files*1000)*10^(6);

fprintf('\nThere are %1.0f dark counts\n',dark_count)

% Stop clock
fprintf('\nPost processing took %1.1f seconds\n',toc)

```

Appendix G. Fast Digital Data Acquisition Parameters

The fast digital data acquisition parameters for 1 and 10 waveforms per set is found in Table 16. The fast digital data acquisition parameters for 100 and 1000 waveforms per set is found in Table 17. In Tables 16 and 17, the first column provides the frequency as it is increased from 0.1 to 5000 kHz. The next four columns are the four separate functions within a single collection run, which are comprised of the acquire, ask, read, and save times. The oscilloscope pulse count is the number of pulses collected by the digital oscilloscope during the run. This is the same as the number of collected pulses, (N_{CP}) located in Tables 11 and 12. The oscilloscope pulse count column is calculated using Equation 34, where the number of sets (N_S) is one. The total pulse count column is the number of possible pulses, which is similar to the number of possible pulses, (N_{PP}) located in Tables 11 and 12. Equation 35 is used to calculate the total pulse counts, with one small difference. The difference is the total pulse count column is calculated using only the acquire time, instead of the entire collection time (i.e. all four function times added together). The fraction term is the same as the fraction term in Tables 11 and 12 and is calculated using Equation 36. The number of collected pulses (numerator) and number of possible pulses (denominator) are substituted with the oscilloscope pulse count and total pulse count, respectively.

Table 16. Fast digital data acquisition parameters. (*Top*) 1 waveform per set. (*Bottom*) 10 waveforms per set.

Frequency f (kHz)	Acquire Time (sec)	Ask Time (sec)	Read Time (sec)	Save Time (sec)	File Size (KB)	Oscilloscope Pulse Count (#)	Total Pulse Count (#)	Fraction F (#)
0.1	0.1843	0.0125	0.2988	0.0212	0.729	1	18	0.05556
0.5	0.1779	0.0067	0.2677	0.0152	0.750	1	88	0.01136
1	0.1504	0.0111	0.2406	0.0197	0.721	1	150	0.00667
5	0.1587	0.0125	0.2601	0.0239	0.732	1	793	0.00126
10	0.1779	0.0132	0.2957	0.0220	0.721	1	1779	0.00056
50	0.1842	0.0078	0.2994	0.0167	0.732	1	9210	0.00011
100	0.1708	0.0127	0.2893	0.0216	0.722	1	17080	5.85E-5
500	0.1835	0.0127	0.3054	0.0216	0.725	1	91750	1.09E-5
1000	0.1750	0.0112	0.2827	0.0216	0.730	1	175000	5.71E-6
2500	0.1390	0.0075	0.2719	0.0163	0.875	3	347500	8.63E-6
5000	0.1407	0.0073	0.2762	0.0161	0.979	5	703500	7.11E-6

Frequency f (kHz)	Acquire Time (sec)	Ask Time (sec)	Read Time (sec)	Save Time (sec)	File Size (KB)	Oscilloscope Pulse Count (#)	Total Pulse Count (#)	Fraction F (#)
0.1	0.2862	0.0075	0.4575	0.0200	5.928	10	28	0.35714
0.5	0.2070	0.0081	0.3492	0.0335	5.853	10	103	0.09709
1	0.2508	0.0146	0.3664	0.0268	5.880	10	250	0.04000
5	0.1857	0.0120	0.3736	0.0272	5.804	10	928	0.01078
10	0.2371	0.0076	0.3517	0.0223	5.876	10	2371	0.00422
50	0.1797	0.0122	0.3250	0.0247	5.822	10	8985	0.00111
100	0.1684	0.0123	0.3330	0.0246	5.842	10	16840	0.00059
500	0.1768	0.0128	0.3942	0.0254	5.876	10	88400	0.00011
1000	0.2337	0.0073	0.3308	0.0198	5.838	10	233700	4.28E-5
2500	0.2022	0.0077	0.4030	0.0201	7.343	30	505500	5.93E-5
5000	0.1762	0.0177	0.3268	0.0300	8.114	50	881000	5.68E-5

Table 17. Fast digital data acquisition parameters. (*Top*) 100 waveforms per set. (*Bottom*) 1000 waveforms per set.

Frequency f (kHz)	Acquire Time (sec)	Ask Time (sec)	Read Time (sec)	Save Time (sec)	File Size (KB)	Oscilloscope Pulse Count (#)	Total Pulse Count (#)	Fraction F (#)
0.1	1.2702	0.0232	1.4713	0.0694	57.617	100	127	0.78740
0.5	0.4563	0.0110	0.7937	0.0547	57.339	100	228	0.43860
1	0.3443	0.0113	0.4856	0.0555	57.586	100	344	0.29070
5	0.2977	0.0122	0.4985	0.0672	57.558	100	1488	0.06720
10	0.3030	0.0112	0.4093	0.0577	57.538	100	3030	0.03300
50	0.2419	0.0086	0.4025	0.0525	57.499	100	12095	0.00827
100	0.2688	0.0123	0.3808	0.0561	57.717	100	26880	0.00372
500	0.2513	0.0114	0.3911	0.0654	57.486	100	125650	0.00080
1000	0.2727	0.0117	0.4247	0.0570	57.778	100	272700	0.00037
2500	0.2530	0.0115	0.3782	0.0565	71.220	300	632500	0.00047
5000	0.2610	0.0117	0.4083	0.0627	80.287	500	1305000	0.00038

Frequency f (kHz)	Acquire Time (sec)	Ask Time (sec)	Read Time (sec)	Save Time (sec)	File Size (KB)	Oscilloscope Pulse Count (#)	Total Pulse Count (#)	Fraction F (#)
0.1	11.0781	0.0226	11.4995	0.3795	574.040	1000	1107	0.90334
0.5	3.0764	0.0208	3.4758	0.3975	576.399	1000	1538	0.65020
1	2.0797	0.0150	2.4791	0.4494	575.978	1000	2079	0.48100
5	1.2840	0.0161	1.5476	0.3742	576.397	1000	6420	0.15576
10	1.1948	0.0258	1.4497	0.5544	574.949	1000	11948	0.08370
50	1.1315	0.0152	1.5411	0.4035	573.130	1000	56575	0.01768
100	1.1043	0.0284	1.3832	0.3908	574.762	1000	110430	0.00906
500	1.0702	0.0146	1.4813	0.3928	573.663	1000	535100	0.00187
1000	1.1087	1.0149	1.5274	0.3894	578.184	1000	1108700	0.00090
2500	1.1021	0.0162	1.5014	0.4790	712.504	3000	2755250	0.00109
5000	1.0956	0.0226	1.4857	0.4184	801.497	5000	5478000	0.00091

Bibliography

1. Wikipedia, "Scintillator — wikipedia, the free encyclopedia," 2013, online; Accessed 17-April-2013. [Online]. Available: <http://en.wikipedia.org/w/index.php?title=Scintillator&oldid=549032118>
2. J. S. Gearhart, "Investigation of BCF-12 Plastic Scintillating Coherent Fiber Bundle Timing Properties," 2012. [Online]. Available: www.dtic.mil/dtic/tr/fulltext/u2/a558322.pdf
3. B. S. Jones, "Investigation of yag:ce scintillating fiber properties using silicon photomultipliers," 2011. [Online]. Available: <http://www.dtic.mil/dtic/tr/fulltext/u2/a538424.pdf>
4. A. Ronzhin, M. Albrow, S. Los, M. Martens, P. Murat, E. Ramberg, H. Kim, C. T. Chen, C. M. Kao, K. Niessen, A. Zatserklyaniy, M. Mazzillo, B. Carbone, G. Condorelli, G. Fallica, A. Piana, D. Sanfilippo, G. Valvo, and S. Ritt, "A sipm-based tof-pet detector with high speed digital drs4 readout," *Nuclear Instruments and Methods in Physics Research Section A: Accelerators, Spectrometers, Detectors and Associated Equipment*, vol. 703, p. 109, 2013. [Online]. Available: <http://www.sciencedirect.com/science/article/pii/S0168900212013800>
5. E. Takada, K. Sugiyama, H. Takahashi, T. Iguchi, and M. Nakazawa, "Neutron radiation distribution sensor using flexible plastic scintillating fiber combined with the time-of-flight technique," *IEEE Transactions on Nuclear Science*, vol. 42, no. 4, p. 570, August 1995.
6. G. F. Knoll, *Radiation Detection and Measurement*, 3rd ed. Hoboken, NJ: John Wiley & Sons, Inc., 2000.
7. J. B. Birks, "The Theory and Practice of Scintillation Counting," *Physics Today*, vol. 18, p. 60, 1965.
8. J. Chadwick, "The Existence of a Neutron," *The Royal Society of London Proceedings Series A*, p. 692, 1 June 1932. [Online]. Available: rspa.royalsocietypublishing.org
9. R. C. Ruchti, "Tracking with scintillating fibers," *Nuclear Physics B - Proceedings Supplements*, vol. 44, no. 1-3, p. 308, November 1995. [Online]. Available: <http://www.sciencedirect.com/science/article/pii/S0920563295800492>
10. Open Optogenetics, "Fiber Optics: Theory and Applications," 2010. [Online]. Available: www.openoptogenetics.org/images/8/89/Fiber_Optics_Theory_and_Applications.pdf

11. Saint-Gobain Crystals, “Scintillation products: Scintillating optical fibers,” 2011. [Online]. Available: <http://www.detectors.saint-gobain.com/uploadedFiles/SGdetectors/Documents/Brochures/Scintillating-Optical-Fibers-Brochure.pdf>
12. M. Weis, J. Lin, D. Taguchi, T. Manaka, and M. Iwamoto, “Analysis of transient currents in organic field effect transistor: The time-of-flight method,” *The Journal of Physical Chemistry C*, vol. 113, no. 43, 2009, online; Accessed 04-December-2013. [Online]. Available: <http://pubs.acs.org/doi/abs/10.1021/jp908381b>
13. N. Mirsaleh-Kohan, W. D. Nasrin, and R. N. Compton, “Electron ionization time-of-flight mass spectroscopy: Historical review and current applications,” *Mass Spectroscopy Reviews*, vol. 27, no. 3, 2008, online; Accessed 4-December-2013. [Online]. Available: <http://dx.doi.org/10.1002/mas.20162>
14. S. Cova, M. Ghioni, A. Lotito, I. Rech, and F. Zappa, “Evolution and prospects for single-photon avalanche diodes and quenching circuits,” *Journal of Modern Optics*, vol. 51, no. 9-10, 2004. [Online]. Available: <http://www.tandfonline.com/doi/abs/10.1080/09500340408235272>
15. Hamamatsu, “MppcTM: Mppc modules; compact opto-semiconductors with excellent photon-counting capability,” July 2013. [Online]. Available: http://www.hamamatsu.com/resources/pdf/ssd/mppc_kapd0002e.pdf
16. Tektronix, “Digital phosphor oscilloscopes: Dpo7000 series,” 2006. [Online]. Available: <http://www.tek.com/oscilloscope/dpo7000-digital-phosphor-oscilloscope>
17. O. Abdi, K. C. Wong, T. Hassan, K. J. Peters, and M. J. Kowalsky, “Cleaving of Solid Single Mode Polymer Optical Fiber for Strain Sensor Applications,” *Optics Communications*, 2009. [Online]. Available: <http://www.sciencedirect.com/science/article/pii/S0030401808011218>
18. The MathWorks, Inc., “Matlab[®] mat-file format: R2013b,” September 2013, online; Accessed 1-November-2013. [Online]. Available: http://www.mathworks.com/help/pdf_doc/matlab/matfile_format.pdf
19. L. Chiang and R. B. Oberer, “Computation of detection efficiencies for nmis fast plastic scintillators using a thick detector model,” October 2000, online; Accessed 24-May-2103. [Online]. Available: http://web.ornl.gov/~webworks/cpr/rpt/108927_.pdf
20. Hamamatsu, “Photomultiplier tubes and assemblies: For scintillation counting & high energy physics,” September 2012. [Online]. Available: http://www.hamamatsu.com/resources/pdf/etd/High_energy_PMT_TPMO0007E03.pdf
21. —, “Photomultiplier tubes: Photomultiplier tubes and related products,” August 2012. [Online]. Available: http://www.hamamatsu.com/resources/pdf/etd/PMT_TPMZ0001E01.pdf

REPORT DOCUMENTATION PAGE

Form Approved
OMB No. 0704-0188

The public reporting burden for this collection of information is estimated to average 1 hour per response, including the time for reviewing instructions, searching existing data sources, gathering and maintaining the data needed, and completing and reviewing the collection of information. Send comments regarding this burden estimate or any other aspect of this collection of information, including suggestions for reducing this burden to Department of Defense, Washington Headquarters Services, Directorate for Information Operations and Reports (0704-0188), 1215 Jefferson Davis Highway, Suite 1204, Arlington, VA 22202-4302. Respondents should be aware that notwithstanding any other provision of law, no person shall be subject to any penalty for failing to comply with a collection of information if it does not display a currently valid OMB control number. **PLEASE DO NOT RETURN YOUR FORM TO THE ABOVE ADDRESS.**

1. REPORT DATE (DD-MM-YYYY) 26-12-2013		2. REPORT TYPE Master's Thesis		3. DATES COVERED (From — To) October 2011 — December 2013	
4. TITLE AND SUBTITLE TIMING AND SPECTROSCOPY REQUIREMENTS FOR A PLASTIC SCINTILLATING FIBER BUNDLE TIME-OF-FLIGHT NEUTRON SPECTROMETER				5a. CONTRACT NUMBER In House	
				5b. GRANT NUMBER N/A	
				5c. PROGRAM ELEMENT NUMBER N/A	
				5d. PROJECT NUMBER N/A	
6. AUTHOR(S) Paul A. Clement, First Lieutenant, USAF				5e. TASK NUMBER N/A	
				5f. WORK UNIT NUMBER N/A	
				7. PERFORMING ORGANIZATION NAME(S) AND ADDRESS(ES) Air Force Institute of Technology Graduate School of Engineering and Management (AFIT/ENP) 2950 Hobson Way WPAFB OH 45433-7765	
8. PERFORMING ORGANIZATION REPORT NUMBER AFIT-ENP-13-D-01				9. SPONSORING / MONITORING AGENCY NAME(S) AND ADDRESS(ES) Mr. William Ulicny Department of Homeland Security - Domestic Nuclear Detection Office 245 Murray Dr. B410 Washington, DC 20528	
10. SPONSOR/MONITOR'S ACRONYM(S) DHS/DNDO				11. SPONSOR/MONITOR'S REPORT NUMBER(S) N/A	
12. DISTRIBUTION / AVAILABILITY STATEMENT DISTRIBUTION STATEMENT A: APPROVED FOR PUBLIC RELEASE; DISTRIBUTION UNLIMITED					
13. SUPPLEMENTARY NOTES This work is declared a work of the U.S. Government and is not subject to copyright protection in the United States.					
14. ABSTRACT The design parameters of a Time-of-Flight (TOF) neutron spectrometer composed of BCF-12 plastic scintillating fibers were investigated. A GEANT4 transport model was developed for analyzing the interaction of 2.5 MeV neutrons with a 14 × 14 BCF-12 fiber bundle. The bundle simulation demonstrated that 0.359% of all neutrons incident on the bundle will double scatter. The timing and data collection efficiencies of a Tektronix DPO7104 series digital oscilloscope were examined to determine the signal processing requirements for future fiber bundle measurements. The minimum detectable neutron energy was computed by taking into account the bundle scintillation efficiency, light collection efficiency, photodiode quantum efficiency, and quenching. For a BCF-12 fiber coupled to dual-readout Hamamatsu S10362-11-025C series Silicon Photomultipliers (SiPMT), the minimum detectable neutron energy was calculated to be 300–700 keV, depending on the fiber cladding and geometry. The spatial and timing uncertainties were set to 1 mm and 0.1 ns, respectively, to determine the overall energy uncertainty associated with a TOF neutron spectrometer. The uncertainties of 1 mm and 0.1 ns were chosen as the optimal capabilities of the the SiPMT and digital oscilloscope. Finally, analysis of a SiPMT in a light-tight box was performed to validate dark counts, determine light leakage and other detection system background noise. An experiment involving a 14 × 14 BCF-12 fiber bundle connected to dual-readout SiPMTs is recommended for future research to compare to the GEANT4 double scatter event probability.					
15. SUBJECT TERMS BCF-12, Fiber Bundle, Detection, Digital Data Acquisition, DPO7104, GEANT4, Neutron, Silicon Photomultiplier, Spectroscopy, Spectrometer, Scintillator, Tektronix, Time-of-Flight					
16. SECURITY CLASSIFICATION OF:			17. LIMITATION OF ABSTRACT UU	18. NUMBER OF PAGES 156	19a. NAME OF RESPONSIBLE PERSON Maj Benjamin R. Kowash, AFIT/ENP
a. REPORT U	b. ABSTRACT U	c. THIS PAGE U			19b. TELEPHONE NUMBER (include area code) 937-255-3636, x4571; benjamin.kowash@afit.edu